THE UNIVERSITY OF QUEENSLAND

AUSTRALIA

Graphene Oxide–Iron Oxide Nanocomposites for Dye Contaminated Wastewater Remediation

Nor Aida Zubir

Master of Engineering

A thesis submitted for the degree of Doctor of Philosophy at

The University of Queensland in 2015

School of Chemical Engineering

Abstract

The development of active and stable heterogeneous Fenton-like catalysts have emerged as an alternative to overcome the practical limitations related to the homogeneous Fenton catalyst, where various iron species and/or iron oxides are immobilised within the structure of different catalyst supports. Clay, alumina, zeolite and carbonaceous materials such as activated carbon and carbon nanotubes have been used as catalyst supports of choice by the scientific community. However, there is a knowledge gap associated with using high aspect ratio 2D (dimension) graphene oxide (GO) as an alternative catalyst support. Of particular interest, it is postulated that the structure and functionalities of GO as a support confers to the resultant catalyst overall catalytic activity beyond the conventional Fenton catalysts. In this thesis, the structural and physicochemical properties of resultant catalyst with their corresponding catalytic activity were systematically investigated. To this end, the synergistic interaction between GO and immobilised iron oxide nanoparticles (Fe_3O_4 NPs) was proposed for an oxidative degradation of synthetic dye acid orange 7 (AO7), which is a major water pollutant from textile production.

The GO–Fe_3O_4 nanocomposites were initially synthesised through a facile one-pot method by co-precipitating irons salts onto GO sheets in a basic solution. The formation of GO–Fe_3O_4 was postulated as follows: (i) Fe^{3+}/ Fe^{2+} ions are adsorbed and coordinated by the carboxyl groups (C=O) of GO sheets, (ii) hydrolysed ions form nanoclusters on GO sheets when NaOH is introduced, (iii) followed by condensation of the nanoclusters to form Fe_3O_4 nuclei, and (iv) further nucleation and growth of Fe_3O_4 crystallites on GO sheets were due to the redox reaction as the pH is increased to 10. The incorporation of GO led to an enhancement on the catalytic activity of the nanocomposites with 76% AO7 removal over the control catalysts of Fe_3O_4 NPs and GO sheets, which corresponds to 48 and 22%, respectively.

Further improvements on the catalytic activity of GO–Fe_3O_4 were performed by modifying the synthesis through pre-hydrolysing iron salts prior to GO addition at pH 4 with various GO loadings. The key finding of this new method is the formation of two sets of different mesoporous structure. At low GO loadings ≤10 wt%, GO–Fe_3O_4 nanocomposites resulted in high surface area up to 409 m^2 g^{-1}, in tandem with high 92–98% degradation of AO7. By contrast, GO loadings >10 wt% led to reduced surface area and lower GO–Fe_3O_4 activity (60%). The presence of strong interfacial interactions (Fe–O–C bonds) in the nanocomposites contributed to the superior degradation of AO7, in tandem with structural-morphological features.

The operational conditions of heterogeneous Fenton-like reaction were evaluated and modelled as a function of nanocomposites dosage, pH, temperature, oxidant and dye concentrations. Best results showed a fast 80% degradation in ~20 min, whilst ~98% of AO7 was successfully removed after 180 min of reaction time. Optimal conditions were determined for nanocomposites (GO(5wt%)–Fe_3O_4) at the catalyst dosage of 0.2 g L^{-1}, initial pH of 3 and 22 mM of H_2O_2 concentration at 298 K. The kinetics for the oxidative degradation of AO7 was found to be a pseudo-first-order reaction following the Langmuir-Hinshelwood mechanism.

A noteworthy finding was the high activity (>98%) and recyclability of GO–Fe_3O_4 over 7 cycles whilst the Fe_3O_4 NPs exhibited a severe loss of activity (~0%) at the 5th cycle. It was found that the ratio of Fe^{3+}/Fe^{2+} for GO–Fe_3O_4 remained almost constant over the 7 cycles, contrary to Fe_3O_4 NPs which underwent a significant Fe^{2+} decrease. The synergistic effect of GO in the GO–Fe_3O_4 nanocomposite was able to accelerate the $\equiv Fe^{3+}/\equiv Fe^{2+}$ redox cycles for the fast reduction of $\equiv Fe^{3+}$ to $\equiv Fe^{2+}$ which is actively participating in the decomposition of adsorbed H_2O_2 into $HO^{\bullet}$ radicals during catalysis. The X-ray photoelectron spectroscopy (XPS) analysis of spent GO–Fe_3O_4 showed that the sp^2 carbon domains (C=C) slightly decreased after every cycle, thus suggesting some degree of oxidation of the carbon basal plane. It is therefore postulated that the unusual stability in the GO–Fe_3O_4 is attributed to a donor-acceptor mechanism of the nanocomposites, in which the electrons donated from the oxidation of the GO are used for the regeneration of $\equiv Fe^{2+}$ and thus maintaining the Fe^{3+}/Fe^{2+} ratio.

Finally, the partial substitution of zinc (Zn) into Fe_3O_4 in the presence of GO was investigated, in view of the UV photocatalyst properties of zinc oxides. A slight change on the physicochemical properties of GO–$Fe_{3-x}Zn_xO_4$ lead to an increase in photocatalytic activity, where x=0.2 gave the higher degradation of AO7 in the UV-assisted Fenton-like reactions at 60 min reaction. It was found that the activity of the catalyst without GO always gave lower values ~30% of AO7 removal. Therefore, GO has proven again its beneficial use as an active component in the case of UV-assisted Fenton-like reaction as well.

Declaration by author

This thesis is composed of my original work, and contains no material previously published or written by another person except where due reference has been made in the text. I have clearly stated the contribution by others to jointly-authored works that I have included in my thesis.

I have clearly stated the contribution of others to my thesis as a whole, including statistical assistance, survey design, data analysis, significant technical procedures, professional editorial advice, and any other original research work used or reported in my thesis. The content of my thesis is the result of work I have carried out since the commencement of my research higher degree candidature and does not include a substantial part of work that has been submitted to qualify for the award of any other degree or diploma in any university or other tertiary institution. I have clearly stated which parts of my thesis, if any, have been submitted to qualify for another award.

I acknowledge that an electronic copy of my thesis must be lodged with the University Library and, subject to the policy and procedures of The University of Queensland, the thesis be made available for research and study in accordance with the Copyright Act 1968 unless a period of embargo has been approved by the Dean of the Graduate School.

I acknowledge that copyright of all material contained in my thesis resides with the copyright holder(s) of that material. Where appropriate I have obtained copyright permission from the copyright holder to reproduce material in this thesis.

Publications during candidature

Peer-reviewed papers

1. **N.A. Zubir**, X. Zhang, C. Yacou, J.C. Diniz da Costa, Fenton-like degradation of Acid Orange 7 using graphene oxide-iron oxide nanocomposite, Sci. Adv. Mater. 6 (2014) 1382-1388.

2. **N.A. Zubir**, C. Yacou, J. Motuzas, X. Zhang, J.C. Diniz da Costa, Structural and functional investigation of graphene oxide–Fe_3O_4 nanocomposites for the heterogeneous Fenton-like reaction, Sci. Rep. 4 (2014) 4594 1-8.

3. **N.A. Zubir**, C. Yacou, X. Zhang, J.C. Diniz da Costa, Optimisation of graphene oxide–iron oxide nanocomposite in heterogeneous Fenton-like oxidation of acid orange 7, J. Environ. Chem. Eng. 2 (2014) 1881-1888.

Conference abstract

1. **N.A. Zubir**, X. Zhang, C. Yacou, J.C. Diniz da Costa, Synthesis and characterization of water dispersible graphene oxide-Fe_3O_4 nanocomposites, 2012 UQ Engineering Postgraduate Research Conference, 4th June 2012, University of Queensland, Australia. (Oral presentation).

2. **N.A. Zubir**, X. Zhang, C. Yacou, J.C. Diniz da Costa, Fenton-like degradation of acid orange 7 using graphene oxide-iron oxide nanocomposite. 1st International Conference on Emerging Advanced Nanomaterials (ICEAN), 22-25th Oct 2012, Brisbane, Australia. (Oral presentation).

3. **N.A. Zubir**, X. Zhang, C. Yacou, J.C. Diniz da Costa, Graphene oxide (GO) membrane for gas separation. 3rd Early Career Researcher Membrane Symposium, 28-30th Nov 2012, University of Queensland, Australia. (Oral presentation).

4. **N.A. Zubir**, X. Zhang, C. Yacou, J.C. Diniz da Costa. Graphene oxide–iron oxide nanocomposites with enhanced heterogeneous Fenton-like activity for dye removal. XIth European Congress on Catalysis (EUROPACAT XI), 1-6th September 2013, Lyon, France. (Oral presentation).

Publications included in this thesis

N.A. Zubir, X. Zhang, C. Yacou, J.C. Diniz da Costa, Fenton-like degradation of Acid Orange 7 using graphene oxide-iron oxide nanocomposite, Sci. Adv. Mater. 6 (2014) 1382-1388. – incorporated as Chapter 3

Contributor	Statement of contribution
Author N.A. Zubir (Candidate)	Designed experiments (60%) Conducted experiment (80%) Analysed and interpreted data (60%) Wrote and edited the paper (60%)
Author X. Zhang	Designed experiments (30%) Conducted experiment (20%) Analysed and interpreted data (15%) Wrote and edited the paper (15%)
Author C. Yacou	Designed experiments (5%) Analysed and interpreted data (10%) Wrote and edited the paper (10%)
Author J.C. Diniz da Costa	Designed experiments (5%) Analysed and interpreted data (15%) Wrote and edited the paper (15%)

N.A. Zubir, C. Yacou, J. Motuzas, X. Zhang, J.C. Diniz da Costa, Structural and functional investigation of graphene oxide–Fe_3O_4 nanocomposites for the heterogeneous Fenton-like reaction, Sci. Rep. 4 (2014) 4594 1-8. – incorporated as Chapter 4

Contributor	Statement of contribution
Author N.A. Zubir (Candidate)	Designed experiments (80%) Conducted experiment (80%) Analysed and interpreted data (60%) Wrote and edited the paper (70%)
Author C. Yacou	Designed experiments (5%) Analysed and interpreted data (10%) Wrote and edited the paper (5%)

Author J. Motuzas	Designed experiments (5%) Conducted experiment (20%) Analysed and interpreted data (5%)
Author X. Zhang	Designed experiments (5%) Analysed and interpreted data (15%) Wrote and edited the paper (10%)
Author J.C. Diniz da Costa	Designed experiments (5%) Analysed and interpreted data (10%) Wrote and edited the paper (15%)

N.A. Zubir, C. Yacou, X. Zhang, J.C. Diniz da Costa, Optimisation of graphene oxide–iron oxide nanocomposite in heterogeneous Fenton-like oxidation of acid orange 7, J. Environ. Chem. Eng. 2 (2014) 1881-1888. – incorporated as Chapter 5

Contributor	Statement of contribution
Author N.A. Zubir (Candidate)	Designed experiments (85%) Conducted experiment (80%) Analysed and interpreted data (70%) Wrote and edited the paper (70%)
Author C. Yacou	Designed experiments (5%) Conducted experiment (20%) Analysed and interpreted data (10%) Wrote and edited the paper (5%)
Author X. Zhang	Designed experiments (5%) Analysed and interpreted data (10%) Wrote and edited the paper (10%)
Author J.C. Diniz da Costa	Designed experiments (5%) Analysed and interpreted data (10%) Wrote and edited the paper (15%)

Contributions by others to the thesis

Contributions by Prof Joe Diniz da Costa, A/Prof Dr Xiwang Zhang and Dr Christelle Yacou in the concept of research work, data analysis and interpretation as well as writing within the advisory capacity.

Statement of parts of the thesis submitted to qualify for the award of another degree

None

Acknowledgements

I would like to express my foremost gratefulness to Allah s.w.t. for His grace and guidance. I am greatly thankful to my research supervisors, Prof Joe Diniz da Costa, A/Prof Dr Xiwang Zhang and Dr Christelle Yacou, for their endless guidance, encouragement, motivations, patience and continuous supports throughout my PhD journey. I would like to thanks my committee members, Prof Duong Do and Prof George Zhao for their valuable reviews, constructive criticisms and suggestions.

I am also grateful to Dr Julius Motuzas, Dr Dana Lee Martens, Dr David Wang, Dr Simon Smart and my fellow colleagues in FIMLAB group; Adi Darmawan, Benjamin Ballinger, Muthia Elma, Yen Chua, Gianni Olguin Contreras, Diego Ruben Schmeda Lopez, Guozhi Ji, Liang Liu and Shengnan Wang for their insightful comments, tremendous supports and cherished friendships. Special acknowledgements go to the CMM and AIBN technical staffs, Dr Barry Wood, Anya Yago, Robyn Webb, Celestien Warnaar and Cheryl Berquist for their technical advises and supports.

I would like to acknowledge the Ministry of Higher Education Malaysia (MOHE) and Universiti Teknologi MARA (UiTM) for the financial support. My heartiest gratitude goes to my beloved mother and my late father for all the love and continuous encouragements. Last but not least, I dedicated this thesis to my beloved husband, Fikry Shukry and my lovely daughters, Iffah Raihana and Iffah Farhana. You are the pillar of my strength throughout this journey. I would not make it without your unconditional love, understandings and supports.

Keywords

Graphene oxide (GO), iron oxide (Fe_3O_4), nanoparticles (NPs), heterogeneous Fenton-like reaction, catalysis, dye degradation

Australian and New Zealand Standard Research Classifications (ANZSRC)

ANZSRC code: 090402, Catalytic Process Engineering, 50%

ANZSRC code: 090409, Wastewater Treatment Processes, 50%

Fields of Research (FoR) Classification

FoR code: 0904, Chemical Engineering, 100%

Table of Contents

List of Figures

List of Tables

List of Abbreviations

AC	Activated carbon
AFM	Atomic force microscopy
ANOVA	Analysis of variance
AOPs	Advanced oxidation processes
AO7	Acid orange 7
BET	Brunauer-Emmett-Teller
BPA	Bisphenol A
CNTs	Carbon nanotubes
Fe^{2+}	Ferrous ions
Fe^{3+}	Ferric ions
$\equiv Fe^{2+}$	Immobilised ferrous ions
$\equiv Fe^{3+}$	Immobilised ferric ions
Fe_3O_4	Iron oxide (magnetite)
Fe_2O_3	Iron oxide (hematite)
$Fe_{3-x}Zn_xO_4$	Zinc partially substituted magnetite
FCCD	Face centred central composite design
FESEM	Field-Emission Scanning Electron Microscopy
FTIR	Fourier-Transform Infrared Spectroscopy
GO	Graphene Oxide
GO–Fe_3O_4	Graphene oxide–iron oxide
GO–$Fe_{3-x}Zn_xO_4$	Graphene oxide–zinc partially substituted magnetite
$HO^{\bullet}$	Hydroxyl radicals
$HOO^{\bullet}$	Hydroperoxyl radicals
OH^-	Hydroxyl ions
H_2O_2	Hydrogen peroxide
HRTEM	High-Resolution Transmission Electron Microscopy

ICP-OES	Inductively Coupled Plasma-Optical Emission Spectroscopy
NPs	Nanoparticles
RhB	Rhodamine B
RSM	Response Surface Methodology
STEM-EDS	Scanning Transmission Electron Microscope-Energy Dispersive X-ray Spectrometer
TEM	Transmission Electron Microscopy
XAS	X-ray Absorption Spectroscopy
XPS	X-ray Photoelectron Spectroscopy
XRD	X-Ray Diffraction

Chapter 1

Introduction

1.1 Background

Dye contaminated wastewaters are a matter of global concern on water environment. In fact, the World Bank estimates that 17 to 20% of industrial water pollution emanates from textile dyeing and treatment processes [1]. As regulations become more stringent, the need for efficient treatment of these contaminants is imperative prior to discharge into natural water bodies. Advanced oxidation processes (AOPs) have been considered as a robust and efficient alternative for treating the dye contaminated wastewater when the common treatment processes, such as sedimentation, flocculation, adsorption and membrane filtration are insufficiently effective [2-5]. AOP processes are based on the generation of highly reactive hydroxyl radicals ($HO^{\bullet}$, oxidation potential E_0 up to +2.8V) to decompose persistent organic pollutants (i.e. dyes) [6]. The $HO^{\bullet}$ radicals are generated in situ via chemical oxidation using either ozone and/or hydrogen peroxide (H_2O_2) with or without radiation assisted sources such as thermal, ultrasonic, ultraviolet and visible lights.

Among these AOPs, oxidation using Fenton or Fenton-like reaction has been proven to be a promising approach due to the simplicity of the reaction operation coupled with an environmentally benign process. This is mainly attributed to the generation of $HO^{\bullet}$ radicals that enable oxidation of dyes efficiently and non-selectively [7, 8]. Nevertheless, the application of homogeneous Fenton or Fenton-like reactions usually suffer from several drawbacks. These include the need of post-treatment requirements prior to discharge as a result of iron hydroxide sludge formation which is considered as secondary pollutant, narrow pH operational range between 2.5–3.5, and unattainable regeneration of the catalyst which hampers the economic feasibility of this process [9-11].

Therefore, the development of heterogeneous Fenton-like catalysts emerged as a desirable alternative to overcome these practical limitations related to the respective homogeneous reactions whilst allowing for the heterogeneous catalysts to be reused in successive reaction cycles. In heterogeneous catalysts, the iron species are immobilised on or within the structure of the catalyst's support, such as clay [12-16], alumina [17, 18], zeolite [19, 20], silica [21] and carbonaceous materials [22-25]. Thus, the oxidation reactions mainly takes place at the solid-liquid interfaces, where the iron remains

substantially in solid phase either as a mineral or as an adsorbed ion [22]. The use of carbonaceous materials as a catalyst has been well proven due to its uniqueness in acting as a co-catalyst, such as activated carbon (AC) [24, 26, 27], mesoporous carbon [28], carbon aerogel [24, 29], and carbon nanotubes (CNTs) [22, 25, 30] that have been used as supports to immobilise the iron species for the preparation of heterogeneous Fenton-like catalysts.

Despite having high catalytic performance for the removal of dyes (≥90% removal) at the initial stage of reaction, these heterogeneous catalysts endured deactivation [24, 29] in the consecutive reaction cycles that are mainly ascribed to poisoning and/ or leaching due to dissolution of the iron species from the catalysts [2, 31]. The deactivation translates into the reduction of the catalytic activity over time. This is attributed to the instability of the supports which are intimately related to the dispersion of iron species, the nature and properties of the carbonaceous materials, as well as the specific interaction between active sites of the iron species and the supports itself [32]. Therefore, the selection of suitable catalyst supports is crucial for the development of active and stable heterogeneous Fenton-like catalysts.

Recently, Voitko et al. [33] reported that the derivative of graphene known as graphene oxide (GO) was able to exhibit greater reaction rate stability over an extended number of cycles (n>8) than any other carbonaceous material (AC, CNTs) for the decomposition of H_2O_2 in aqueous phase. This stability was linked to the GO morphology and surface functionalities, which consist of copious oxygenated functional groups present along the periphery and across the surface of the sheets [34-36]. In principle, using GO as a catalyst support is therefore attractive to address the shortcomings of current catalysts. Indeed there has been a limited number of reports in the literature for using GO as a substrate for the immobilisation of iron species as heterogeneous (Fenton-like) catalysts for the degradation of persistent organic pollutants [37-40]. However, none of these reports address the question on the structural stability of GO supported-iron containing nanocomposites for the heterogeneous Fenton-like reaction, which remains a gap in the literature. Instead, GO has been studied based on the conducting π-states from sp^2 carbon domain within the large energy gap (σ-states) of sp^3 domain with oxygenated functional groups [41-43] and the changes between these two domains may alter the inherent GO electronic properties [44, 45].

1.2 Scope and research contributions

Based on these gaps in the literature, this thesis focuses on the immobilisation of iron species onto GO sheets for the heterogeneous Fenton-like reaction. This study aims to address the inherent instability of conventional catalysts by investigating novel structures of GO supported-iron

containing nanocomposites as heterogeneous Fenton-like catalyst. There is a need to understand how the structural formation, or immobilisation of iron oxide nanoparticles (NPs) on GO can confer structures with the beneficial destruction of dyes. Within this theme, this thesis endeavours to address the synergies of structure and GO functionalities; knowledge required to understand the optimal conditions in which the heterogeneous Fenton-like reaction can take place. A major hypothesis in this thesis is that a stable catalyst is based on the synergetic structure and functionalities of the resultant GO supported-iron containing nanocomposites. In this case, this thesis also endeavours to answer the question related to the mechanism responsible for the attainment of catalytic stability under the heterogeneous Fenton-like reaction. A last question to be addressed is to whether GO catalysis may also enhance the UV-assisted catalytic activity of nanocomposites. Therefore, in order to address these PhD questions, this thesis investigates the synthesis of GO–iron oxide (GO–Fe_3O_4) nanocomposites at different GO loadings. The resultant nanocomposites are extensively characterised using nitrogen sorption, Fourier-transform infrared (FTIR), X-ray diffraction (XRD), high-resolution transmission electron microscopy (HRTEM), X-ray photoelectron spectroscopy (XPS), field-emission scanning electron microscopy (FESEM) and atomic force microscopy (AFM). In addition, a comprehensive study on the performance of the GO–Fe_3O_4 nanocomposites as catalysts are carried out under the heterogeneous Fenton-like reaction, and also the UV-assisted heterogeneous Fenton-like reaction.

The key contributions to knowledge of this thesis include:

- The synergistic interaction between GO and Fe_3O_4 NPs led to the formation of two distinct structures with different catalytic activities. The best structure was found to be associated with the beneficial intercalation of Fe_3O_4 NPs between the GO sheets, which subsequently favoured the high degradation of acid orange 7 (AO7; 92–98%) owing to the high surface area and pore volume, which enhanced the mass transfer of reactants towards the active sites ($\equiv Fe^{2+}$/ $\equiv Fe^{3+}$) during catalysis.
- The catalytic performance in the heterogeneous Fenton-like reaction is stable over all tested cycles based on the key finding that the Fe^{3+}/Fe^{2+} ratio of the GO–Fe_3O_4 was maintained during the reactions contrary to that of Fe_3O_4 NPs. This vital property of the donor-acceptor mechanism confers the spontaneous reduction of $\equiv Fe^{3+}$ to regenerate into $\equiv Fe^{2+}$ which is actively participating in the decomposition of H_2O_2 into HO• radicals. This postulation was further supported by another key finding related to electron transfer between GO and oxidised active sites ($\equiv Fe^{3+}$) via Fe–O–C bonds based on GO's slight oxidation.
- GO also contributed significantly to the UV-assisted Fenton-like reactions. GO loaded catalysts improved the oxidative degradation of AO7 by ~30% whilst the effect of containing

photo-luminescent zinc as GO–$Fe_{3-x}Zn_xO_4$ ($0 \leq x \leq 0.4$) provided minor catalytic activity improvement only.

1.3 Structure of thesis

This thesis is written in the European style which is now endorsed by the University of Queensland, whereby a collection of relevant publications is presented as part of the body in the thesis. A short description of the corresponding chapters is presented as follows:

Chapter 1: Introduction

This chapter introduces the background of the thesis and outlines the scopes and key contributions to the field of research.

Chapter 2: Literature Review

This chapter presents an overview and the recent progress in heterogeneous Fenton-like reaction and catalysts, particularly those containing or based on Fe_3O_4. Carbonaceous supports and GO as an alternative supports are also discussed, along with potential literature gaps.

Chapter 3: Graphene oxide–iron oxide (GO–Fe_3O_4) nanocomposites as an alternative heterogeneous Fenton-like catalyst

This chapter presents a postulated mechanism on the formation of GO–Fe_3O_4 nanocomposites and its characterisation. The catalytic performance of GO–Fe_3O_4 nanocomposites were evaluated by taking into account of their reactivity for the oxidation of AO7 as the model pollutant in the heterogeneous Fenton-like reaction. This chapter was published in Science of Advanced Materials.

Chapter 4: Structural and functional investigations of GO–Fe_3O_4 nanocomposites

This chapter presents the detailed investigation of the structural-morphology and functionality relationships of GO–Fe_3O_4 nanocomposites to correlate with their catalytic performances in heterogeneous Fenton-like reaction with respect to different amounts of GO loading. Two sets of different mesoporous structure were proposed based on the findings of the experimental works. This chapter was published in Scientific Reports.

Chapter 5: Optimisation of heterogeneous Fenton-like reaction using GO–Fe_3O_4 nanocomposites

This chapter presents the detailed investigation of the effect of different operational parameters of the oxidative degradation of AO7 using GO–Fe_3O_4 nanocomposites. This is then followed by performing kinetic studies and validation of reaction mechanism to explain the rate of intrinsic chemical reaction on the surface of active sites on the GO–Fe_3O_4 nanocomposites. This chapter was published in the Journal of Environmental Chemical Engineering.

Chapter 6: Recyclability and longevity of the catalyst based on the synergistic effect of GO and iron oxide in the heterogeneous Fenton-like reaction

This chapter presents the recyclability and longevity of the nanocomposites over seven consecutive cycles of oxidative degradation. The underlying interactions between the catalyst (Fe_3O_4 NPs) and its support (GO) were explored and explained based on the characterisation of both pristine and spent nanocomposites at their respective cycles of reaction.

Chapter 7: Physicochemical characterisation and catalytic properties investigation of graphene oxide with zinc partially substituted magnetite (GO–$Fe_{3-x}Zn_xO_4$) nanocomposites

This chapter presents the influence of GO when coupled with Fe_3O_4 and a photoluminescent catalyst (zinc oxide) in both heterogeneous and UV-assisted Fenton-like reactions. The Fe_3O_4, $Fe_{3-x}Zn_xO_4$ and GO–$Fe_{3-x}Zn_xO_4$ nanocomposites were characterised and tested for the oxidative degradation of AO7 at various zinc molar ratios (x), in order to understand the physicochemical and catalytic properties of the resultant materials, respectively.

Chapter 8: Conclusions and Recommendations

This chapter presents the major conclusions and recommendations for future work.

References

[1] S.H.S. Chan, T. Yeong Wu, J.C. Juan, C.Y. Teh, Recent developments of metal oxide semiconductors as photocatalysts in advanced oxidation processes (AOPs) for treatment of dye waste-water, J. Chem. Technol. Biot. 86 (2011) 1130-1158.

[2] A.N. Soon, B.H. Hameed, Heterogeneous catalytic treatment of synthetic dyes in aqueous media using Fenton and photo-assisted Fenton process, Desalination 269 (2011) 1-16.

[3] E. Forgacs, T. Cserháti, G. Oros, Removal of synthetic dyes from wastewaters: a review, Environ. Int. 30 (2004) 953-971.

[4] F.P. van der Zee, S. Villaverde, Combined anaerobic–aerobic treatment of azo dyes—a short review of bioreactor studies, Water Res. 39 (2005) 1425-1440.

[5] R. Fang, X. Cheng, X. Xu, Synthesis of lignin-base cationic flocculant and its application in removing anionic azo-dyes from simulated wastewater, Bioresource Technol. 101 (2010) 7323-7329.

[6] L. Gomathi Devi, S. Girish Kumar, K. Mohan Reddy, C. Munikrishnappa, Photo degradation of methyl orange an azo dye by advanced Fenton process using zero valent metallic iron: Influence of various reaction parameters and its degradation mechanism, J. Hazard. Mater. 164 (2009) 459-467.

[7] S.P. Sun, C.J. Li, J.H. Sun, S.H. Shi, M.H. Fan, Q. Zhou, Decolorization of an azo dye orange G in aqueous solution by Fenton oxidation process: Effect of system parameters and kinetic study, J. Hazard. Mater. 161 (2009) 1052-1057.

[8] J.H. Ramirez, F.M. Duarte, F.G. Martins, C.A. Costa, L.M. Madeira, Modelling of the synthetic dye orange II degradation using Fenton's reagent: From batch to continuous reactor operation, Chem. Eng. J. 148 (2009) 394-404.

[9] S.H. Tian, Y.T. Tu, D.S. Chen, X. Chen, Y. Xiong, Degradation of acid orange II at neutral pH using $Fe_2(MoO_4)_3$ as a heterogeneous Fenton-like catalyst, Chem. Eng. J. 169 (2011) 31-37.

[10] S. Karthikeyan, A. Titus, A. Gnanamani, A.B. Mandal, G. Sekaran, Treatment of textile wastewater by homogeneous and heterogeneous Fenton oxidation processes, Desalination 281 (2011) 438-445.

[11] G. Zhang, S. Wang, F. Yang, Efficient adsorption and combined heterogeneous/homogeneous Fenton oxidation of amaranth using supported nano-FeOOH as cathodic catalysts, J. Phys. Chem. C 116 (2012) 3623-3634.

[12] J. Herney-Ramirez, M. Lampinen, M.A. Vicente, C.A. Costa, L.M. Madeira, Experimental design to optimize the oxidation of orange II dye solution using a clay-based Fenton-like catalyst, Ind. Eng. Chem. Res. 47 (2008) 284-294.

[13] J.H. Ramirez, C.A. Costa, L.M. Madeira, G. Mata, M.A. Vicente, M.L. Rojas-Cervantes, A.J. López-Peinado, R.M. Martín-Aranda, Fenton-like oxidation of orange II solutions using heterogeneous catalysts based on saponite clay, Appl. Catal. B 71 (2007) 44-56.

[14] J. Herney-Ramirez, A.M.T. Silva, M.A. Vicente, C.A. Costa, L.M. Madeira, Degradation of acid orange 7 using a saponite-based catalyst in wet hydrogen peroxide oxidation: Kinetic study with the Fermi's equation, Appl. Catal. B 101 (2011) 197-205.

[15] H. Hassan, B.H. Hameed, Fe–clay as effective heterogeneous Fenton catalyst for the decolorization of reactive blue 4, Chem. Eng. J. 171 (2011) 912-918.

[16] E.G. Garrido-Ramírez, B.K.G. Theng, M.L. Mora, Clays and oxide minerals as catalysts and nanocatalysts in Fenton-like reactions — a review, Appl. Clay Sci. 47 (2010) 182-192.

[17] C.L. Hsueh, Y.H. Huang, C.Y. Chen, Novel activated alumina-supported iron oxide-composite as a heterogeneous catalyst for photooxidative degradation of reactive black 5, J. Hazard. Mater. 129 (2006) 228-233.

[18] H. Lim, J. Lee, S. Jin, J. Kim, J. Yoon, T. Hyeon, Highly active heterogeneous Fenton catalyst using iron oxide nanoparticles immobilized in alumina coated mesoporous silica, Chem. Commun. (2006) 463-465.

[19] M.L. Rache, A.R. García, H.R. Zea, A.M.T. Silva, L.M. Madeira, J.H. Ramírez, Azo-dye orange II degradation by the heterogeneous Fenton-like process using a zeolite Y-Fe catalyst—Kinetics with a model based on the Fermi's equation, Appl. Catal. B 146 (2014) 192-200.

[20] M. Aleksić, H. Kušić, N. Koprivanac, D. Leszczynska, A.L. Božić, Heterogeneous Fenton type processes for the degradation of organic dye pollutant in water — the application of zeolite assisted AOPs, Desalination 257 (2010) 22-29.

[21] P.P. Gan, S.F.Y. Li, Efficient removal of rhodamine B using a rice hull-based silica supported iron catalyst by Fenton-like process, Chem. Eng. J. 229 (2013) 351-363.

[22] X. Hu, B. Liu, Y. Deng, H. Chen, S. Luo, C. Sun, P. Yang, S. Yang, Adsorption and heterogeneous Fenton degradation of 17α-methyltestosterone on nano Fe_3O_4/MWCNTs in aqueous solution, Appl. Catal. B 107 (2011) 274-283.

[23] L. Zhou, H. Zhang, L. Ji, Y. Shao, Y. li, Fe_3O_4/MWCNT as heterogeneous Fenton catalyst: Degradation pathways of tetrabromobisphenol A, RSC Adv. 4 (2014) 24900-24908.

[24] J.H. Ramirez, F.J. Maldonado-Hódar, A.F. Pérez-Cadenas, C. Moreno-Castilla, C.A. Costa, L.M. Madeira, Azo-dye orange II degradation by heterogeneous Fenton-like reaction using carbon-Fe catalysts, Appl. Catal. B 75 (2007) 312-323.

[25] S. Song, R. Rao, H. Yang, H. Liu, A. Zhang, Facile synthesis of Fe_3O_4/MWCNTs by spontaneous redox and their catalytic performance, Nanotechnol. 21 (2010) 185602-185607.

[26] N. Thi Dung, P. Ngoc Hoa, D. Manh Huy, N. Kim Tham, Magnetic Fe_2MO_4 (M:Fe, Mn) activated carbons: Fabrication, characterization and heterogeneous Fenton oxidation of methyl orange, J. Hazard. Mater. 185 (2011) 653-661.

[27] A. Rodriguez, G. Ovejero, J.L. Sotelo, M. Mestanza, J. Garcia, Heterogeneous Fenton catalyst supports screening for mono azo dye degradation in contaminated wastewaters, Ind. Eng. Chem. Res. 49 (2010) 498-505.

[28] F. Duan, Y. Yang, Y. Li, H. Cao, Y. Wang, Y. Zhang, Heterogeneous Fenton-like degradation of 4-chlorophenol using iron/ordered mesoporous carbon catalyst, J. Environ. Sci. 26 (2014) 1171-1179.

[29] F. Duarte, F.J. Maldonado-Hódar, A.F. Pérez-Cadenas, L.M. Madeira, Fenton-like degradation of azo-dye orange II catalyzed by transition metals on carbon aerogels, Appl. Catal. B 85 (2009) 139-147.

[30] J. Deng, X. Wen, Q. Wang, Solvothermal in situ synthesis of Fe_3O_4-multi-walled carbon nanotubes with enhanced heterogeneous Fenton-like activity, Mater. Res. Bull. 47 (2012) 3369-3376.

[31] K. Pirkanniemi, M. Sillanpää, Heterogeneous water phase catalysis as an environmental application: a review, Chemosphere 48 (2002) 1047-1060.

[32] S. Navalon, A. Dhakshinamoorthy, M. Alvaro, H. Garcia, Heterogeneous Fenton catalysts based on activated carbon and related materials, ChemSusChem 4 (2011) 1712-1730.

[33] K.V. Voitko, R.L.D. Whitby, V.M. Gun'ko, O.M. Bakalinska, M.T. Kartel, K. Laszlo, A.B. Cundy, S.V. Mikhalovsky, Morphological and chemical features of nano and macroscale carbons affecting hydrogen peroxide decomposition in aqueous media, J. Colloid Interf. Sci. 361 (2011) 129-136.

[34] D.R. Dreyer, S. Park, C.W. Bielawski, R.S. Ruoff, The chemistry of graphene oxide, Chem. Soc. Rev. 39 (2010) 228-240.

[35] C. Su, K.P. Loh, Carbocatalysts: Graphene oxide and its derivatives, Accounts Chem. Res. 46 (2013) 2275-2285.

[36] A. Lerf, H. He, M. Forster, J. Klinowski, Structure of graphite oxide revisited[I], J. Phys. Chem. B 102 (1998) 4477-4482.

[37] G. He, W. Liu, X. Sun, Q. Chen, X. Wang, H. Chen, Fe_3O_4@graphene oxide composite: A magnetically separable and efficient catalyst for the reduction of nitroarenes, Mater. Res. Bull. 48 (2013) 1885-1890.

[38] S. Guo, G. Zhang, Y. Guo, J.C. Yu, Graphene oxide–Fe_2O_3 hybrid material as highly efficient heterogeneous catalyst for degradation of organic contaminants, Carbon 60 (2013) 437-444.

[39] Z.L. Hua, W.Q. Ma, X. Bai, R.R. Feng, L. Yu, X.Y. Zhang, Z.Y. Dai, Heterogeneous Fenton degradation of bisphenol A catalyzed by efficient adsorptive Fe_3O_4/GO nanocomposites, Environ. Sci. Pollut. Res. 21 (2014) 7737-7745.

[40] Y. Dong, J. Li, L. Shi, J. Xu, X. Wang, Z. Guo, W. Liu, Graphene oxide-iron complex: Synthesis, characterization and visible-light-driven photocatalysis, J. Mater. Chem. A 1 (2013) 644-650.

[41] Y. Matsumoto, M. Koinuma, S. Ida, S. Hayami, T. Taniguchi, K. Hatakeyama, H. Tateishi, Y. Watanabe, S. Amano, Photoreaction of graphene oxide nanosheets in water, J. Phys. Chem. C 115 (2011) 19280-19286.

[42] K.P. Loh, Q. Bao, G. Eda, M. Chhowalla, Graphene oxide as a chemically tunable platform for optical applications, Nat. Chem. 2 (2010) 1015-1024.

[43] L.M. Pastrana-Martínez, S. Morales-Torres, V. Likodimos, J.L. Figueiredo, J.L. Faria, P. Falaras, A.M.T. Silva, Advanced nanostructured photocatalysts based on reduced graphene oxide–TiO_2 composites for degradation of diphenhydramine pharmaceutical and methyl orange dye, Appl. Catal. B 123–124 (2012) 241-256.

[44] A. Bagri, C. Mattevi, M. Acik, Y.J. Chabal, M. Chhowalla, V.B. Shenoy, Structural evolution during the reduction of chemically derived graphene oxide, Nat. Chem. 2 (2010) 581-587.

[45] G. Liao, S. Chen, X. Quan, H. Yu, H. Zhao, Graphene oxide modified g-C_3N_4 hybrid with enhanced photocatalytic capability under visible light irradiation, J. Mater. Chem. 22 (2012) 2721-2726.

Chapter 2

Literature Review

Abstract

This review examines the existing literature on the heterogeneous Fenton-like reaction, focusing on catalyst type, preparation methods and performance. It starts by describing the motivation of processing wastewater containing dyes which require degradation. The homogenous Fenton-like reaction is then briefly addressed followed by a more comprehensive review of the heterogeneous Fenton-like reaction in Section 2.3. It is observed at this point that there is a gap in the literature, related to the need of catalysts with novel structures to be stable over several cycles. Out of several potential candidates, graphene oxide (GO) warrants investigation as a novel catalyst support, and is covered in Section 2.4. Coupling GO with iron oxides or other types of metal oxides for the degradation of pollutants in water is also reviewed, though it is observed that there is still a gap to be investigated related to GO plus metal oxides. Finally, a summary of the major findings and gaps in the literature are discussed in Section 2.5.

2.1 Dye contaminated wastewater

Wastewater originating from textile dyeing processes consist of a wide variety of organic dyes, which have a great influence on both environment and human health impacts due to their toxicity, biodegradability and aesthetic aspects [1, 2]. It has been estimated that more than $7x10^5$ tons of around 10,000 different commercial dyes and pigments are produced annually globally [3, 4]. In fact, the World Bank estimates that 17 to 20% of industrial water pollution originates from textile dyeing and treatment processes [5]. The dye molecules share some similarities in both chemical structure and physical characteristics that mainly comprise of two key components, namely chromophores and auxochromes [6, 7]. The chromophore refers to the part of the dye molecule which consists of conjugated aromatic π bonds which are responsible for producing colours. Meanwhile, auxochrome refers to the electron-withdrawing or electron-donating substituents attached to a chromophore that not only supplement the chromophore by altering the overall energy of the electron system, but also render the molecule soluble in water and enhances their affinity toward textile fibres.

Approximately 60–70% of the global production of dyes are classified as azo dyes which consist of one or more azo groups (R_1–N=N–R_2) in the chromophoric component that is mostly substituted by sulfonate (–SO_3) and hydroxyl groups (–OH) [8, 9]. Among these azo dyes, well known acid orange 7 (AO7) or orange II (Figure 2.1a) represents more than half of the global azo dye production in the textile manufacturing industry because of its low cost and high stability [10]. AO7 is an anionic monoazo textile dye of the acid class which is resistant to light degradation, ozone and common acids or bases. AO7 consists of four absorbance bands as illustrated in Figure 2.1b [11]. The two main absorption bands in the visible region, one centred at 484 nm and the other a shoulder at 430 nm, correspond to the hydrazone and azo forms of the chromophore, respectively. The other two bands at 230 nm and 310 nm in the ultraviolet region are assigned to the adjacent auxochromes of benzene and naphthalene, as shown in Figure 2.1a. Changes in absorbance peaks reflect the evolution of AO7's chromophore, allowing useful information to be obtained and monitored by UV-vis analysis [11, 12].

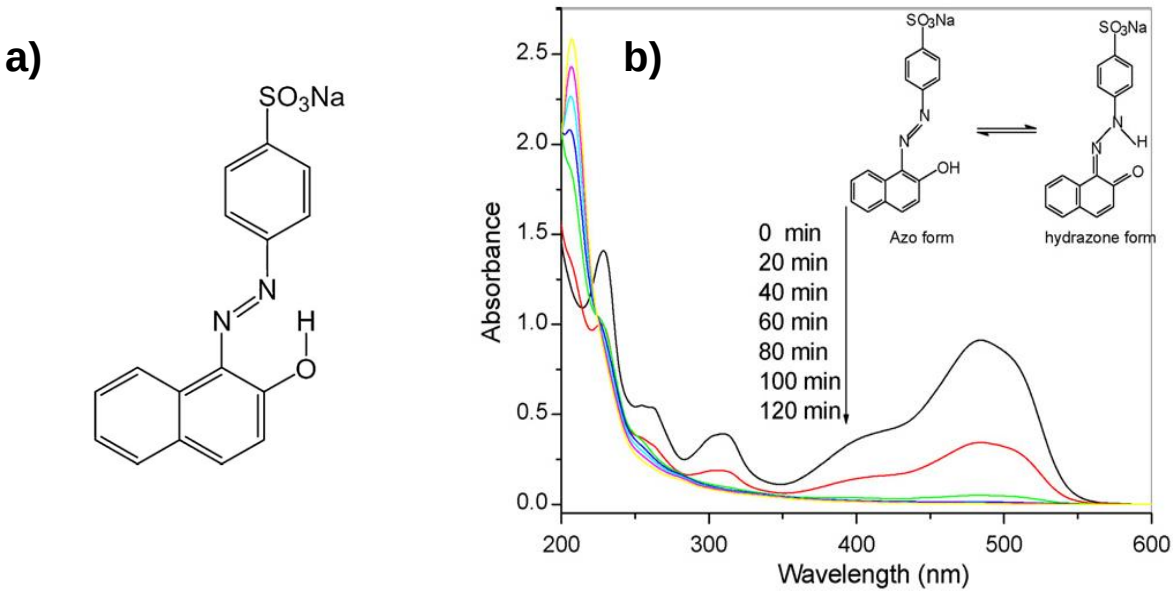

Figure 2.1: a) Molecular structure of AO7 and b) UV–vis spectral changes of AO7 in solution under electrochemically assisted photocatalytic degradation as a function of irradiation time [11].

2.2 Homogeneous Fenton reaction

As regulations become more stringent, the treatment and discharge of dye contaminated wastewater is highly regulated and compulsory. Various treatments such as physicochemical and biological processes have been widely investigated [13-15]. Each of these treatments has its own advantages

and disadvantages in the remediation of dye contaminated wastewater. Of the numerous treatments available, considerable attention has been paid to advanced oxidation processes (AOPs) due to their attractive features, such as the production of highly potent and strongly oxidizing radicals which allow for the destruction of a wide range of persistent organic compounds [2, 16, 17].

One of the most intensively studied AOPs is the process based on the Fenton reactions because of its own unique advantages. These include simple operation, high degradation efficiency, and because they employ environmentally benign chemicals that generate the highly reactive hydroxyl ($HO^{\bullet}$) radicals which are able to oxidise dyes efficiently and non-selectively [8, 18, 19]. The active sites in the Fenton process are derived from iron ions which serve as catalysts to decompose H_2O_2 molecules into $HO^{\bullet}$ radicals. The sequential steps that take place in the process of the classical homogeneous Fenton reaction is shown in Equations 2.1–2.6 [20, 21].

$$Fe^{2+} + H_2O_2 \rightarrow Fe^{3+} + HO^{\bullet} + OH^{-} \qquad k_1 = 76\ \mathrm{M^{-1}s^{-1}} \qquad (2.1)$$

$$Fe^{3+} + H_2O_2 \rightarrow Fe^{2+} + HOO^{\bullet} + H^{+} \qquad k_2 = 0.001 - 0.01\ \mathrm{M^{-1}s^{-1}} \qquad (2.2)$$

$$Fe^{2+} + HOO^{\bullet} \rightarrow Fe^{3+} + HOO^{-} \qquad k_3 = 1.3\times10^{6}\ \mathrm{M^{-1}s^{-1}} \qquad (2.3)$$

$$Fe^{3+} + HOO^{\bullet} \rightarrow Fe^{2+} + O_2 + H^{+} \qquad k_4 = 1.3\times10^{6}\ \mathrm{M^{-1}s^{-1}} \qquad (2.4)$$

$$H_2O_2 + HO^{\bullet} \rightarrow HOO^{\bullet} + H_2O \qquad k_5 = 2.7\times10^{7}\ \mathrm{M^{-1}s^{-1}} \qquad (2.5)$$

$$HO^{\bullet} + \text{organic compounds} \rightarrow \text{intermediates} \rightarrow CO_2 + xH_2O \qquad (2.6)$$

The reduction of iron (production of hydroperoxyl radicals ($HOO^{\bullet}$), Equation 2.2) proceeds considerably more slowly than the oxidation of iron (production of $HO^{\bullet}$ radicals, Equation 2.1). Therefore, the rate limiting step in the overall oxidation rate is mainly governed by the slow regeneration of ferrous ions (Fe^{2+}), which makes the homogeneous Fenton reaction unfeasible for practical applications as the overall reaction slows down after the conversion of Fe^{2+} to ferric ions (Fe^{3+}). Moreover, the homogeneous Fenton and/or Fenton-like reactions possess severe limitations, including: the necessity for post-treatment prior to discharge due to the formation of iron hydroxide sludge; narrow operational pH range (2.5–3.5); and unattainable regeneration of catalyst that seems to be uneconomical [19, 22].

These limitations can be circumvented through the utilisation of heterogeneous solid catalysts which can mediate the heterogeneous Fenton-like reaction by: (i) providing a second matrix phase to prevent the Fe^{3+} ions from combining with the hydroxyl ions (OH^-) to form iron hydroxide sludge [23] and (ii) to provide a sink to absorb an electron from a hydroxyl ion to generate $HO^{\bullet}$ radicals [19, 23]; whilst having fast regeneration of Fe^{2+} ions to catalytically decompose H_2O_2 into $HO^{\bullet}$ radicals during catalysis.

2.3 Heterogeneous Fenton-like reaction

In the heterogeneous Fenton-like catalysts, various types of iron compounds are immobilised within the structure and in the pore/interlayer spaces of different types of catalyst supports, such as silica [24], clay [20, 25-27], alumina [28, 29], zeolites [2, 30] and carbonaceous materials [31, 32]. These include complexes of iron with organic ligands or solid iron oxides as summarised in Table 2.1. The decomposition of H_2O_2 in the heterogeneous Fenton-like reaction follows Equations 2.7–2.8, where ≡ represents the iron species bound to the surface of the catalyst support. In principle, most of the reactions occur at the solid–liquid interfaces, either at the surface of the support or in the pores of the support, where the iron species remains substantially in the solid phase, either as a mineral or as an adsorbed ion [33].

$$\equiv Fe^{2+} + H_2O_2 \rightarrow \equiv Fe^{3+} + HO^{\bullet} + OH^- \quad (2.7)$$

$$\equiv Fe^{3+} + H_2O_2 \rightarrow \equiv Fe^{2+} + HOO^{\bullet} + H^+ \quad (2.8)$$

Table 2.1: Supported iron-containing nanocomposites on the oxidative degradation of dyes in the heterogeneous and/ or UV assisted Fenton-like reactions.

Dyes	Catalyst	Catalyst support	Percentage of removal	Conditions	Refs.
Rhodamine B	Fe-ligands	Silica	99% in 120 min	pH 5; 1 g L^{-1} catalyst; 5 mg L^{-1} dye; 19.6 mM H_2O_2; 30 °C	[24]
Rhodamine B	Iron complexes	Silica	99% in 30 min	pH 3; 5 g L^{-1} catalyst; 25 mg L^{-1} dye; H_2O_2; 30 °C; 50 W UVA	[34]
Acid orange II	Iron complexes	Clay	99% in 120 min	pH 3; 0.7 g L^{-1} catalyst; 70 mg L^{-1} dye; 13 mM H_2O_2; 40 °C	[27]
Reactive Blue 4	Fe_2O_3	Clay	99% in 140 min	pH 3; 5 g L^{-1} catalyst; 50 mg L^{-1} dye; 4 mM H_2O_2; 30 °C	[26]
Acid orange II	Fe_2O_3 and $Fe_2Si_4O_{10}$	Laponite clay	99% in 120 min	pH 3; 1 g L^{-1} catalyst; 70 mg L^{-1} dye; 9.6 mM H_2O_2; 25 °C; 8 W UVC	[35]
Acid orange II	Fe-ligands	Bentonite clay	30% in 120 min/ 98% in 20 min (UV)	pH 3; 1 g L^{-1} catalyst; 70 mg L^{-1} dye; 10 mM H_2O_2; 30 °C; 6 W UVA	[36]
Reactive Blue 137	Iron complexes	Zeolites	95% in 60 min	pH 3; 1.5 g L^{-1} catalyst; 20 mg L^{-1} dye; 10 mM H_2O_2; 30 °C	[2]
Acid orange II	Iron complexes	Zeolites	99% in 90 min	pH 3; 0.2 g L^{-1} catalyst; 35 mg L^{-1} dye; 6 mM H_2O_2; 30 °C	[30]
Rhodamine 6G	Iron complexes	Zeolites	99% in 90 min	pH 3.4; 1 g L^{-1} catalyst; 100 mg L^{-1} dye; 267 mM H_2O_2; 50 °C	[37]
Reactive black 5	Fe_2O_3	Alumina	90% in 60 min	pH 3.5; 2 g L^{-1} catalyst; 99 mg L^{-1} dye; 5.9 mM H_2O_2; 15 W UVA	[28]
Reactive black 5	Fe_2O_3	Alumina	99% in 600 min	pH 4.1; 0.2 g L^{-1} catalyst; 100 mg L^{-1} dye; 5 mM H_2O_2; 25 °C	[29]
Acid orange II	Iron complexes	Carbon	99% in 240 min	pH 3; 0.1 g L^{-1} catalyst; 35 mg L^{-1} dye; 6 mM H_2O_2; 30 °C	[31]
Reactive Red	Iron complexes	Carbon	99% in 30 min	pH 2.95; 5 g L^{-1} catalyst; 56.8 mg L^{-1} dye; 30 mM H_2O_2; 50 °C	[32]

Several recent studies have investigated different iron oxides and/ or iron hydroxides as heterogeneous catalysts for the Fenton-like reactions, such as α-Fe_2O_3 [38-40], γ-Fe_2O_3 [41, 42], Fe_3O_4 [33, 43-49] and FeOOH [50-52]. Among these iron oxides and/ or iron hydroxides, the inverse spinel Fe_3O_4 has been found to work efficiently as a heterogeneous catalyst in the heterogeneous Fenton-like reaction, based on its high Fenton activity [46, 53, 54]. This is due to the fact that the Fe_3O_4 possesses several unique features [46, 55-58] such as: (i) it contains both Fe^{2+} and Fe^{3+} in the spinel structure, where the Fe^{2+} occupies only the octahedral site whilst Fe^{3+} are distributed equally between both octahedral and tetrahedral sites, as illustrated in Figure 2.2; (ii) the presence of Fe^{2+} occupying the octahedral sites in the spinel structure plays a significant role in initiating the decomposition of H_2O_2 into $HO^{\bullet}$ radicals according to the classical Haber–Weiss mechanism (Equation 2.1) that can be represented by Equation 2.7; (iii) the accommodation of both Fe^{2+} and Fe^{3+} on the octahedral sites allowing the iron species to be reversibly oxidised and reduced without structural change; and (iv) the iron ions in the spinel structure of Fe_3O_4 can be isomorphically substituted with several transition metals which have various redox properties altering the catalytic properties of the resulting materials. In addition, the Fe_3O_4 can be easily separated from the reaction medium using an external magnetic field due to its inherent magnetic properties [59-61].

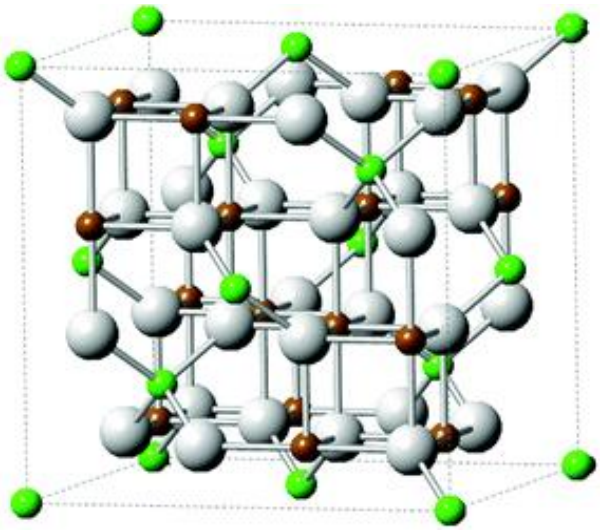

Figure 2.2: The spinel structure of Fe_3O_4. The green atoms are indicative to Fe^{2+}, brown atoms are Fe^{3+} and white atoms are oxygen [61].

However, the Fe_3O_4 particles and/ or nanoparticles (NPs) are prone to aggregation, forming agglomerates, specifically due to strong anisotropic dipolar interactions in the aqueous phase. This reduces their dispersibility and catalytic properties, which eventually diminishes their overall activity [62]. In this regard, there is a need to immobilise these particles and/or NPs onto various supports for the preservation of their unique properties. Immobilisation of Fe_3O_4 particles and/or NPs within the structure of solid supports has emerged as another type of promising heterogeneous Fenton-like catalyst in the past few years. In particular, the use of carbonaceous materials as the catalyst support has been well proven because of its unique capability of acting as a co-catalyst [63, 64]. Various types of carbonaceous materials such as activated carbons (AC) [65, 66], carbon aerogels [65, 67], carbon microfibers [68], carbon spheres [69], mesoporous carbon [70], and carbon nanotubes (CNTs) [71, 72] have been used as supports to immobilise the Fe_3O_4 particles and/or (NPs) for the preparation of heterogeneous Fenton-like catalysts as summarised in Table 2.2.

Most authors have considered the synergistic effect resulting from the adsorption properties of the support, which enables the pre-concentration of pollutants to be oxidised within the vicinity of the active sites which substantially enhances the catalytic activity of the carbon-based supported Fe_3O_4 nanocomposites. However, these nanocomposites also suffer from some degree of deactivation in the successive cycles of reaction [65, 67], despite having high catalytic performance with more than 90% removal rate of dyes obtained during the initial stage of reaction. This deactivation is mainly attributed to the poisoning and/ or dissolution of the iron species from the supported catalyst into the acidic medium (leaching) during catalysis [16, 65, 67, 73]. This manifests as a decrease of catalytic activity for carbon-based supported Fe_3O_4 nanocomposites over time due to the:
(i) instability of the supports, which is intimately related to the dispersion of immobilised Fe_3O_4; (ii) the nature and properties of the carbonaceous materials; as well as (iii) the specific interaction between active sites of the Fe_3O_4 and the supports [74]. Hence, the need for more stable catalyst supports is vital for the development of active and stable heterogeneous Fenton-like catalysts.

Table 2.2: Carbon-based supported Fe_3O_4 nanocomposites on the oxidative degradation of dyes in the heterogeneous and/ or UV assisted Fenton-like reactions.

Dyes	Carbonaceous materials	Colour removal	Conditions	Refs.
Acid orange II	AC/ Carbon aerogel	98% in 200 min/ 99% in 120 min	pH 3; 0.2 g L^{-1} catalyst; 35 mg L^{-1} dye; 6 mM H_2O_2; 30 °C	[65]
Methyl orange	AC	55% in 90 min	pH 4.0; 2.5 g L^{-1} catalyst; 50 mg L^{-1} dye; 18 mM H_2O_2; 30 °C	[66]
Acid orange II	Carbon aerogel	98% in 300 min/	pH 3; 0.2 g L^{-1} catalyst; 35 mg L^{-1} dye; 6 mM H_2O_2; 30 °C	[67]
Congo red	Carbon microfibers	99% in 120 min	pH 3.5; 1.0 g L^{-1} catalyst; 100 mg L^{-1} dye; 50 mM H_2O_2; 30 °C, 15 W UVC	[68]
Methylene blue	Carbon spheres	60% in 720 min	1 g L^{-1} catalyst; 10 mg L^{-1} dye; 15 W UVA	[69]
1-diazo-2-naphthol-4-sulfonic acid dye	Mesoporous carbon	94% in 120 min	pH 5; 0.5 g L^{-1} catalyst; 250 mg L^{-1} dye; 15 mM H_2O_2; 30 °C	[70]
Methylene blue	CNTs	97% in 720 min	pH 5.5; 0.3 g L^{-1} catalyst; 10 mg L^{-1} dye; 400 mM H_2O_2; 25 °C	[71]
Acid orange II	CNTs	94% in 30 min	pH 3.5; 0.5 g L^{-1} catalyst ; 87.5 mg L^{-1} dye; 15 mM H_2O_2	[72]
Rhodamine B	CNTs	80% in 120 min	pH 2; 2.5 g L^{-1} catalyst ; 10 mg L^{-1} dye; 245 mM H_2O_2, 4W UVA	[75]

2.4 Graphene oxide (GO) based nanocomposites/ nanocatalysts

A potential carbonaceous support that has been studied in a limited number of cases is GO. Voitko et al. [76] have recently reported that the derivative of graphene known as graphene oxide (GO) has demonstrated greater stability in preserving its catalytic activity over an extended number of cycles (n>8) than any other carbonaceous material, including AC and CNTs for the decomposition of H_2O_2 in aqueous solution. Such stability was inextricably linked to the GO morphology and surface functionalities, which consists of copious oxygenated functional groups present along the periphery and across the surface of the sheets [76-79] as presented in Figure 2.3.

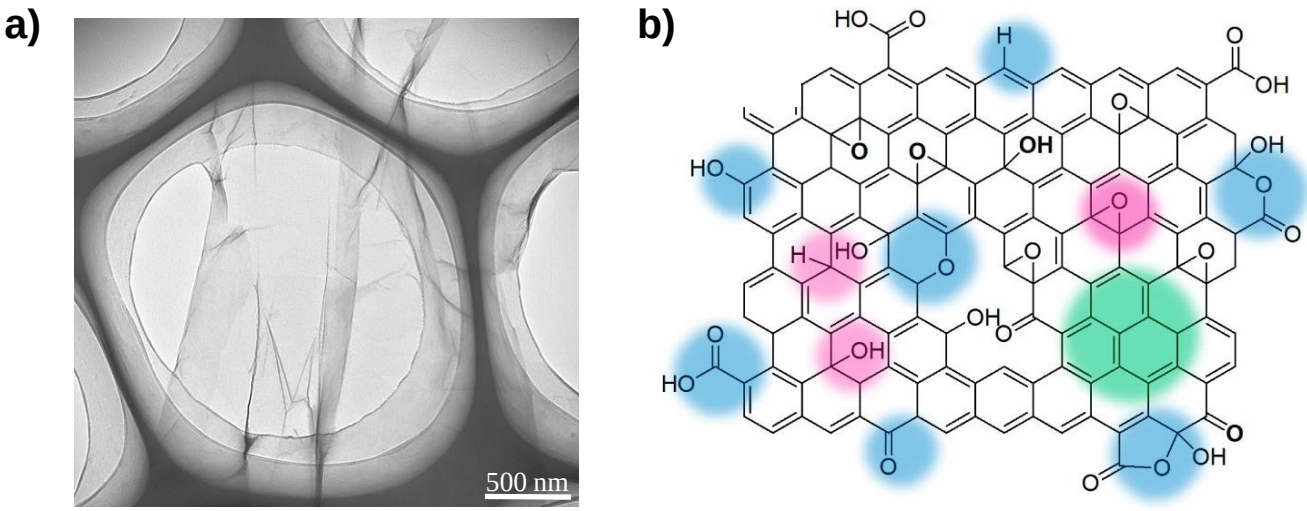

Figure 2.3: a) TEM image of GO b) Proposed structure of GO based on the Lerf–Klinowski model. Hydroxyls and epoxide groups (pink) are the dominant functionalities on the basal plane. The edge defects are unique sites for some oxygen functionalities (blue) [79].

There are two distinct regions [77-80] in the two-dimensional structure of GO as proposed by the Lerf–Klinowski model (Figure 2.3b). The first region is predominately associated with the sp^2 hybridised carbon domains (graphene-like) whilst the second region is ascribed to the highly oxygenated functional groups, such as the hydroxyl and epoxide groups which are present on the basal plane while the carbonyl and carboxyl groups are on the edges. The presence of these functional groups allows GO sheets to be easily exfoliated in water or a polar solvent to yield stable dispersions. In addition, GO acts as a weak acid cation-exchange resin because of the ionisable carboxyl groups, which allow ion exchange with metal cations or positively charged organic molecules [81]. These properties serve GO as a promising two-dimensional support to nucleate and anchor metal and/ or metal oxide NPs on both edges and surfaces [82]. Besides its rich surface chemistry, GO also possesses a heterogeneous electronic structure due to the presence of conducting π-states originating from sp^2 carbon domains and the large energy gap between the σ-states of the sp^3 domains connected to the oxygenated functional groups [83-85]. Thus, the changes in carbon to oxygen (C/O) ratio may modify the GO electronic properties from insulating to semiconducting [86, 87]. These unique characteristics make GO a potential candidate as an alternative to carbocatalysts as well as supports of immobilised active catalysts.

2.4.1 GO as carbocatalysts

Owing to the inherent rich, chemical functionality and reactivity, strong acidity, and the high surface area upon reduction, GO has been actively exploited as a carbocatalyst for various synthetic reactions in the past few years. For instance, GO mediates the oxidation of various hydrocarbons [88], sulphides [89] and olefins [90], aza-Michael additions [91], the hydration of alkynes [88], dehydration–hydrothiolation of secondary aryl alcohols [92], reduction of nitrobenzene into aniline [93], Friedel–Crafts addition of α,β-unsaturated ketones to indoles [94], and Strecker reaction of ketones to synthesise α-amino nitriles [95]. In fact, GO was able to show its stability without having any detrimental loss in its catalytic activity in consecutive cycles of reaction. Table 2.3 summarises the significant roles of GO in enhancing the overall catalytic performance of reactions.

Table 2.3: GO as carbocatalysts

Application	Key performances	Roles of GO	Refs.
Oxidation of benzyl alcohol to benzaldehyde	Benzaldehyde conversion > 98% with 200 wt % GO at 100 °C in 24 h	Enhanced reactivity was due to the presence of oxygenated functional groups that facilitates the oxidation process	[88]
Aza-Michael addition reaction	Enhance yield of β-amino compounds; GO: 97% (5 min) Reduced-GO: 95% (30 min) Without GO: 96% (35 min)	The presence of oxygenated functional groups activating the aza-Michael addition reaction	[91]
Dehydration–hydrothiolation of secondary aryl alcohols	Enhance yield of thioether; GO: 74% (120 min) Graphite:77% (420 min)	The reaction proceeded via: GO: acid-catalysed Markovnikov addition Graphite: anti-Markovnikov addition	[92]

Table 2.3: (Continued)

Application	Key performances	Roles of GO	Refs.
Reduction of nitrobenzene to aniline	The k_{obs} increases up to 2 orders of magnitude; Na_2S: 7.83 x 10^{-5} h^{-1} Na_2S/GO: 7.77 x 10^{-3} h^{-1}	Enhanced electron transfer during the catalysis due to concomitant interactions between the zigzag edges (catalytic active sites) and basal plane of RGO (conductor)	[93]
Friedel–Crafts addition of α,β-unsaturated ketones to indoles	Enhance yield of substituted indoles: GO: 92% Activated carbon: 20%	The acidic characteristics of GO helps to stimulate the Friedel–Crafts addition reaction	[94]
Strecker reaction of ketones	Enhance yield of α-amino nitriles; GO: 94% Activated carbon: 5% Silica: 10%	Protonation of the carbonyl groups favours the nucleophilic addition by amine that subsequent proceed with the dehydration of the amino alcohol in facilitating the formation of the α-amino nitriles	[95]

2.4.2 GO as catalyst support/ co-catalyst

In addition to its inherent reactivity, GO has also been utilised as a support to disperse and stabilise metal and metal oxide NPs during heterogeneous catalysis in numerous catalytic applications [96-108]. Based on the literature, it was found that GO played a key role over other carbon supports by enhancing the overall catalytic performances through: (i) preventing the severe aggregation of metal and/or metal oxide NPs by promoting good dispersion of NPs onto GO sheets [99, 103, 104]; (ii) controlling the dispersibility of heterogeneous catalysts in aqueous solution based on unique solution behaviour of GO [101, 105, 109]; (iii) increasing the absorptivity of targeted pollutants which have a similar aromatic ring structure through π-π interactions within the vicinity of the active sites to be further oxidised/ reduced during the catalysis [110, 111]; (iv) extending the light absorption range [112]; (v) efficient charge transportation and separation to prevent the direct recombination of electrons and holes [87, 96, 113-115]; and (vi) inducing electronic perturbations in the metallic active sites [109].

The integration of GO and iron complexes or iron oxide NPs into a single composite has become a hot topic of research in catalysis [108, 116-123], as it inherits the advantages of both component materials. Of particular interest, the following paragraphs further discuss the current progress of GO supported-iron containing nanocomposites as heterogeneous (Fenton-like) catalysts for the degradation of persistent organic pollutants, specifically dyes. He et al. [120] investigated the catalytic performance of graphene oxide–iron oxide (GO–Fe_3O_4) nanocomposites for the reduction of nitrobenzene in the presence of hydrazine. The nanocomposites exhibited higher catalytic activity by having completed reduction in 18 min with the yield of aniline close to 99% with higher turnover frequency of 3.63 min^{-1} than that of Fe_3O_4 NPs, in which 15% of the reactant still remained within the same time, as shown in Figure 2.4a. This was due to the dispersion of Fe_3O_4 NPs on the surface of the GO sheets (Figure 2.4b) instead of aggregating during the catalysis.

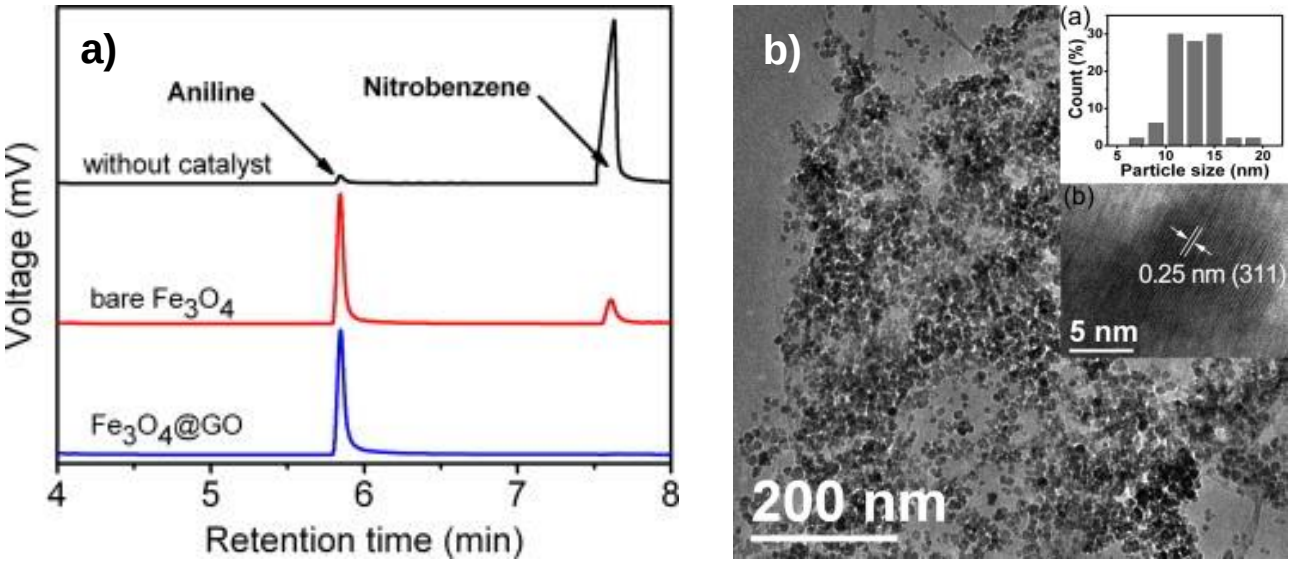

Figure 2.4: a) The GC analyses of the reduction of nitrobenzene in different reaction systems after 18 min and b) TEM image of GO–Fe_3O_4 nanocomposites [120].

Dong et al. [117] synthesised graphene oxide-Fe(III) complexes (GO–Fe) via an acidic impregnation method for the degradation of Rhodamine B dye (RhB) in both heterogeneous and photo Fenton-like reactions. Ferric ions were found to be successfully coordinated with oxygen functional groups of GO without having any formation of iron NPs derived from hydrolysis of ferric ions, as evidenced in both FTIR and TEM-EDX analysis. Figure 2.5a presents the normalised concentration of RhB profile, where nearly 38% of RhB degradation was attained in heterogeneous reaction within 120 min. In contrast, the enhancement of RhB degradation was found to be almost 100% within 45 min of irradiation, owing to the presence of sp^2 hybridised graphitic regions of GO that effectively facilitated

electron transfer between GO and iron centres to form reactive oxygen radical species under such conditions.

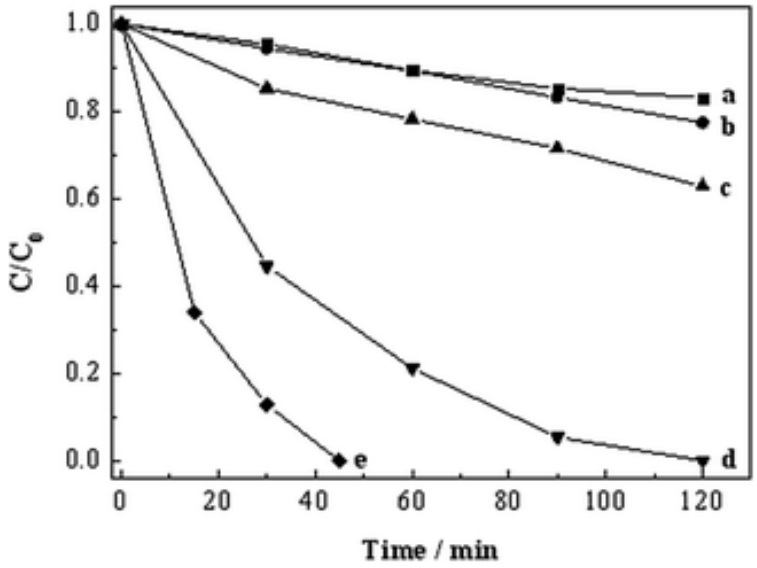

Figure 2.5: The normalised concentration of RhB profile under different conditions. (a) 20 mg L^{-1} GO–Fe, no H_2O_2 under visible-light irradiation; (b) 20 mg L^{-1} GO, 2 mM H_2O_2 under visible-light irradiation; (c) 20 mg L^{-1} GO–Fe, 2 mM H_2O_2 in the dark; (d) 5 mg L^{-1} and (e) 20 mg L^{-1} GO–Fe, 2 mM H_2O_2 under visible-light irradiation at pH = 3 [117].

Moreover, Guo et al. [118] also investigated similar catalytic performance using a graphene oxide-Fe_2O_3 (GO–Fe_2O_3) hybrid. Fe_2O_3 nanoparticles were deposited onto GO sheets by metal-carbonyl coordination. The GO–Fe_2O_3 exhibited 17% higher RhB degradation under the visible-light irradiation over heterogeneous Fenton-like reactions (±80%) after 80 min. The degradation was mainly attributed to heterogeneous reaction whereas the leached iron (3.98 mg L^{-1}) contributed only 40% of RhB degradation within the same time period (Figure 2.6a-curve g). This hybrid catalyst also demonstrated a broad applicability in pH range from 2.09 to 10.09 and stable photocatalytic activity without having any significant loss in performance (RhB removal of more than 90%) even after undergoing seven cycles of oxidative reaction (Figure 2.6b). These findings were attributed to the synergetic effects of the adsorptivity of GO and the formation of $HO^{\bullet}$ radicals during the heterogeneous photo-Fenton reactions.

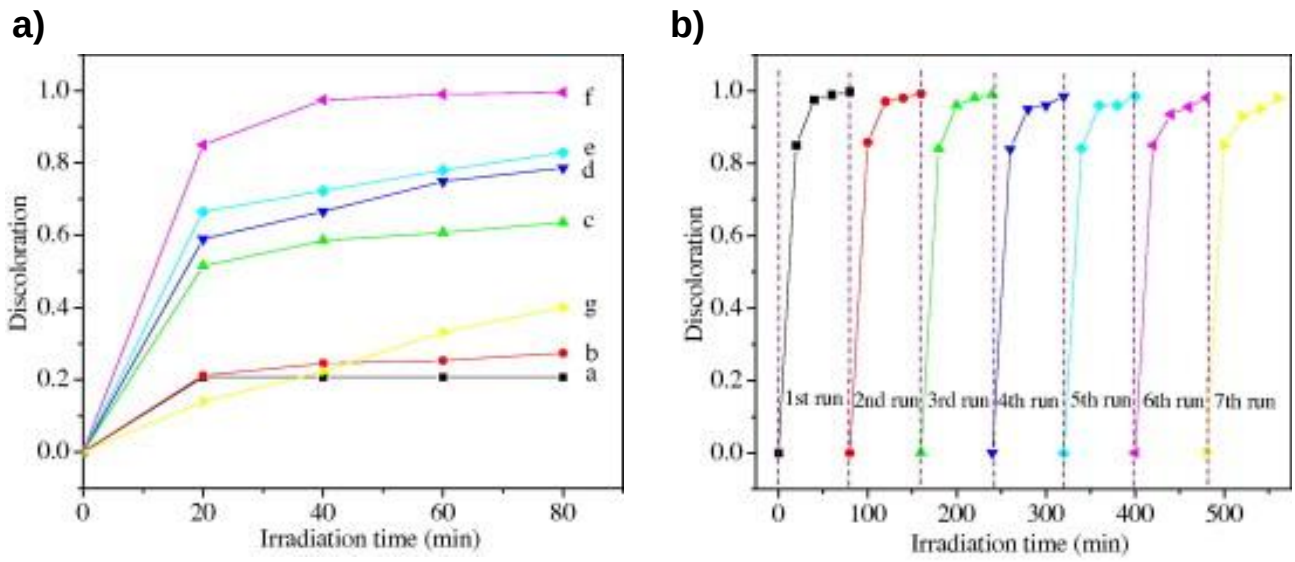

Figure 2.6: a) Discoloration of RhB under different conditions: a- RhB/H_2O_2/vis; b- RhB/H_2O_2, in the dark; c- RhB/GO–Fe_2O_3, in the dark; d- RhB/GO–Fe_2O_3/vis; e- RhB/GO–Fe_2O_3/H_2O_2,in the dark; f- RhB/GO–Fe_2O_3/H_2O_2/vis; g- RhB/Fe^{3+}/H_2O_2/vis and b) the long-term stability test of GO–Fe_2O_3 in the photo Fenton-like reaction [118].

Recently Hua et al. [123] reported the preparation of GO–Fe_3O_4 nanocomposites by the in-situ growth of Fe_3O_4 nanoparticles on the GO surface through the hydrothermal synthesis method. The Fe_3O_4 NPs were found to be homogeneously dispersed on the surface of GO (Figure 2.7a) with uniform particle sizes ~6 nm in diameter (Figure 2.7b). The GO–Fe_3O_4 nanocomposites enhanced the degradation of bisphenol A (BPA) by more than 8.5 times (> 85% BPA removal in 12 h) over the bare Fe_3O_4 NPs in the heterogeneous Fenton-like reaction (Figure 2.7c). This enhancement was attributed to the formation of small diameter and relatively uniform size of the Fe_3O_4 NPs successfully immobilised on the GO sheets. In addition, the synergistic effect of GO on the pre-concentration of BPA molecules aided in further oxidisation of BPA within the vicinity of catalyst active sites. These nanocomposites have shown good stability and reusability by sustaining more than 80% degradation of BPA over the three consecutive cycles of reaction as depicted in Figure 2.7d.

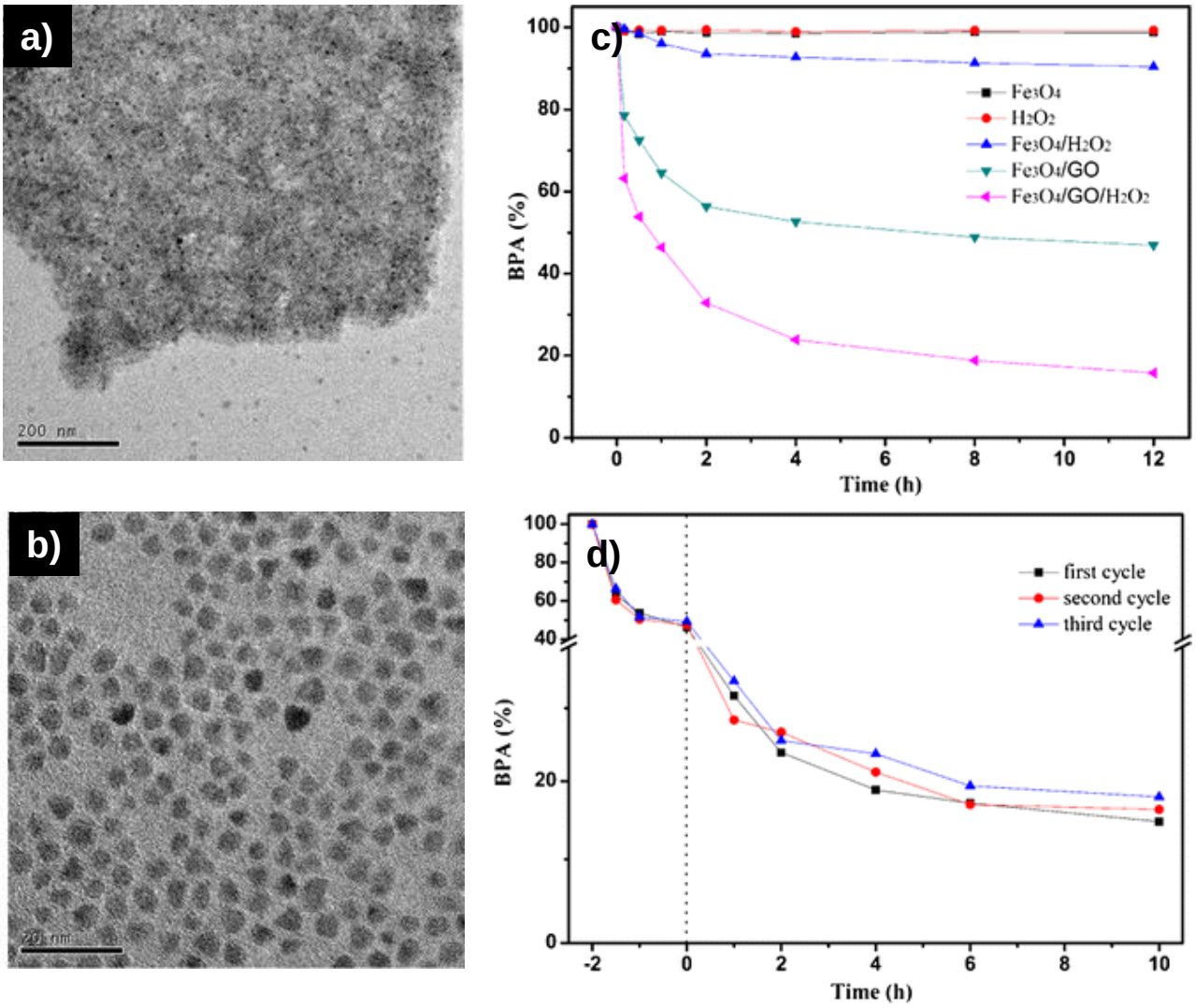

Figure 2.7: a) TEM and b) HRTEM images of GO–Fe_3O_4 nanocomposites, c) BPA degradation in different systems and d) the long-term stability test on the BPA degradation using GO–Fe_3O_4 nanocomposites. Experimental conditions: 20 mg L^{-1} BPA, 10 mM H_2O_2, 1 g L^{-1} catalyst dosage and pH 6 [123].

2.5 Summary

This review clearly shows that wastewater contamination by textile dyes requires processing to avert negative environmental impacts. Further, a great proportion of dyes are related to AO7, which is extensively used by the textile industry. Currently, there are several technologies that can be used to degrade organic dyes, and AOPs are currently the gold standard, especially via the Fenton-like reaction. However, one common feature of catalysts used in AOPs is the lack of stability and recyclability, which is a major gap in the literature that warrants further research. This is not a new problem and has been addressed by the research community with partial success only. The general

approach is to immobilise an active metal oxide or metal group on a support, with carbonaceous supports being the most promising materials. Despite having high catalytic performance for the removal of dyes (>90% removal) at the initial stage of reaction, these heterogeneous catalysts still suffer deactivation.

Therefore, the selection of a suitable catalyst support is crucial for the development of active and stable heterogeneous Fenton-like catalysts. Out of many carbonaceous supports to form supported heterogeneous catalysts, GO is considered as a potential candidate. In fact, GO has been proven to immobilise iron complexes and/or iron oxide NPs for the development of heterogeneous (Fenton-like) catalysts. From the findings of the recent progress on GO supported-iron containing nanocomposites as heterogeneous (Fenton-like) catalysts, it was found that GO has functionalities which may confer synergistic effects with iron oxides such as by: (i) facilitating the adsorption of target pollutants through π-π interactions; (ii) preventing the iron oxide NPs from aggregating; and (iii) facilitating the electron transfer between GO and iron centres due to the presence of sp^2 hybridised carbon domain on the basal planes.

Nevertheless, there are still knowledge gaps associated with: (i) a detailed formation mechanism of the GO supported-iron containing nanocomposites; (ii) understanding their structural-morphology and functionality relationships with respect to their catalytic activity; and (iii) the reaction mechanism in tandem with synergistic interactions and catalyst stability. There is a need to investigate the synergies of nanocomposites structure and GO functionalities, a knowledge of this is required to understand the optimal conditions in which the heterogeneous Fenton-like reaction can take place. A major hypothesis to be tested in this thesis is that a stable catalyst is based on the synergistic effect between the structure and functionality of the GO supported-iron containing nanocomposites. In this case, this thesis also endeavours to answer the question related to the mechanism responsible for the attainment of catalytic stability under the heterogeneous Fenton-like reaction. Finally, another knowledge gap is the effect of GO supported-iron containing nanocomposites under the UV-assisted heterogeneous Fenton-like reaction in enhancing catalytic activity. The role played by GO requires further understanding under these conditions. Therefore, these knowledge gaps raise important and relevant PhD questions, which are central to this thesis and subsequent investigations in the experimental chapters.

References

[1] V.M. Correia, T. Stephenson, S.J. Judd, Characterisation of textile wastewaters - a review, Environ. Technol. 15 (1994) 917-929.

[2] M. Aleksić, H. Kušić, N. Koprivanac, D. Leszczynska, A.L. Božić, Heterogeneous Fenton type processes for the degradation of organic dye pollutant in water — The application of zeolite assisted AOPs, Desalination 257 (2010) 22-29.

[3] V. Gómez, M.S. Larrechi, M.P. Callao, Kinetic and adsorption study of acid dye removal using activated carbon, Chemosphere 69 (2007) 1151-1158.

[4] V.K. Garg, R. Kumar, R. Gupta, Removal of malachite green dye from aqueous solution by adsorption using agro-industry waste: a case study of prosopis cineraria, Dyes Pigments 62 (2004) 1-10.

[5] S.H.S. Chan, T. Yeong Wu, J.C. Juan, C.Y. Teh, Recent developments of metal oxide semiconductors as photocatalysts in advanced oxidation processes (AOPs) for treatment of dye waste-water, J. Chem. Technol. Biot. 86 (2011) 1130-1158.

[6] V.K. Gupta, Suhas, Application of low-cost adsorbents for dye removal - a review, J. Environ. Manage. 90 (2009) 2313-2342.

[7] W.J. Epolito, Y.H. Lee, L.A. Bottomley, S.G. Pavlostathis, Characterization of the textile anthraquinone dye reactive blue 4, Dyes Pigments 67 (2005) 35-46.

[8] J.H. Ramirez, F.M. Duarte, F.G. Martins, C.A. Costa, L.M. Madeira, Modelling of the synthetic dye orange II degradation using Fenton's reagent: From batch to continuous reactor operation, Chem. Eng. J. 148 (2009) 394-404.

[9] E. Ember, S. Rothbart, R. Puchta, R. van Eldik, Metal ion-catalyzed oxidative degradation of orange II by H_2O_2. High catalytic activity of simple manganese salts, New J. Chem. 33 (2009) 34-49.

[10] N. Riaz, F.K. Chong, B.K. Dutta, Z.B. Man, M.S. Khan, E. Nurlaela, Photodegradation of orange II under visible light using Cu–Ni/TiO_2: Effect of calcination temperature, Chem. Eng. J. 185–186 (2012) 108-119.

[11] G. Li, J. Qu, X. Zhang, H. Liu, H. Liu, Electrochemically assisted photocatalytic degradation of orange II: Influence of initial pH values, J. Mol. Catal. A 259 (2006) 238-244.

[12] G. Li, K.H. Wong, X. Zhang, C. Hu, J.C. Yu, R.C.Y. Chan, P.K. Wong, Degradation of acid orange 7 using magnetic AgBr under visible light: The roles of oxidizing species, Chemosphere 76 (2009) 1185-1191.

[13] E. Forgacs, T. Cserháti, G. Oros, Removal of synthetic dyes from wastewaters: a review, Environ. Int. 30 (2004) 953-971.

[14] F.P. van der Zee, S. Villaverde, Combined anaerobic–aerobic treatment of azo dyes—a short review of bioreactor studies, Water Res. 39 (2005) 1425-1440.

[15] R. Fang, X. Cheng, X. Xu, Synthesis of lignin-base cationic flocculant and its application in removing anionic azo-dyes from simulated wastewater, Bioresource Technol. 101 (2010) 7323-7329.

[16] A.N. Soon, B.H. Hameed, Heterogeneous catalytic treatment of synthetic dyes in aqueous media using Fenton and photo-assisted Fenton process, Desalination 269 (2011) 1-16.

[17] L. Gomathi Devi, S. Girish Kumar, K. Mohan Reddy, C. Munikrishnappa, Photo degradation of methyl orange an azo dye by advanced Fenton process using zero valent metallic iron: Influence of various reaction parameters and its degradation mechanism, J. Hazard. Mater. 164 (2009) 459-467.

[18] S.P. Sun, C.J. Li, J.H. Sun, S.H. Shi, M.H. Fan, Q. Zhou, Decolorization of an azo dye orange G in aqueous solution by Fenton oxidation process: Effect of system parameters and kinetic study, J. Hazard. Mater. 161 (2009) 1052-1057.

[19] S. Karthikeyan, A. Titus, A. Gnanamani, A.B. Mandal, G. Sekaran, Treatment of textile wastewater by homogeneous and heterogeneous Fenton oxidation processes, Desalination 281 (2011) 438-445.

[20] E.G. Garrido-Ramírez, B.K.G. Theng, M.L. Mora, Clays and oxide minerals as catalysts and nanocatalysts in Fenton-like reactions — a review, Appl. Clay Sci. 47 (2010) 182-192.

[21] H. Bel Hadjltaief, P. Da Costa, P. Beaunier, M.E. Gálvez, M. Ben Zina, Fe-clay-plate as a heterogeneous catalyst in photo-Fenton oxidation of phenol as probe molecule for water treatment, Appl. Clay Sci. 91–92 (2014) 46-54.

[22] S.H. Tian, Y.T. Tu, D.S. Chen, X. Chen, Y. Xiong, Degradation of acid orange II at neutral pH using $Fe_2(MoO_4)_3$ as a heterogeneous Fenton-like catalyst, Chem. Eng. J. 169 (2011) 31-37.

[23] L. Núñez, J.A. García-Hortal, F. Torrades, Study of kinetic parameters related to the decolourization and mineralization of reactive dyes from textile dyeing using Fenton and photo-Fenton processes, Dyes Pigments 75 (2007) 647-652.

[24] P.P. Gan, S.F.Y. Li, Efficient removal of rhodamine B using a rice hull-based silica supported iron catalyst by Fenton-like process, Chem. Eng. J. 229 (2013) 351-363.

[25] J. Herney-Ramirez, A.M.T. Silva, M.A. Vicente, C.A. Costa, L.M. Madeira, Degradation of acid orange 7 using a saponite-based catalyst in wet hydrogen peroxide oxidation: Kinetic study with the Fermi's equation, Appl. Catal. B 101 (2011) 197-205.

[26] H. Hassan, B.H. Hameed, Fe–clay as effective heterogeneous Fenton catalyst for the decolorization of reactive blue 4, Chem. Eng. J. 171 (2011) 912-918.

[27] J. Herney-Ramirez, M. Lampinen, M.A. Vicente, C.A. Costa, L.M. Madeira, Experimental design to optimize the oxidation of orange II dye solution using a clay-based Fenton-like catalyst, Ind. Eng. Chem. Res. 47 (2007) 284-294.

[28] C.L. Hsueh, Y.H. Huang, C.Y. Chen, Novel activated alumina-supported iron oxide-composite as a heterogeneous catalyst for photooxidative degradation of reactive black 5, J. Hazard. Mater. 129 (2006) 228-233.

[29] H. Lim, J. Lee, S. Jin, J. Kim, J. Yoon, T. Hyeon, Highly active heterogeneous Fenton catalyst using iron oxide nanoparticles immobilized in alumina coated mesoporous silica, Chem. Commun. (2006) 463-465.

[30] M.L. Rache, A.R. García, H.R. Zea, A.M.T. Silva, L.M. Madeira, J.H. Ramírez, Azo-dye orange II degradation by the heterogeneous Fenton-like process using a zeolite Y-Fe catalyst—Kinetics with a model based on the Fermi's equation, Appl. Catal. B 146 (2014) 192-200.

[31] F.M. Duarte, F.J. Maldonado-Hódar, L.M. Madeira, Influence of the iron precursor in the preparation of heterogeneous Fe/activated carbon Fenton-like catalysts, Appl. Catal. A 458 (2013) 39-47.

[32] Y. Yao, L. Wang, L. Sun, S. Zhu, Z. Huang, Y. Mao, W. Lu, W. Chen, Efficient removal of dyes using heterogeneous Fenton catalysts based on activated carbon fibers with enhanced activity, Chem. Eng. Sci. 101 (2013) 424-431.

[33] X. Hu, B. Liu, Y. Deng, H. Chen, S. Luo, C. Sun, P. Yang, S. Yang, Adsorption and heterogeneous Fenton degradation of 17α-methyltestosterone on nano Fe_3O_4/MWCNTs in aqueous solution, Appl. Catal. B 107 (2011) 274-283.

[34] Y. Chen, S. Jin, J. Liu, B. Zhao, T. Wang, Photo-Fenton reaction of supported cationic cyclopentadienyl iron complexes of arene and application as heterogeneous catalysts in photodegradation of dyes under visible light, Inorg. Chim. Acta 406 (2013) 37-43.

[35] J. Feng, X. Hu, P.L. Yue, H.Y. Zhu, G.Q. Lu, A novel laponite clay-based Fe nanocomposite and its photo-catalytic activity in photo-assisted degradation of orange II, Chem. Eng. Sci. 58 (2003) 679-685.

[36] J. Chen, L. Zhu, Comparative study of catalytic activity of different Fe-pillared bentonites in the presence of UV light and H_2O_2, Sep. Purif. Technol. 67 (2009) 282-288.

[37] M. Dükkancı, G. Gündüz, S. Yılmaz, R.V. Prihod'ko, Heterogeneous Fenton-like degradation of rhodamine 6G in water using CuFeZSM-5 zeolite catalyst prepared by hydrothermal synthesis, J. Hazard. Mater. 181 (2010) 343-350.

[38] L. Guo, F. Chen, X. Fan, W. Cai, J. Zhang, S-doped α-Fe_2O_3 as a highly active heterogeneous Fenton-like catalyst towards the degradation of acid orange 7 and phenol, Appl. Catal. B 96 (2010) 162-168.

[39] N. Panda, H. Sahoo, S. Mohapatra, Decolourization of methyl orange using Fenton-like mesoporous Fe_2O_3–SiO_2 composite, J. Hazard. Mater. 185 (2011) 359-365.

[40] J. Feng, X. Hu, P.L. Yue, Discoloration and mineralization of orange II using different heterogeneous catalysts containing Fe: A comparative study, Environ. Sci. Technol. 38 (2004) 5773-5778.

[41] J. Feng, X. Hu, P.L. Yue, H.Y. Zhu, G.Q. Lu, Discoloration and mineralization of reactive red HE-3B by heterogeneous photo-Fenton reaction, Water Res. 37 (2003) 3776-3784.

[42] N. Ferroudj, J. Nzimoto, A. Davidson, D. Talbot, E. Briot, V. Dupuis, A. Bée, M.S. Medjram, S. Abramson, Maghemite nanoparticles and maghemite/silica nanocomposite microspheres as magnetic Fenton catalysts for the removal of water pollutants, Appl. Catal. B 136–137 (2013) 9-18.

[43] O.U. Rahman, S.C. Mohapatra, S. Ahmad, Fe_3O_4 inverse spinal super paramagnetic nanoparticles, Mater. Chem. Phys. 132 (2012) 196-202.

[44] S.-P. Sun, A.T. Lemley, p-Nitrophenol degradation by a heterogeneous Fenton-like reaction on nano-magnetite: Process optimization, kinetics, and degradation pathways, J. Mol. Catal. A 349 (2011) 71-79.

[45] X. Xue, K. Hanna, N. Deng, Fenton-like oxidation of rhodamine B in the presence of two types of iron (II, III) oxide, J. Hazard. Mater. 166 (2009) 407-414.

[46] R.C.C. Costa, M.F.F. Lelis, L.C.A. Oliveira, J.D. Fabris, J.D. Ardisson, R.R.V.A. Rios, C.N. Silva, R.M. Lago, Novel active heterogeneous Fenton system based on $Fe_{3-x}M_xO_4$ (Fe, Co, Mn, Ni): The role of M^{2+} species on the reactivity towards H_2O_2 reactions, J. Hazard. Mater. 129 (2006) 171-178.

[47] R.C.C. Costa, F.C.C. Moura, J.D. Ardisson, J.D. Fabris, R.M. Lago, Highly active heterogeneous Fenton-like systems based on Fe^0/Fe_3O_4 composites prepared by controlled reduction of iron oxides, Appl. Catal. B 83 (2008) 131-139.

[48] P.V. Nidheesh, R. Gandhimathi, S. Velmathi, N.S. Sanjini, Magnetite as a heterogeneous electro Fenton catalyst for the removal of rhodamine B from aqueous solution, RSC Adv. 4 (2014) 5698-5708.

[49] M. Zhu, G. Diao, Synthesis of porous Fe_3O_4 nanospheres and its application for the catalytic degradation of xylenol orange, J. Phys. Chem. C 115 (2011) 18923-18934.

[50] T. Shahwan, S. Abu Sirriah, M. Nairat, E. Boyacı, A.E. Eroğlu, T.B. Scott, K.R. Hallam, Green synthesis of iron nanoparticles and their application as a Fenton-like catalyst for the degradation of aqueous cationic and anionic dyes, Chem. Eng. J. 172 (2011) 258-266.

[51] G. Zhang, S. Wang, F. Yang, Efficient adsorption and combined heterogeneous/homogeneous Fenton oxidation of amaranth using supported nano-FeOOH as cathodic catalysts, J. Phys. Chem. C 116 (2012) 3623-3634.

[52] W.P. Kwan, B.M. Voelker, Rates of hydroxyl radical generation and organic compound oxidation in mineral-catalyzed Fenton-like systems, Environ. Sci.Technol. 37 (2003) 1150-1158.

[53] R. Matta, K. Hanna, S. Chiron, Fenton-like oxidation of 2,4,6-trinitrotoluene using different iron minerals, Sci. Total Environ. 385 (2007) 242-251.

[54] Y. Zhong, X. Liang, Z. He, W. Tan, J. Zhu, P. Yuan, R. Zhu, H. He, The constraints of transition metal substitutions (Ti, Cr, Mn, Co and Ni) in magnetite on its catalytic activity in heterogeneous Fenton and UV/Fenton reaction: From the perspective of hydroxyl radical generation, Appl. Catal. B 150-151 (2014) 612-618.

[55] X. Liang, Z. He, G. Wei, P. Liu, Y. Zhong, W. Tan, P. Du, J. Zhu, H. He, J. Zhang, The distinct effects of Mn substitution on the reactivity of magnetite in heterogeneous Fenton reaction and Pb(II) adsorption, J. Colloid Interf. Sci. 426 (2014) 181-189.

[56] X. Liang, Z. He, Y. Zhong, W. Tan, H. He, P. Yuan, J. Zhu, J. Zhang, The effect of transition metal substitution on the catalytic activity of magnetite in heterogeneous Fenton reaction: In interfacial view, Colloids Surfaces A 435 (2013) 28-35.

[57] Y. Zhong, X. Liang, W. Tan, Y. Zhong, H. He, J. Zhu, P. Yuan, Z. Jiang, A comparative study about the effects of isomorphous substitution of transition metals (Ti, Cr, Mn, Co and Ni) on the UV/Fenton catalytic activity of magnetite, J. Mol. Catal. A 372 (2013) 29-34.

[58] L. Menini, M.C. Pereira, L.A. Parreira, J.D. Fabris, E.V. Gusevskaya, Cobalt- and manganese-substituted ferrites as efficient single-site heterogeneous catalysts for aerobic oxidation of monoterpenic alkenes under solvent-free conditions, J. Catal. 254 (2008) 355-364.

[59] L. Gao, J. Zhuang, L. Nie, J. Zhang, Y. Zhang, N. Gu, T. Wang, J. Feng, D. Yang, S. Perrett, X. Yan, Intrinsic peroxidase-like activity of ferromagnetic nanoparticles, Nat. Nano. 2 (2007) 577-583.

[60] M. Sedlacik, R. Moucka, Z. Kozakova, N.E. Kazantseva, V. Pavlinek, I. Kuritka, O. Kaman, P. Peer, Correlation of structural and magnetic properties of Fe_3O_4 nanoparticles with their calorimetric and magnetorheological performance, J. Magn. Magn. Mater. 326 (2013) 7-13.

[61] C. Yang, J. Wu, Y. Hou, Fe_3O_4 nanostructures: synthesis, growth mechanism, properties and applications, Chem. Commun. 47 (2011) 5130-5141.

[62] H. Wei, E. Wang, Fe_3O_4 magnetic nanoparticles as peroxidase mimetics and their applications in H_2O_2 and glucose detection, Anal. Chem. 80 (2008) 2250-2254.

[63] O. Taran, E. Polyanskaya, O. Ogorodnikova, V. Kuznetsov, V. Parmon, M. Besson, C. Descorme, Influence of the morphology and the surface chemistry of carbons on their catalytic performances in the catalytic wet peroxide oxidation of organic contaminants, Appl. Catal. A 387 (2010) 55-66.

[64] C.M. Domínguez, A. Quintanilla, P. Ocón, J.A. Casas, J.J. Rodriguez, The use of cyclic voltammetry to assess the activity of carbon materials for hydrogen peroxide decomposition, Carbon 60 (2013) 76-83.

[65] J.H. Ramirez, F.J. Maldonado-Hódar, A.F. Pérez-Cadenas, C. Moreno-Castilla, C.A. Costa, L.M. Madeira, Azo-dye orange II degradation by heterogeneous Fenton-like reaction using carbon-Fe catalysts, Appl. Catal. B 75 (2007) 312-323.

[66] N. Thi Dung, P. Ngoc Hoa, D. Manh Huy, N. Kim Tham, Magnetic Fe_2MO_4 (M:Fe, Mn) activated carbons: Fabrication, characterization and heterogeneous Fenton oxidation of methyl orange, J. Hazard. Mater.185 (2011) 653-661.

[67] F. Duarte, F.J. Maldonado-Hódar, A.F. Pérez-Cadenas, L.M. Madeira, Fenton-like degradation of azo-dye Orange II catalyzed by transition metals on carbon aerogels, Appl. Catal. B 85 (2009) 139-147.

[68] K. Yao, J. Gong, J. Zheng, L. Wang, H. Tan, G. Zhang, Y. Lin, H. Na, X. Chen, X. Wen, T. Tang, Catalytic carbonization of chlorinated poly(vinyl chloride) microfibers into carbon microfibers with high performance in the photodegradation of congo red, J. Phys. Chem. C 117 (2013) 17016-17023.

[69] H.-J. Tang, T.-T. Han, Z.-J. Luo, X.-Y. Wu, Magnetite/N-doped carboxylate-rich carbon spheres: Synthesis, characterization and visible-light-induced photocatalytic properties, Chinese Chem. Lett. 24 (2013) 63-66.

[70] L. Gu, N. Zhu, H. Guo, S. Huang, Z. Lou, H. Yuan, Adsorption and Fenton-like degradation of naphthalene dye intermediate on sewage sludge derived porous carbon, J. Hazard. Mater. 246–247 (2013) 145-153.

[71] H. Wang, H. Jiang, S. Wang, W. Shi, J. He, H. Liu, Y. Huang, Fe_3O_4-MWCNT magnetic nanocomposites as efficient peroxidase mimic catalysts in a Fenton-like reaction for water purification without pH limitation, RSC Adv. 4 (2014) 45809-45815.

[72] J. Deng, X. Wen, Q. Wang, Solvothermal in situ synthesis of Fe_3O_4-multi-walled carbon nanotubes with enhanced heterogeneous Fenton-like activity, Mater. Res. Bull. 47 (2012) 3369-3376.

[73] K. Pirkanniemi, M. Sillanpää, Heterogeneous water phase catalysis as an environmental application: a review, Chemosphere 48 (2002) 1047-1060.

[74] S. Navalon, A. Dhakshinamoorthy, M. Alvaro, H. Garcia, Heterogeneous Fenton catalysts based on activated carbon and related materials, ChemSusChem 4 (2011) 1712-1730.

[75] M.I. Kim, J.S. Im, S.-J. In, H. Kim, J.-G. Kim, Y.-S. Lee, Improved photo degradation of rhodamine B dye using iron oxide/carbon nanocomposite by photo-Fenton reaction, Carbon Lett. 9 (2008) 95-199.

[76] K.V. Voitko, R.L.D. Whitby, V.M. Gun'ko, O.M. Bakalinska, M.T. Kartel, K. Laszlo, A.B. Cundy, S.V. Mikhalovsky, Morphological and chemical features of nano and macroscale carbons affecting hydrogen peroxide decomposition in aqueous media, J.Colloid Interf. Sci. 361 (2011) 129-136.

[77] D.R. Dreyer, S. Park, C.W. Bielawski, R.S. Ruoff, The chemistry of graphene oxide, Chem. Soc. Rev. 39 (2010) 228-240.

[78] A. Lerf, H. He, M. Forster, J. Klinowski, Structure of graphite oxide revisited[I], J. Phys. Chem. B, 102 (1998) 4477-4482.

[79] C. Su, K.P. Loh, Carbocatalysts: Graphene oxide and its derivatives, Accounts Chem. Res. 46 (2013) 2275-2285.

[80] D.R. Dreyer, A.D. Todd, C.W. Bielawski, Harnessing the chemistry of graphene oxide, Chem. Soc. Rev. 43 (2014) 5288-5301.

[81] G.K. Ramesha, A. Vijaya Kumara, H.B. Muralidhara, S. Sampath, Graphene and graphene oxide as effective adsorbents toward anionic and cationic dyes, J. Colloid Interf. Sci. 361 (2011) 270-277.

[82] M.Z. Kassaee, E. Motamedi, M. Majdi, Magnetic Fe_3O_4-graphene oxide/polystyrene: Fabrication and characterization of a promising nanocomposite, Chem. Eng. J. 172 (2011) 540-549.

[83] Y. Matsumoto, M. Koinuma, S. Ida, S. Hayami, T. Taniguchi, K. Hatakeyama, H. Tateishi, Y. Watanabe, S. Amano, Photoreaction of graphene oxide nanosheets in water, J. Phys. Chem. C 115 (2011) 19280-19286.

[84] K.P. Loh, Q. Bao, G. Eda, M. Chhowalla, Graphene oxide as a chemically tunable platform for optical applications, Nat. Chem. 2 (2010) 1015-1024.

[85] L.M. Pastrana-Martínez, S. Morales-Torres, V. Likodimos, J.L. Figueiredo, J.L. Faria, P. Falaras, A.M.T. Silva, Advanced nanostructured photocatalysts based on reduced graphene oxide–TiO_2 composites for degradation of diphenhydramine pharmaceutical and methyl orange dye, Appl. Catal. B 123–124 (2012) 241-256.

[86] A. Bagri, C. Mattevi, M. Acik, Y.J. Chabal, M. Chhowalla, V.B. Shenoy, Structural evolution during the reduction of chemically derived graphene oxide, Nat. Chem. 2 (2010) 581-587.

[87] G. Liao, S. Chen, X. Quan, H. Yu, H. Zhao, Graphene oxide modified g-C_3N_4 hybrid with enhanced photocatalytic capability under visible light irradiation, J. Mater. Chem. 22 (2012) 2721-2726.

[88] D.R. Dreyer, Graphene Oxide: A convenient carbocatalyst for facilitating oxidation and hydration reactions, Angew. Chem. Int. Edit. 49 (2010) 6813-6816.

[89] D.R. Dreyer, H.-P. Jia, A.D. Todd, J. Geng, C.W. Bielawski, Graphite oxide: a selective and highly efficient oxidant of thiols and sulfides, Org. Biomol. Chem. 9 (2011) 7292-7295.

[90] D.R. Dreyer, C.W. Bielawski, Graphite oxide as an olefin polymerization carbocatalyst: Applications in electrochemical double layer capacitors, Adv. Funct. Mater. 22 (2012) 3247-3253.

[91] S. Verma, H.P. Mungse, N. Kumar, S. Choudhary, S.L. Jain, B. Sain, O.P. Khatri, Graphene oxide: an efficient and reusable carbocatalyst for aza-Michael addition of amines to activated alkenes, Chem. Commun. 47 (2011) 12673-12675.

[92] B. Basu, S. Kundu, D. Sengupta, Graphene oxide as a carbocatalyst: the first example of a one-pot sequential dehydration-hydrothiolation of secondary aryl alcohols, RSC Adv. 3 (2013) 22130-22134.

[93] H. Fu, D. Zhu, Graphene oxide-facilitated reduction of nitrobenzene in sulfide-containing aqueous solutions, Environ. Sci. Technol. 47 (2013) 4204-4210.

[94] A. Vijay Kumar, Recyclable graphite oxide catalyzed Friedel–Crafts addition of indoles to α,β-unsaturated ketones, Tetrahedron Lett. 52 (2011) 5188-5191.

[95] A. Sengupta, Graphene oxide and its functionalized derivatives as carbocatalysts in the multicomponent Strecker reaction of ketones, ChemCatChem 6 (2014) 2507-2511.

[96] J. Hou, Z. Wang, W. Kan, S. Jiao, H. Zhu, R.V. Kumar, Efficient visible-light-driven photocatalytic hydrogen production using CdS@TaON core-shell composites coupled with graphene oxide nanosheets, J. Mater. Chem. 22 (2012) 7291-7299.

[97] W.G. Hong, B.H. Kim, S.M. Lee, H.Y. Yu, Y.J. Yun, Y. Jun, J.B. Lee, H.J. Kim, Agent-free synthesis of graphene oxide/transition metal oxide composites and its application for hydrogen storage, Int. J. Hydrogen Energ. 37 (2012) 7594-7599.

[98] N.S. Andryushina, O.L. Stroyuk, Influence of colloidal graphene oxide on photocatalytic activity of nanocrystalline TiO_2 in gas-phase ethanol and benzene oxidation, Appl. Catal. B 148-149 (2014) 543-549.

[99] J. Bian, M. Xiao, S.J. Wang, Y.X. Lu, Y.Z. Meng, Graphite oxide as a novel host material of catalytically active Cu–Ni bimetallic nanoparticles, Catal. Commun. 10 (2009) 1529-1533.

[100] Á. Mastalir, Z. Király, Á. Patzkó, I. Dékány, P. L'Argentiere, Synthesis and catalytic application of Pd nanoparticles in graphite oxide, Carbon 46 (2008) 1631-1637.

[101] F. Bei, X. Hou, S.L.Y. Chang, G.P. Simon, D. Li, Interfacing colloidal graphene oxide sheets with gold nanoparticles, Chem. Eur. J. 17 (2011) 5958-5964.

[102] P. Shi, X. Dai, H. Zheng, D. Li, W. Yao, C. Hu, Synergistic catalysis of Co_3O_4 and graphene oxide on Co_3O_4/GO catalysts for degradation of orange II in water by advanced oxidation technology based on sulfate radicals, Chem. Eng. J. 240 (2014) 264 - 270.

[103] P. Shi, R. Su, S. Zhu, M. Zhu, D. Li, S. Xu, Supported cobalt oxide on graphene oxide: Highly efficient catalysts for the removal of orange II from water, J. Hazard. Mater. 229–230 (2012) 331-339.

[104] J.W. Zhu, G.Y. Zeng, F.D. Nie, X.M. Xu, S. Chen, Q.F. Han, X. Wang, Decorating graphene oxide with CuO nanoparticles in a water-isopropanol system, Nanoscale 2 (2010) 988-994.

[105] D. Verma, S. Verma, A.K. Sinha, S.L. Jain, Iron nanoparticles supported on graphene oxide: A robust, magnetically separable heterogeneous catalyst for the oxidative cyanation of tertiary amines, ChemPlusChem 78 (2013) 860-865.

[106] J. Zhu, M. Xu, X. Meng, K. Shang, H. Fan, S. Ai, Electro-enzymatic degradation of carbofuran with the graphene oxide–Fe_3O_4–hemoglobin composite in an electrochemical reactor, Process Biochem. 47 (2012) 2480-2486.

[107] Y. Song, Z. He, H. Hou, X. Wang, L. Wang, Architecture of Fe_3O_4–graphene oxide nanocomposite and its application as a platform for amino acid biosensing, Electrochim. Acta, 71 (2012) 58-65.

[108] Y.-L. Dong, H.-G. Zhang, Z.U. Rahman, L. Su, X.-J. Chen, J. Hu, X.-G. Chen, Graphene oxide-Fe_3O_4 magnetic nanocomposites with peroxidase-like activity for colorimetric detection of glucose, Nanoscale 4 (2012) 3969-3976.

[109] J. Huang, L. Zhang, B. Chen, N. Ji, F. Chen, Y. Zhang, Z. Zhang, Nanocomposites of size-controlled gold nanoparticles and graphene oxide: Formation and applications in SERS and catalysis, Nanoscale 2 (2010) 2733-2738.

[110] J. Liu, H. Bai, Y. Wang, Z. Liu, X. Zhang, D.D. Sun, Self-assembling TiO_2 nanorods on large graphene oxide sheets at a two-phase interface and their anti-recombination in photocatalytic applications, Adv. Funct. Mater. 20 (2010) 4175-4181.

[111] W. Lu, R. Ning, X. Qin, Y. Zhang, G. Chang, S. Liu, Y. Luo, X. Sun, Synthesis of Au nanoparticles decorated graphene oxide nanosheets: Noncovalent functionalization by TWEEN 20 in situ reduction of aqueous chloroaurate ions for hydrazine detection and catalytic reduction of 4-nitrophenol, J. Hazard. Mater. 197 (2011) 320-326.

[112] S.Q. Liu, B. Xiao, L.R. Feng, S.S. Zhou, Z.G. Chen, C.B. Liu, F. Chen, Z.Y. Wu, N. Xu, W.C. Oh, Z.D. Meng, Graphene oxide enhances the Fenton-like photocatalytic activity of nickel ferrite for degradation of dyes under visible light irradiation, Carbon 64 (2013) 197-206.

[113] B. Li, T. Liu, Y. Wang, Z. Wang, ZnO/graphene-oxide nanocomposite with remarkably enhanced visible-light-driven photocatalytic performance, J. Colloid Interf. Sci. 377 (2012) 114-121.

[114] C. Chen, W. Cai, M. Long, B. Zhou, Y. Wu, D. Wu, Y. Feng, Synthesis of visible-light responsive graphene oxide/TiO_2 composites with p/n heterojunction, ACS Nano 4 (2010) 6425-6432.

[115] J. Liu, L. Liu, H. Bai, Y. Wang, D.D. Sun, Gram-scale production of graphene oxide–TiO_2 nanorod composites: Towards high-activity photocatalytic materials, Appl. Catal. B 106 (2011) 76-82.

[116] F. Li, J. Zhao, Z. Chen, Fe-anchored graphene oxide: A low-cost and easily accessible catalyst for low-temperature CO oxidation, J. Phys. Chem. C 116 (2012) 2507-2514.

[117] Y. Dong, J. Li, L. Shi, J. Xu, X. Wang, Z. Guo, W. Liu, Graphene oxide-iron complex: synthesis, characterization and visible-light-driven photocatalysis, J. Mater. Chem. A 1 (2013) 644-650.

[118] S. Guo, G. Zhang, Y. Guo, J.C. Yu, Graphene oxide–Fe_2O_3 hybrid material as highly efficient heterogeneous catalyst for degradation of organic contaminants, Carbon 60 (2013) 437-444.

[119] Q. Chang, J. Huang, G. Jiang, H. Tang, L. De, Immobilization of horseradish peroxidase onto graphene oxide/Fe_3O_4 magnetic nanoparticles and its use for degradation of phenols, Chinese J. Environ. Eng. 8 (2014) 1812-1816.

[120] G. He, W. Liu, X. Sun, Q. Chen, X. Wang, H. Chen, Fe_3O_4@graphene oxide composite: A magnetically separable and efficient catalyst for the reduction of nitroarenes, Mater. Res. Bull. 48 (2013) 1885-1890.

[121] J. Huang, Q. Chang, Y. Ding, X. Han, H. Tang, Catalytic oxidative removal of 2,4-dichlorophenol by simultaneous use of horseradish peroxidase and graphene oxide/Fe_3O_4 as catalyst, Chem. Eng. J. 254 (2014) 434-442.

[122] J. Mondal, K.T. Nguyen, A. Jana, K. Kurniawan, P. Borah, Y. Zhao, A. Bhaumik, Efficient alkene hydrogenation over a magnetically recoverable and recyclable Fe_3O_4@GO nanocatalyst using hydrazine hydrate as the hydrogen source, Chem. Commun. 50 (2014) 12095-12097.

[123] Z. Hua, W. Ma, X. Bai, R. Feng, L. Yu, X. Zhang, Z. Dai, Heterogeneous Fenton degradation of bisphenol A catalyzed by efficient adsorptive Fe_3O_4/GO nanocomposites, Environ. Sci. Pollut. Res. (2014) 1-9.

Chapter 3

Graphene oxide–iron oxide ($GO–Fe_3O_4$) nanocomposites as an alternative heterogeneous Fenton-like catalyst

3.1 Introduction

The aim of chapter 3 was to synthesise, characterise and investigate the performance of graphene oxide–iron oxide ($GO–Fe_3O_4$) nanocomposites as an alternative heterogeneous Fenton-like catalyst for the degradation of persistent organic pollutants, particularly dyes. The incorporation of GO as catalyst support in immobilising Fe_3O_4 nanoparticles (NPs) was hypothesised to be able in enhancing the inherent catalytic activity of Fe_3O_4 NPs. The catalytic performance of $GO–Fe_3O_4$ nanocomposites were evaluated by taking into account of their reactivity for the oxidative degradation of acid orange 7 (AO7) as the model pollutant in the heterogeneous Fenton-like reaction.

3.2 Contributions

This chapter investigates the feasibility of using $GO–Fe_3O_4$ nanocomposites as an alternative heterogeneous Fenton-like catalyst and also the influence of GO in enhancing the overall catalytic performances during the catalysis. The major contribution of this work was the related to the formation mechanism of the $GO–Fe_3O_4$ nanocomposites. In fact, the findings of this work have proven that the incorporation of GO as catalyst support led to an enhancement on the catalytic performance of AO7 degradation over the control catalysts of Fe_3O_4 NPs and GO sheets.

AMERICAN SCIENTIFIC PUBLISHERS

Science of Advanced Materials
Vol. 6, pp. 1382–1388, 2014
(www.aspbs.com/sam)

ARTICLE

Fenton-Like Degradation of Acid Orange 7 Using Graphene Oxide-Iron Oxide Nanocomposite

Nor Aida Zubir[1,2], Xiwang Zhang[1], Christelle Yacou[1], and João C. Diniz da Costa[1,*]

[1]*FIMLab—Films and Inorganic Membrane Laboratory, School of Chemical Engineering, The University of Queensland, Brisbane, Qld 4072, Australia*
[2]*Faculty of Chemical Engineering, Universiti Teknologi MARA (UiTM), 13500 Pulau Pinang, Malaysia*

ABSTRACT

This work presents a facile, scalable method for the fabrication of graphene oxide-iron oxide (GO-Fe_3O_4) nanocomposites produced by co-precipitation of iron ions onto the GO surfaces in basic aqueous media. FTIR and XRD characterisation suggests that Fe_3O_4 was chemically anchored to the GO sheets, possibly via the carboxyl and hydroxyl groups. Small GO loadings of 0.5 and 1 wt% were not sufficient to alter the Fe_3O_4 structures. However, increasing the GO loading to 5 and 10 wt% resulted in significant loss in pore volume, thus suggesting the lamellar GO sheets decorated with Fe_3O_4 were assembling into GO-Fe_3O_4 nanocomposite stacks. It was found that the GO-Fe_3O_4 nanocomposites had an enhanced catalytic activity in the heterogeneous Fenton-like oxidation of Acid Orange 7 (AO7) compared to pure GO flat sheets and Fe_3O_4 nanoparticles. Interestingly, the GO-Fe_3O_4 nanocomposite with 5 wt% loading ratio exhibited the best catalytic activity with 76% degradation of AO7 dye observed within 90 min of reaction. This was attributed to the synergistic effect of GO by enriching the adsorbed AO7 molecules onto the nanocomposite to be further oxidised in the vicinities of active sites. This finding suggests the promising employment of GO-Fe_3O_4 nanocomposites in removing organic dyes from polluted water by heterogeneous Fenton-like reaction.

KEYWORDS: Graphene Oxide, Iron Oxide, Nanocomposites, Fenton-Like Reaction, Acid Orange 7.

1. INTRODUCTION

Environmental protection continues to become increasingly important and this is evident by the deployment of stringent treatment regulations dealing with the reclamation and disposal of dye contaminated wastewaters from textile, paper, plastics and related industries. In fact, the World Bank estimates that 17 to 20% of industrial water pollution emanates from textile dyeing and treatment processes.[1] The discharge of dye contaminated wastewaters to the environment has led to serious concerns from both aesthetic and environmental points of view. The presence of a dyes' colour is often visible, even at concentrations as low as 1 ppm.[2] More importantly, these wastewaters are considered carcinogenic, mutagenic and toxic at these concentrations.[3] As regulations become more stringent, the treatment and discharge of dye contaminated wastewaters is compulsory, highly regulated and enforced. Various treatments such as physico-chemical and biological processes have been widely investigated,[4–6] where considerable attention has been paid to advanced oxidation processes (AOPs). AOPs have attractive features such as highly potent and strongly oxidizing radicals, which allow for the destruction of wide range of organic pollutants.[3,7]

One of the most intensively studied AOP is based on the Fenton reaction. The active sites in the Fenton process are derived from iron ions, which serve as catalysts that break down the peroxide (H_2O_2) molecules into numerous hydroxyl radicals (OH) which are capable of decomposing persistent organic pollutants, including dye. However, the homogeneous Fenton process possesses several drawbacks, including the necessity for post-treatment prior to discharge due to the formation of iron hydroxide sludge, narrow pH range of 2.5–3.5, and unattainable regeneration of catalyst.[8] Therefore, the development of active and stable heterogeneous Fenton-like catalysts emerged as an interesting alternative, where various iron species are immobilized within the structure of different catalyst supports such as activated carbon, clay, alumina, ion exchange resin and zeolite.[9–14] In heterogeneous catalysts, the oxidation reactions mainly occur at the solid-liquid interfaces. As a result, significant reduction iron dissolution can be achieved reducing precipitation into sludge, as the iron remains either in the solid phase as a mineral or as an adsorbed ion. Due to this fact, the catalysts can mediate Fenton-like reactions at wider pH range and can also

*Author to whom correspondence should be addressed.
Email: j.dacosta@uq.edu.au
Received: 30 September 2012
Accepted: 12 May 2013

be recovered and regenerated for successive operations as well.

The use of carbonaceous materials as a support for immobilizing active catalysts has been well proven due to its uniqueness in acting as a co-catalyst. One example is the graphitic structure which could act in the same way with iron ions in the Fenton reaction.[15] Graphene is one of many carbon allotropes that have drawn considerable attention because of their unusual electronic transport properties and ability to improve catalytic properties.[16–19] Graphene oxide (GO), a derivative of graphene, has also shown to be a promising candidate for the catalytic support and carrier in chemical reactions, or for sorption, filtration and separation materials in environmental applications.[20–23] Liao et al.[22] suggested that the adjustable oxygenated functional groups of GO facilitate surface modification, thus favouring GO as host material for compositing with other materials. Moreover, Lu et al.[23] reported that the GO plays an active part in the catalysis through the pre-concentration of 4-nitrophenol that is then reduced within the vicinity of catalyst active sites.

This work proposes a novel approach to use GO as the catalyst support for catalysis, especially in the Fenton reaction system. We therefore report for the first time the immobilization of the iron species onto the GO surface aimed at taking advantage of the possible synergistic effect between GO and iron species in the Fenton reaction. Herein we investigate a facile and scalable approach towards the synthesis of GO-iron oxide (GO-Fe_3O_4) nanocomposites by a chemical precipitation method. The catalytic performance of GO-Fe_3O_4 nanocomposites were evaluated by taking into account of their reactivity for the oxidation of Acid Orange 7 (AO7) as the model pollutant in the heterogeneous Fenton-like reaction.

2. EXPERIMENTAL DETAILS

2.1. Synthesis of GO

All chemicals were of analytical grade and used as received. GO was synthesized by oxidation of graphite flake (Aldrich) using the modified Hummers method.[16, 24] Natural graphite (2.5 g) was mixed with $NaNO_3$ (1.25 g) in a beaker prior to the addition of H_2SO_4 (98 wt%, 60 mL). The mixture was equilibrated in an ice-water bath prior to the gradual addition of potassium permanganate (7.5 g) under vigorous stirring. The solution was maintained below 20 ° C to control the exothermic reaction and was kept stirring at a controlled cold temperature for 2 h. The mixture was then removed from the ice-water bath and stirred at room temperature overnight until a pasty consistency with a brownish colour was obtained. Next, deionized water (135 mL) was added slowly to the paste while being stirred vigorously. The mixture was then heated to 98 °C for 1 h in an oil bath and subsequently cooled down to room temperature. The reaction was terminated by adding H_2O_2 (30 wt%, 25 mL) to reduce the residual permanganate and manganese dioxide into colourless manganese sulphate. The mixture turned from brown to bright yellow after the peroxide treatment. Subsequently, the mixture was filtered, washed twice with HCl (5 wt%, 400 mL) to remove residual metal ions, and rinsed three times with deionized water. The resultant GO was dried at 60 °C in an oven prior to further use.

2.2. Synthesis of GO-Fe_3O_4 Nanocomposites

The GO-Fe_3O_4 nanocomposites were synthesized through chemical co-precipitation of ferric and ferrous ions in the presence of GO.[17, 25] GO (30 mg) was initially ultrasonicated in deionized water (100 mL) for 2 h to transform the carboxylic acid groups into carboxylate anions. Separately, $FeCl_3 \cdot 6H_2O$ (0.05 mol) and $FeCl_2 \cdot 4H_2O$ (0.025 mol) were dissolved in deionized water (250 mL), and was added slowly into the GO solution at room temperature. The initial pH of the mixture was measure at 1.48. Then, 1 M NaOH was added dropwise (2 mL/min) into the solution until a pH of 10 was obtained under constant stirring conditions. During the addition of NaOH a colour changed was observed: yellow through brown, transitioning to black. The mixture was aged by constant stirring for a further 30 min at pH 10. The resulting black precipitate was magnetically separated and washed three times with deionized water and dried in oven at 60 °C for 48 h. Analogous procedures were repeated by changing the weight ratio of GO to the precipitated Fe_3O_4; from a blank sample, 0 wt%, through 0.5, 1, 5 and 10 wt%, respectively.

2.3. Material Characterization

FTIR measurements were carried out using a PerkinElmer Spectrum 400 FT-IR/ATR Spectrometer, within a range of 4000–500 cm^{-1}. BET specific surface area and pore volume were measured on the basis of N_2 sorption capacity at 77 K on Micromeritics Tristar 3020 after degassing at 90 °C overnight under vacuum to remove any adsorbed components. Phase analysis was performed by X-ray diffraction using a Bruker D8 Advance diffractometer (Cu Kα radiation, $\lambda = 1.5418$ Å; accelerating voltage of 40 kV and current of 40 mA) and morphological investigations were performed on a JEOL 1010 transmission electron microscope (TEM) operated at 100 kV. Samples for TEM were prepared by placing a drop of dilute sample dispersed in ethanol onto a carbon-coated copper grid and dried at room temperature.

2.4. Catalytic Activity Testing

The catalytic activity studies were carried out using Acid Orange 7 (AO7, 35 mg/L) dye as the model organic pollutant in a water matrix. The initial pH of dye solution was adjusted to the desired value using 1 M HCl or 1 M NaOH. Following the pH adjustment, an appropriate dosage of GO-Fe_3O_4 nanocomposite was introduced into an Erlenmeyer flask filled with AO7 solution

(250 mL) and magnetically stirred at 350 rpm to maintain a uniform suspension. After allowing 30 min for the adsorption/desorption of AO7 to reach equilibrium, the reaction was initiated by adding predetermined amounts of H_2O_2 solution to the flask which subsequently time logged. Samples were withdrawn periodically during the reaction and analyzed immediately after removing suspended particles via 0.2 μm Millipore syringe filters. Dye concentrations were analyzed with a UV-Vis spectrophotometer (Evolution 220, Thermo Fisher Scientific) at a maximum absorbance wavelength of 484 nm.

3. RESULTS AND DISCUSSION

3.1. Synthesis and Properties of GO-Fe_3O_4 Nanocomposites

The synthesis process of GO-Fe_3O_4 nanocomposites is schematically illustrated in Figure 1. It is well known that the surfaces of exfoliated GO sheets are covered by a large number of carboxyl, hydroxyl and epoxy groups on its graphitic backbone due to oxidation processes. These functional groups can act as anchor sites that enable the subsequent *in situ* deposition of Fe_3O_4 nanoparticles onto the GO sheets.[26]

The proposed formation mechanism of GO-Fe_3O_4 nanocomposites during the co-precipitation reaction can be elucidated by Figures 1(3) and (4) as follows:
(i) when the iron solutions are mixed with the exfoliated GO suspension, Fe^{3+}/Fe^{2+} ions are adsorbed and coordinated by the carboxyl groups of GO sheets;[27]
(ii) subsequently, the Fe^{3+}/Fe^{2+} ions are hydrolysed to form $Fe(OH)_3/Fe(OH)_2$ nanoclusters on GO sheets when NaOH is introduced into the mixture; and
(iii) condensation of $Fe(OH)_3$/ $Fe(OH)_2$ nanoclusters lead to the formation of Fe_3O_4 nuclei.[28]

Further nucleation and growth of Fe_3O_4 crystallites on GO sheets were due to the redox reaction as the pH is increased to 10.[29] The following reaction equation is proposed for the fabrication of GO-Fe_3O_4 nanocomposites:

$$2Fe^{3+} + Fe^{2+} + GO + 8OH^- \leftrightarrow GO + 2Fe(OH)_3 \rightarrow GO \cdot Fe_3O_4(s) + 4H_2O \quad (1)$$

The functionalization of GO with Fe_3O_4 nanoparticles was confirmed by FTIR spectroscopy. The presence of oxygenated-functionalized groups in the GO spectrum (Fig. 2) is in good agreement with previous work.[26, 30] The broad peak between 3200–3400 cm^{-1} is assigned to the stretching of O—H band. The peak at 1714 cm^{-1} is associated with the stretching band of C═O in carbonyl moieties, including carboxylic acid. Meanwhile, the peaks observed at 1622, 1361, 1224 and 1051 cm^{-1} correspond to skeletal vibrations of graphitic domains (aromatic C═C), carboxyl C—O, epoxy C—O and alkoxy C—O stretching vibrations, respectively.

The spectrum of GO-Fe_3O_4 nanocomposites differs from that of GO as evidenced by the weakening of the hydroxyl region between 3400 and 3200 cm^{-1}. This result indicates that the O—H bond was reduced after depositing Fe_3O_4 nanoparticles, which are chemically anchored on GO surfaces with the aid of carboxylic acid. This deposition can be substantiated by the shift of the C═O peak (carboxylic acid) on GO from 1714 cm^{-1} to 1550 cm^{-1} due to the formation of carboxylate ion ($–COO^-$).[25] Enhanced intensity of $–COO^-$ peak can be observed with an increasing GO loading from 0.5 wt% to 10 wt%. The broad peak between 600 and 550 cm^{-1} corresponds to the vibration of M_T–O–M_O for Fe_3O_4; where M_T and M_O denote the metal occupying tetrahedral and octahedral positions, respectively.[31] This Fe–O vibration

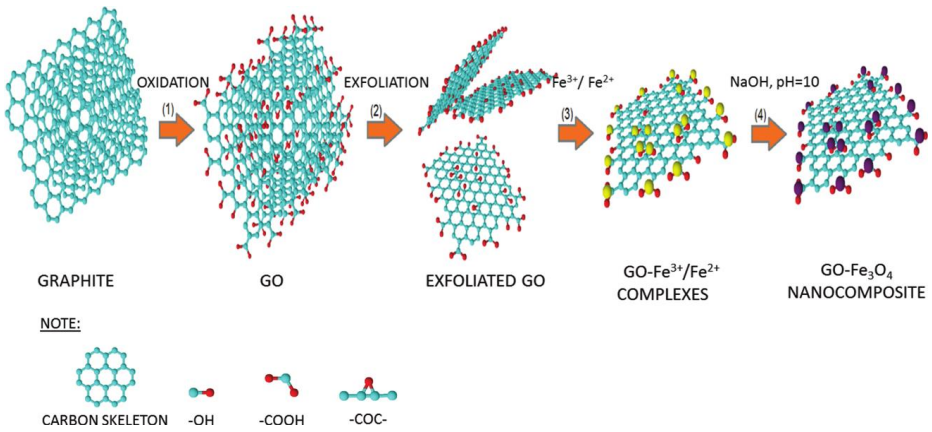

Fig. 1. Illustration of GO-Fe_3O_4 nanocomposites synthesis: (1) Oxidation of graphite to GO by modified Hummers method. (2) Exfoliation of GO sheets by ultrasonication. (3) Adsorption and coordination of Fe^{3+}/Fe^{2+} ions onto the GO sheets. (4) Nucleation and growth of Fe_3O_4 crystallites to form GO-Fe_3O_4 nanocomposites.

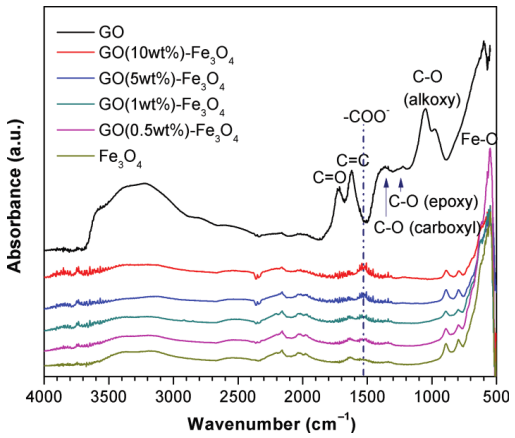

Fig. 2. FTIR spectrum of GO, Fe_3O_4 nanoparticles and GO-Fe_3O_4 nanocomposites.

peak weakens further as the nanocomposite GO loading is increased, suggesting that the Fe_3O_4 nanoparticles are bound onto the GO surface.

N_2 adsorption isotherms were performed to determine the pore structure of the Fe_3O_4 nanoparticles and GO-Fe_3O_4 nanocomposites as shown in Figure 3. The nanocomposites exhibited Type IV isotherms with hysteresis loops. The extended loop indicates that a wide range of mesopores are present in the nanocomposites. The mesoporous structure of Fe_3O_4 can be probably attributed to the interspaces of aggregated Fe_3O_4 nanoparticles due to their strong magnetic interactions.[18] This claim was further supported by the *t*-plot that confirmed the Fe_3O_4 nanoparticles were dense, as depicted in the Figure 3 inset.

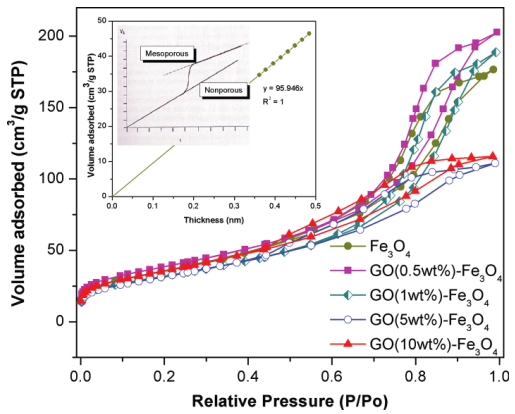

Fig. 3. N_2 adsorption/desorption isotherms of GO-Fe_3O_4 nanocomposites with different GO loading weight ratios; insets show the calculated *t*-plot of Fe_3O_4 nanoparticles and literature. Reprinted with permission from [32], P. A. Webb, et al., Analytical Methods in Fine Particle Technology, Micromeretics Instrument Corporation, Norcross, GA, USA (**1997**). © 1997, Micromeritics.

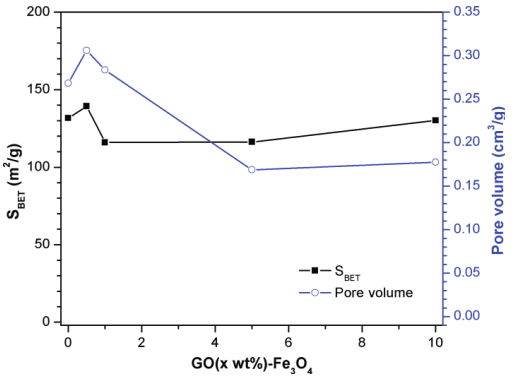

Fig. 4. BET surface area and pore volume of GO-Fe_3O_4 nanocomposites at different GO loading weight ratios.

These findings can be well supported through the correlations between the BET surface area and pore volume of nanocomposites as presented in Figure 4. It was found that by increasing GO loading from 0.5 to 10 wt%, the BET surface areas were consistently within the range of 115–130 m^2/g. In fact, the addition of GO has not significantly altered the N_2 isotherms (Fig. 3) up to partial pressures of 0.3, especially with the blank sample which does not contain GO. As the corresponding calculations of BET surface area are modeled from these partial pressures, these results suggest that the GO contributed very little to the total surface area of the GO-Fe_3O_4 nanocomposites. In fact, the BET surface area of GO is low in the range of 30–40 m^2/g due to the strong hydrogen bonding that causes tight sheet associations.[33,34]

However, GO delivered pronounced changes in the pore volumes of the GO-Fe_3O_4 nanocomposites. While Figure 4 shows that the addition of 0.5 and 1.0 wt% GO led to small variations of 0.31 to 0.28 cm^3/g, greater GO loadings of 5 and 10 wt% resulted in a significant 42% decrease in pore volume to 0.18 cm^3/g. These results may be associated with various pore structures resulting from different building blocks between the Fe_3O_4 nanoparticles and GO as reported elsewhere.[18] To further explain the observed structural changes, the hysteresis loops of the 0.5 and 1.0 wt% GO loaded samples has a similar shape to the blank sample containing Fe_3O_4 only (Fig. 3). Further GO loadings of 5 and 10 wt% lead to flattening of the hysteresis shape, indicating a significant loss in pore volume.

The discussion on surface areas and pore volumes suggest that there are two regimes associated with structural formation of GO-Fe_3O_4 nanocomposites. The first regime is linked to small GO loadings, where the GO loading plays a marginal role in the final structure. In this case, the anchoring of Fe_3O_4 on GO may form single flat structures similar to Figure 1.4 which are dispersed in the GO-Fe_3O_4 nanocomposites. The second regime is directly related to higher GO loadings. The reduction in pore volume

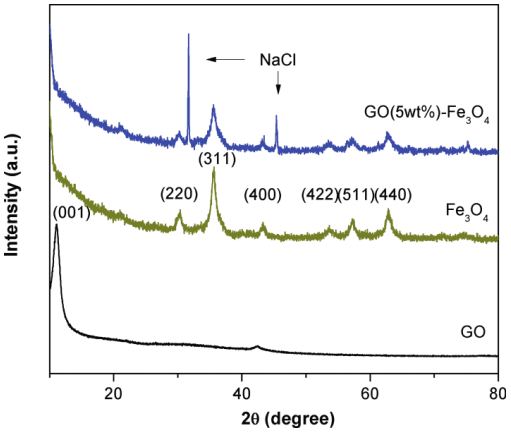

Fig. 5. XRD patterns of GO, Fe_3O_4 nanoparticles and GO (5 wt%)-Fe_3O_4 nanocomposite.

and hysteresis loop suggests that the single flat structures combine, sandwiching the Fe_3O_4 nanoparticles between the GO sheets, possibly leading to stacked GO-Fe_3O_4 nanocomposite structures. Therefore these results suggest that the higher Fe_3O_4 content (low GO loading) was effective in causing the intercalation of nanoparticles within the GO sheets and allowing the formation of a narrow hysteresis. In the case of reduced Fe_3O_4 content (high GO loading), there was an increased aggregation of the GO sheets leading to a reduction in pore volume. In addition, the hysteresis loop suggests that the pore size distribution became broader, possibly attributed to disordering stacking of GO sheets (see XRD patterns in Fig. 5) or the agglomeration of the Fe_3O_4 nanoparticles which intercalated between the GO sheets.

The crystalline structure of synthesized GO, Fe_3O_4 and GO (5 wt%)-Fe_3O_4 nanocomposite were confirmed by XRD measurements (Fig. 5). The characteristic GO reflection at 11.1° 2θ-corresponds to the (001) planes, which indicates a typical loose layer-like structure due to the existence of oxygenated-functional groups on both sides of the sheets with water molecules trapped between the sheets.[19] The crystal structure of Fe_3O_4 nanoparticles was confirmed by the presence of diffraction peaks at 30.3, 35.4, 43.3, 53.6, 57.2 and 62.9° 2θ which can be assigned to the (220), (311), (400), (422), (511) and (440) crystal planes of face-centred cubic Fe_3O_4 (indexed to JCPDS No. 19-0629). All the peaks in the XRD patterns of Fe_3O_4 nanoparticles are in the good agreement with those reported in the literature.[21,29] Similar XRD patterns were also noted on GO (5 wt%)-Fe_3O_4 nanocomposite, which further confirmed the successful deposition of Fe_3O_4 nanoparticles onto the GO sheets. The diffraction peaks at 31.6 and 45.3° 2θ were due to sodium chloride, a residual impurity from the synthesis procedure. Moreover, the disappearance of (001) planes in the GO was possibly attributed to disruption of the typical layer-like structure of GO. In fact, it is suggested that disordered stacking of GO sheets in the GO (5 wt%)-Fe_3O_4 nanocomposite were formed due to the growth of Fe_3O_4 crystallites. The NaCl peaks observed in Figure 5 are attributed to the GO-Fe_3O_4 nanocomposites synthesis method which involves the reaction of NaOH and iron chloride salts ($FeCl_3 \cdot 6H_2O$/$FeCl_2 \cdot 4H_2O$). Although the as-prepared samples were thoroughly washed

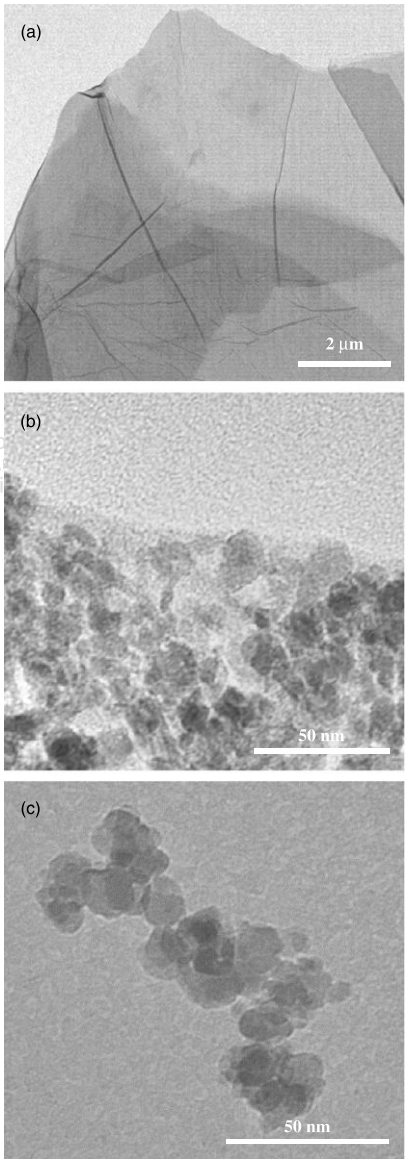

Fig. 6. TEM images of (a) GO, (b) GO (5 wt%)-Fe_3O_4 nanocomposite and (c) Fe_3O_4 nanoparticles.

in deionised water several times, persistent traces of NaCl remained trapped in the sample matrix.

The structure and morphology of GO, Fe_3O_4 nanoparticles and the GO (5 wt%)-Fe_3O_4 nanocomposite were further characterized with TEM. The synthesized GO (Fig. 6(a)) presents the lamellar 2D structure with smooth surfaces and wrinkled edges as a result of deformation upon the exfoliation and restacking process, in agreement with the literature.[20, 35, 36] After grafting with Fe_3O_4 nanoparticles to form a GO-Fe_3O_4 nanocomposite (Fig. 6(b)), the GO had a much rougher surface that indicates that the Fe_3O_4 nanoparticles have been deposited on the surface of GO layers. The size of these Fe_3O_4 nanoparticles was within 6–15 nm as depicted in Figure 6(c). In fact, no individual Fe_3O_4 nanoparticles were spotted beyond the GO sheets of the nanocomposite even after ultrasonication. This was attributed to strong chemical interactions between the carboxylate ions and iron oxide.[25] It is also worth mentioning that the Fe_3O_4 nanoparticles were directly grafted onto the GO surfaces without having any molecular linkers.

3.2. Catalytic Activity

The catalytic activity of the nanocomposites towards the activation of H_2O_2 in degrading AO7 dye is depicted in Figure 7(a). In order to demostrate their synergy-induced enhancement in the catalytic activity, control experiments were performed using Fe_3O_4 nanoparticles and GO sheets by observing the decolorization of AO7, respectively. Negligible degradation of the AO7 solution was observed in the blank conditions of Fenton-like reaction. This behavior might be attributed to the low oxidation potential of H_2O_2 compared to OH radicals. In the presence of the Fe_3O_4 nanoparticles and GO sheets, AO7 was degraded by 48 and 22% at 180 min, respectively. Meanwhile, the degradation rate of AO7 in the presence of GO-Fe_3O_4 nanocomposites varied within the range of 46–76% after 180 min of reaction at different GO loading weight ratios.

The GO (5 wt%)-Fe_3O_4 nanocomposite was found to exhibit prominent degradation of AO7 with 76% observed within 90 min, which suggests that the catalytic properties of the nanocomposite was enhanced by the well dispersed Fe_3O_4 nanoparticles anchored to the GO sheets and the combined effect between them. Ramirez et al.[9] and Noorjahan et al.[14] revealed that the difference in the oxidation rate was contributed to the synergistic effect, a result of the adsorption properties of the substrate,[23] whereby the adsorbed pollutant molecules in the immediate vicinity of immobilized Fe ions ($\equiv Fe^{2+}/\equiv Fe^{3+}$) were rapidly degraded by the generated $^{\bullet}OH$ radicals.[11, 37]

The degradation of AO7 by H_2O_2 catalyzed with GO (5 wt%)-Fe_3O_4 nanocomposite can be well supported by the change in the UV-Vis absorption spectrum over the course of degradation (Fig. 7(b)). The AO7 spectrum was characterized by the chromophore that contained azo linkage in the visible range at 484 and 430 nm corresponding

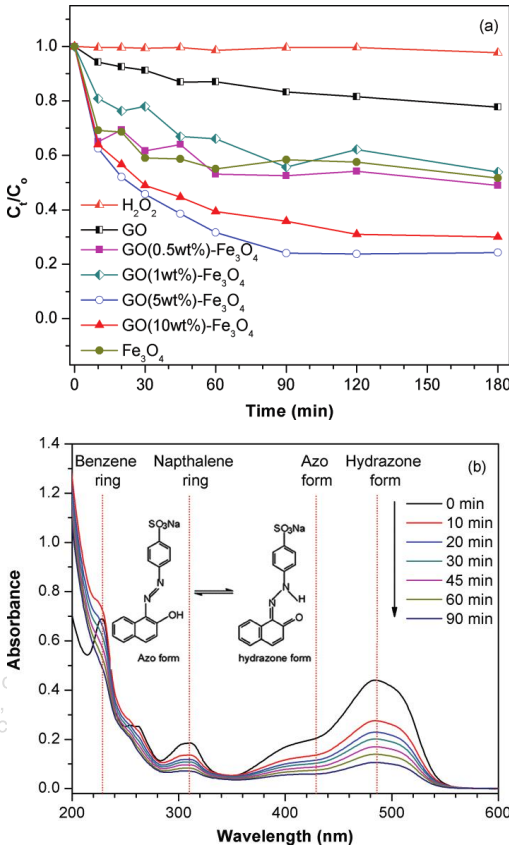

Fig. 7. (a) Degradation of AO7 by GO-Fe_3O_4 nanocomposites in heterogeneous Fenton-like reactions and (b) Spectral changes of AO7 by GO (5 wt%)-Fe_3O_4 nanocomposite ($C_{catalyst} = 0.5$ g/L; $C_{AO7o} = 35$ mg/L; $C_{H_2O_2o} = 8.64$ mM; $pH_o = 3$; $T = 25$ °C).

to the hydrazone and azo form. Meanwhile the other two bands at 230 and 310 nm in ultraviolet region were ascribed to the adjacent auxochrome of benzene and naphthalene rings, respectively.[38] These four characteristic bands were markedly weakened with increasing reaction time, tending to disappear after 90 min, without the appearance of new adsorption bands in the visible or ultraviolet regions due to the destruction of the chromophoric and auxochromic structures by the heterogeneous Fenton-like reactions.

4. CONCLUSIONS

Graphene oxide (GO) was successfully employed as the catalytic support for anchoring Fe_3O_4 nanoparticles in the heterogeneous Fenton-like reactions. The GO (5 wt%)-Fe_3O_4 nanocomposite showed enhanced degradation of AO7 over the control catalyst, i.e., Fe_3O_4 nanoparticles

and GO sheets, respectively. Such catalytic behaviour is attributed to the expected synergistic effect of GO on the pre-concentration of AO7 to be oxidized within the vicinity of reactive centres ($\equiv Fe^{2+}/\equiv Fe^{3+}$). Hence, this novel approach of combining GO flat sheets and Fe_3O_4 nanoparticles show promising direction for further explorations in utilizing GO-Fe_3O_4 nanocomposites for the removal of dyes.

Acknowledgments: The authors acknowledge funding support by Australia Research Council (DP110103533) and The University of Queensland (NSRSF605709). The authors also acknowledge the facilities, and the scientific and technical assistance, of the Australian Microscopy and Microanalysis Research Facility at the Centre for Microscopy and Microanalysis, The University of Queensland. Nor Aida Zubir gratefully acknowledges the generous financial support from Ministry of Higher Education Malaysia (MOHE) and Universiti Teknologi MARA (UiTM) for her Ph.D. study leave. Xiwang Zhang specially thanks for the Australia Research Fellowship provided by Australia Research Council.

References and Notes

1. S. H. S. Chan, T. W. Yeong, J. C. Juan, and C. Y. Teh, *J. Chem. Technol. Biotechnol.* 86, 1130 (**2011**).
2. V. M. Correia, T. Stephenson, and S. J. Judd, *Environ. Technol.* 15, 917 (**1994**).
3. M. Aleksić, H. Kušić, N. Koprivanac, D. Leszczynska, and A. L. Božić, *Desalination* 257, 22 (**2010**).
4. E. Forgacs, T. Cserháti, and G. Oros, *Environ. Int.* 30, 953 (**2004**).
5. F. P. Van der Zee, and S. Villaverde, *Water Res.* 39, 1425 (**2005**).
6. R. Fang, X. Cheng, and X. Xu, *Bioresour. Technol.* 101, 7323 (**2010**).
7. A. N. Soon and B. H. Hameed, *Desalination* 269, 1 (**2011**).
8. S. Karthikeyan, A. Titus, A. Gnanamani, A. B. Mandal, and G. Sekaran, *Desalination* 281, 438 (**2011**).
9. J. H. Ramirez, F. J. Maldonado-Hódar, A. F. Pérez-Cadenas, C. Moreno-Castilla, C. A. Costa, and L. M. Madeira, *Appl. Catal. B: Environ.* 75, 312 (**2007**).
10. N. T. Dung, P. N. Hoa, D. M. Huy, and N. K. Tham, *J. Hazard. Mater.* 185, 653 (**2011**).
11. H. Hassan and B. H. Hameed, *Chem. Eng. J.* 171, 912 (**2011**).
12. C. L. Hsueh, Y. H. Huang, and C. Y. Chen, *J. Hazard. Mater.* 129, 228 (**2006**).
13. Z. Yaping and H. Jiangyong, *Appl. Catal. B: Environ.* 78, 250 (**2008**).
14. M. Noorjahan, V. Durga Kumari, M. Subrahmanyam, and L. Panda, *Appl. Catal. B: Environ.* 57, 291 (**2005**).
15. O. Taran, E. Polyanskaya, O. Ogorodnikova, V. Kuznetsov, V. Parmon, M. Besson, and C. Descorme, *Appl. Catal. A: Gen.* 387, 55 (**2010**).
16. Z. Xiong, L. L. Zhang, and X. S. Zhao, *Chem.-Eur. J.* 17, 2428 (**2011**).
17. S. K. Behera, *Chem. Commun.* 47, 10371 (**2011**).
18. J. Su, M. Cao, L. Ren, and C. Hu, *J. Phys. Chem. C* 115, 14469 (**2011**).
19. F. Wang and K. Zhang, *J. Mol. Catal. A: Chem.* 345, 101 (**2011**).
20. G. Xie, P. Xi, H. Liu, F. Chen, L. Huang, Y. Shi, F. Hou, Z. Zeng, C. Shao, and J. Wang, *J. Mater. Chem.* 22, 1033 (**2012**).
21. M. Liu, C. Chen, J. Hu, X. Wu, and X. Wang, *J. Phys. Chem. C* 115, 25234 (**2011**).
22. G. Liao, S. Chen, X. Quan, H. Yu, and H. Zhao, *J. Mater. Chem.* 22, 2721 (**2012**).
23. W. Lu, R. Ning, X. Qin, Y. Zhang, G. Chang, S. Liu, Y. Luo, and X. Sun, *J. Hazard. Mater.* 197, 320 (**2011**).
24. W. S. Hummers and R. E. Offeman, *J. Am. Chem. Soc.* 80, 1339 (**1958**).
25. X. Yang, X. Zhang, Y. Ma, Y. Huang, Y. Wang, and Y. Chen, *J. Mater. Chem.* 19, 2710 (**2009**).
26. M. Z. Kassaee, E. Motamedi, and M. Majdi, *Chem. Eng. J.* 172, 540 (**2011**).
27. J. W. Zhu, G. Y. Zeng, F. D. Nie, X. M. Xu, S. Chen, Q. F. Han, and X. Wang, *Nanoscale* 2, 988 (**2010**).
28. Z. Li, B. Tan, M. Allix, A. I. Cooper, and M. J. Rosseinsky, *Small* 4, 231 (**2008**).
29. H. Wu, G. Gao, X. Zhou, Y. Zhang, and S. Guo, *CrystEngComm* 14, 499 (**2012**).
30. J. Shen, M. Shi, H. Ma, B. Yan, N. Li, and M. Ye, *Mater. Res. Bull.* 46, 2077 (**2011**).
31. O. Karaagac, H. Kockar, S. Beyaz, and T. Tanrisever, *IEEE Trans. Magn.* 46, 3978 (**2010**).
32. P. A. Webb, C. Orr, R. W. Camp, J. P. Oliver, and Y. S. Yunes, Analytical Methods in Fine Particle Technology, Micromeretics Instrument Corporation, Norcross, GA, USA (**1997**).
33. T. N. Lambert, C. A. Chavez, B. Hernandez-Sanchez, P. Lu, N. S. Bell, A. Ambrosini, T. Friedman, T. J. Boyle, D. R. Wheeler, and D. L. Huber, *J. Phys. Chem. C* 113, 19812 (**2009**).
34. P. Bradder, S. K. Ling, S. Wang, and S. Liu, *J. Chem. Eng. Data* 56, 138 (**2011**).
35. Á. Mastalir, Z. Király, Á. Patzkó, I. Dékány, and P. L'Argentiere, *Carbon* 46, 1631 (**2008**).
36. L. Fan, C. Luo, M. Sun, X. Li, F. Lu, and H. Qiu, *Bioresour. Technol.* 114, 703 (**2012**).
37. X. Hu, B. Liu, Y. Deng, H. Chen, S. Luo, C. Sun, P. Yang, and S. Yang, *Appl. Catal. B: Environ.* 107, 274 (**2011**).
38. G. Li, K. H. Wong, X. Zhang, C. Hu, J. C. Yu, R. C. Y. Chan, and P. K. Wong, *Chemosphere* 76, 1185 (**2009**).

Chapter 4

Structural and functional investigations of GO–Fe_3O_4 nanocomposites

4.1 Introduction

The aim of chapter 4 was to investigate the synergistic structural and functional effects of GO–Fe_3O_4 nanocomposites. The formation of different sets of structure and functionalities is hypothesised to affect their resultant catalytic performances. Changes in these relationships were strongly influenced by the amount of GO loading as well as its dispersion effect during the synthesis of GO–Fe_3O_4 nanocomposites. Hence, this chapter demonstrates the correlation between structure, morphology and functionality of GO–Fe_3O_4 nanocomposites at various GO loadings on the overall catalytic performances for the oxidative degradation of AO7 in the heterogeneous Fenton-like reaction.

4.2 Contributions

This chapter studied the influence of GO loading on the structural-morphological and functionalities relationships of GO–Fe_3O_4 nanocomposites in correlation with their catalytic performances for the oxidative degradation of AO7. The major contribution of this work was the formation of two distinct GO–Fe_3O_4 nanocomposite structures with different catalytic activities. This work also demonstrates that the presence of strong interfacial interactions between the Fe_3O_4 NPs and GO contributed to the superior degradation of AO7.

SCIENTIFIC REPORTS

OPEN

SUBJECT AREAS:
CHEMICAL ENGINEERING
NANOPARTICLES

Received
14 January 2014

Accepted
19 March 2014

Published
4 April 2014

Correspondence and requests for materials should be addressed to J.C.D.d.C. (j.dacosta@uq.edu.au)

Structural and functional investigation of graphene oxide–Fe_3O_4 nanocomposites for the heterogeneous Fenton-like reaction

Nor Aida Zubir[1,2], Christelle Yacou[1], Julius Motuzas[1], Xiwang Zhang[3] & João C. Diniz da Costa[1]

[1]The University of Queensland, FIMLab—Films and Inorganic Membrane Laboratory, School of Chemical Engineering, Brisbane, Qld 4072, Australia, [2]Universiti Teknologi MARA (UiTM), Faculty of Chemical Engineering, 13500 Pulau Pinang, Malaysia, [3]Department of Chemical Engineering, Monash University, Clayton, VIC 3800, Australia.

Graphene oxide–iron oxide (GO–Fe_3O_4) nanocomposites were synthesised by co-precipitating iron salts onto GO sheets in basic solution. The results showed that formation of two distinct structures was dependent upon the GO loading. The first structure corresponds to a low GO loading up to 10 wt%, associated with the beneficial intercalation of GO within Fe_3O_4 nanoparticles and resulting in higher surface area up to 409 $m^2 g^{-1}$. High GO loading beyond 10 wt% led to the aggregation of Fe_3O_4 nanoparticles and the undesirable stacking of GO sheets. The presence of strong interfacial interactions (Fe-O-C bonds) between both components at low GO loading lead to 20% higher degradation of Acid Orange 7 than the Fe_3O_4 nanoparticles in heterogeneous Fenton-like reaction. This behaviour was attributed to synergistic structural and functional effect of the combined GO and Fe_3O_4 nanoparticles.

Magnetite (Fe_3O_4) has attracted considerable research interests in materials chemistry because of its unique properties, including decent magnetic, electric, catalytic, biocompatibility and low toxicity properties[1–4]. In particular, Fe_3O_4 nanoparticles (NPs) have been reported to be a catalyst in many reactions such as Fischer-Tropsch[5], Haber-Bosch[6,7], environmental catalysis[3,8,9], and peroxidase-like activities[10–12]. However, these NPs are prone to aggregate and form large particles owing to strong anisotropic dipolar interactions specifically in aqueous phase, thus losing their dispersibility and specific properties which eventually diminish their activity[13]. Therefore, there is a need to immobilise these NPs onto supports to preserve their unique properties[14–16].

Among many materials, graphene and its derivatives are considered potential materials for the immobilisation of NPs. Of particular interest, graphene oxide (GO) is an attractive material due to its unique two-dimensional lamellar structure and high surface area as well as full surface accessibility and edge reactivity[1,17]. The immobilised NPs are not only able to prevent the aggregation of graphene or GO from stacking but also improve the overall catalytic activity owing to the strong synergistic interaction between both components[18,19]. The lack of surface functionalities in graphene to directly immobilise the NPs onto its surfaces has led to favourable utilisation of GO as an alternative support for the assembly of graphene based nanocomposites[20].

GO is derived from the exfoliation of graphite oxide and consists of abundant oxygenated functional groups, such as hydroxyl and epoxides on the basal plane with carbonyl and carboxyl groups at the edges. These oxygenated functional groups can serve as nucleation sites for metal ions to form NPs/GO nanocomposites. Recently, several studies have been reported using GO for the support of Fe_3O_4 NPs in catalysis for the reduction of nitrobenzene[21], the oxidation of cysteine[22] and 3,3,5,5-tetramethylbenzidine[23]. The reported enhancement in catalytic activity was attributed to the synergistic effects between both GO sheets and Fe_3O_4 NPs.

This work primarily focuses on developing nanocomposite structures containing graphene oxide and iron oxide (GO–Fe_3O_4). The resultant GO–Fe_3O_4 nanocomposites were synthesised via depositing Fe_3O_4 NPs on GO sheets by co-precipitation method. The nanocomposites were then extensively characterised using nitrogen sorption, transmission electron microscopy (TEM) and X-ray photoelectron spectroscopy (XPS), to better understand their structures and functionalities. Finally, the catalytic activity of the nanocomposites in the degradation of Acid Orange 7 (AO7) dye was evaluated in a heterogeneous Fenton-like reaction. The results provide a new insight into

the development of GO–Fe_3O_4 nanocomposites and the structural-morphology relationships with their catalytic activity.

Results

The nitrogen sorption measurements were performed to investigate the textural characteristics of resultant nanocomposites at different GO loading, varying from 0 to 25 wt%. The nitrogen isotherms in Fig. 1a resulted in type IV shape with H2 hysteresis loop in the range of 0.3–0.98 relative pressure. These results suggest that the GO–Fe_3O_4 nanocomposites are characterised by mesoporous structures. The pore size distribution curves (Fig. 1b) calculated using DFT model display pore sizes in the range from 1 to 10 nm. In contrast to the GO–Fe_3O_4 nanocomposites, Fe_3O_4 NPs show a much broader pore size distribution up to 20 nm. Such vicissitudes in hysteresis and pore size distribution may be ascribed to the role played by GO in tailoring the pore structure of the nanocomposites. This stems from integrating two-dimensional (GO sheets) and zero-dimensional (Fe_3O_4 NPs) structures into a single material[24].

The specific surface area and pore volumes of the prepared Fe_3O_4 NPs and nanocomposites are presented in Fig. 1c. A noteworthy increment in surface area was observed by increasing GO loading from 5 to 10 wt% (max S_{BET} approximately 409 $m^2\ g^{-1}$), which declined thereafter. Indeed, a similar observation was also found in pore volume. At low GO loading (≤10 wt%), the pore volume remained steady at ~0.32–0.33 $cm^3\ g^{-1}$ and subsequently decreased to ~0.23–0.24 $cm^3\ g^{-1}$ at higher GO loading (>10 wt%).

Figs. 2a–b show the micrographs of pure GO sheets where the surface dimensions are of several microns and thickness of ~30 nm. Fe_3O_4 NPs are agglomerated (Figs. 2c–d), evidenced by formation of large clusters. Figs. 2e–f and 2g–h show the micrographs of the 5 and 15 wt% GO nanocomposites, respectively. Compared to the pristine GO sheets (Fig. 2a–b), it can be distinctly seen that Fe_3O_4 NPs were deposited onto GO surfaces of the nanocomposites. Moreover, no isolated Fe_3O_4 NPs were observed beyond the GO, suggesting a strong interaction between the NPs and GO sheets. It is also observed a significant reduction in the thickness of the layers for the 5 wt% GO loading, calculated from 2 to 3 nm around Fe_3O_4 NPs, or up to ~5 nm as a combination of these layers (see broken line box at the inset of Fig. 2f). For the 15 wt% GO loading, the Fe_3O_4 NPs agglomerated on the external GO surface, and GO layer thickness could not be measured.

Although a minor degree of aggregation occurs at low GO loading (5 wt%), most of the Fe_3O_4 NPs are still highly dispersed on the GO sheets (Fig. 2e). It is further observed the NPs were intercalated between the GO sheets (see the inset broken line box in Fig. 2f). This observation suggests that the low GO loading helped to prevent Fe_3O_4 from severe aggregation, which is beneficial for the distribution of NPs over the GO planes. The bright circular rings in the selected area electron diffraction (SAED) patterns indicate that Fe_3O_4 NPs are polycrystalline. The spaced-resolved lattice fringes with an interplanar distance of 0.25 nm agree well with the lattice spacing of (311) planes of Fe_3O_4 as reported elsewhere[20,25].

However, a higher GO loading (15 wt%) shows the formation of a different structure. This is clearly seen in the HRTEM micrograph (Fig. 2h) where the surface no longer displays the GO sheets as in Figs. 2a and 2e–f. In fact, Fig. 2h exhibits patterns similar to the pure Fe_3O_4 NPs in Fig. 2d. These images are evidencing that a higher

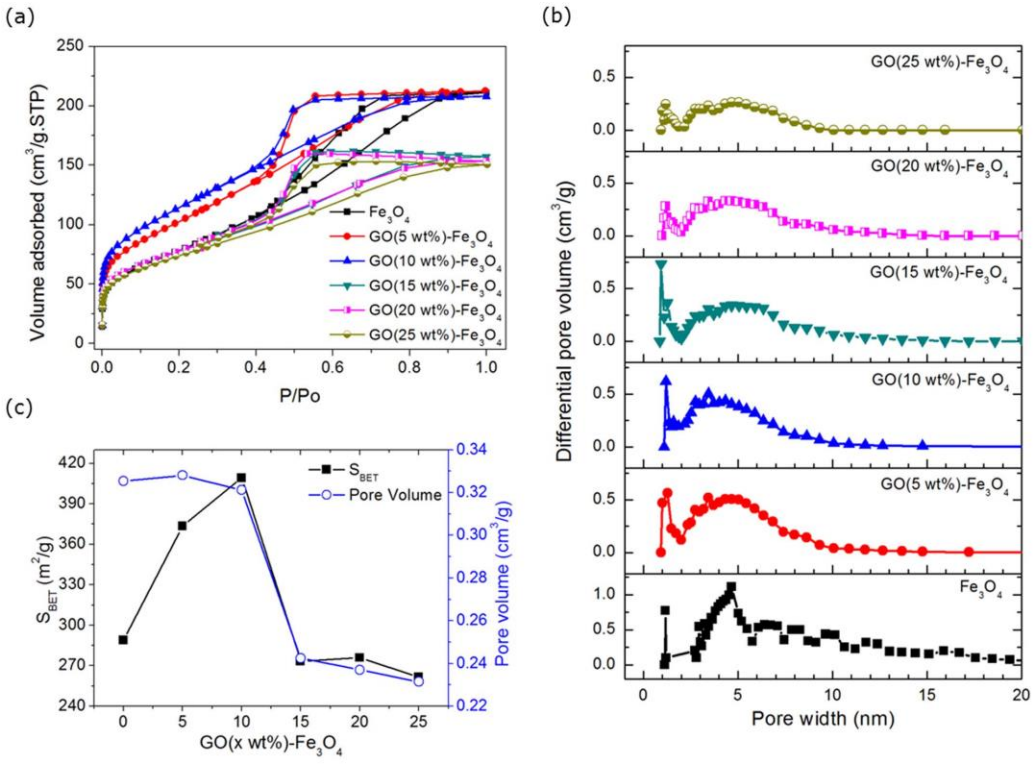

Figure 1 | (a) Nitrogen adsorption-desorption isotherms, (b) DFT pore size distributions and (c) S_{BET} and pore volume of Fe_3O_4 and GO–Fe_3O_4 nanocomposites at various GO loadings.

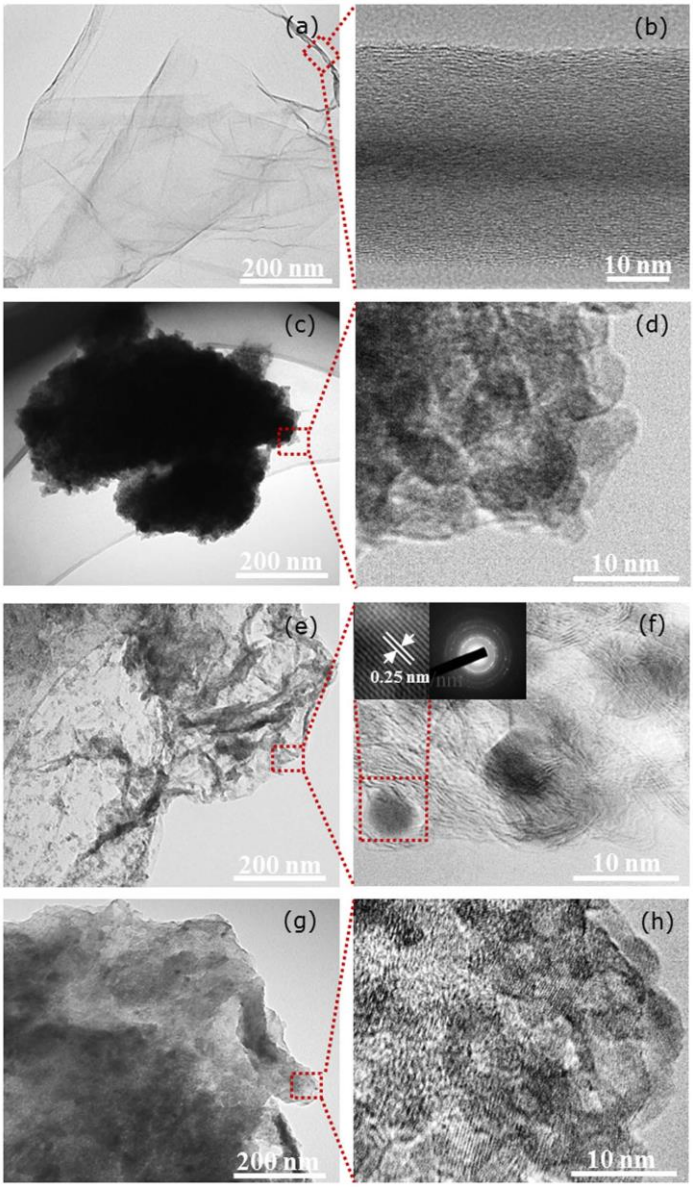

Figure 2 | **TEM images of (a–b) GO, (c–d) Fe_3O_4 NPs, (e–f) GO(5 wt%)–Fe_3O_4 nanocomposite and (g–h) GO(15 wt%)–Fe_3O_4 nanocomposite.**

degree of aggregation of Fe_3O_4 NPs prevails once the GO loading reached 15 wt%, which is coherent with the reduction in pore volume (Fig. 1c). The dominant coverage of Fe_3O_4 NPs is attributed to the oxygenated functional groups on the exterior surface of GO stacking, which tend to facilitate the nucleation and growth of the NPs. This process is similar to many cases where the surface defects and edges provide thermodynamically favourable nucleation sites[26], which show heavy agglomeration as seen in Figs. 2c–d.

The prepared nanocomposites were then further analysed using XPS to verify the phase of NPs, interaction between NPs and GO and state of GO as supports. As seen in Fig. 3a, the wide scan spectra of the nanocomposites exhibited photoelectron lines at binding energies of ~285, 530 and 711 eV which are ascribed to C 1s, O 1s and Fe 2p, respectively. The binding energy peaks at 711.1 and 724.6 eV in the high resolution Fe 2p scan (Fig. 3b) correspond to Fe $2p_{3/2}$ and Fe $2p_{1/2}$, respectively. The disappearance of the charge transfer satellite of Fe $2p_{3/2}$ at ~720 eV reveals the formation of mixed oxide of Fe(II) and Fe(III) namely as Fe_3O_4[1,27]. Besides, similar peak patterns were attained with different GO loadings, indicating the formation of Fe_3O_4 phase in all nanocomposites.

Fig. 4a shows the O 1s spectra of GO, GO–Fe_3O_4 nanocomposites and Fe_3O_4 NPs. The deconvolution of the O 1s spectrum of GO

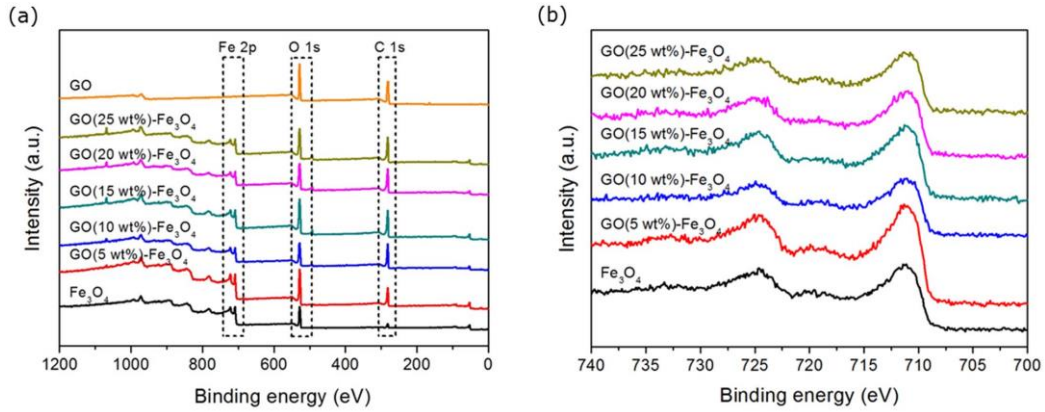

Figure 3 | **(a) Wide scan XPS spectra and (b) high resolution Fe 2p spectra of GO, GO–Fe_3O_4 nanocomposites and Fe_3O_4 NPs.**

consists of three peaks: (i) the oxygen that binds to the sulphate group owing to slight trace of sulphur detected at 168 eV in wide scan spectra (O ex SO_4: 531.4 eV), (ii) the oxygen in carboxylate and/or carbonyl (O–C = O; C = O: 532.4 eV), and (iii) the oxygen in the epoxy and/or hydroxyl (C–O–C; C–OH: 533.2 eV). It is notable that the peaks of O 1s in GO–Fe_3O_4 nanocomposites spectra shifted to lower binding energy and broadened, which is characteristic of the O 1s belonging to lattice oxygen in Fe_3O_4 (Fe–O: 529.8 eV)[26].

The binding of Fe_3O_4 on GO might possibly occur through either the carbon atoms or with the oxygenated functional groups on both GO surfaces and edges. However, the first possibility is excluded as the contribution from C or Fe atoms in the Fe–C bonds are not present at 707.5[28] and 283.3 eV[29] in both Fe 2p (Fig. 3b) and C 1s (Fig. 4b) spectra of the nanocomposites, respectively. Therefore, we postulate that the emergence of the new peak at about 531.2 eV in the nanocomposites spectra is assigned to the deposition of Fe_3O_4 NP onto GO sheets, which is possibly via Fe–O–C bonds. Such postulation can be supported by the significant decrease in the relative intensity of O–C = O, C = O and C–O–C, and C–OH peaks in the nanocomposites compared to the pristine GO, which suggests possible bidentate coordination of the Fe element with carboxylate groups[23,30] and replacement of hydrogen in hydroxyl groups. Further considerations could be related to a ring opening reaction of epoxy groups[31,32] by Fe element in Fe_3O_4 through the Fe–O–C bonds. The O 1s spectrum of Fe_3O_4 NPs displays a maximum peak centred at 529.8 eV which is ascribed to the Fe–O bonds. This finding can be substantiated by the fact that the formation of metal–O–C bonds in nanocomposites could be shifted to higher binding energy approximately 1–3 eV from the metal–O bonds of metal oxides[28,32–34] as presented in Table 1.

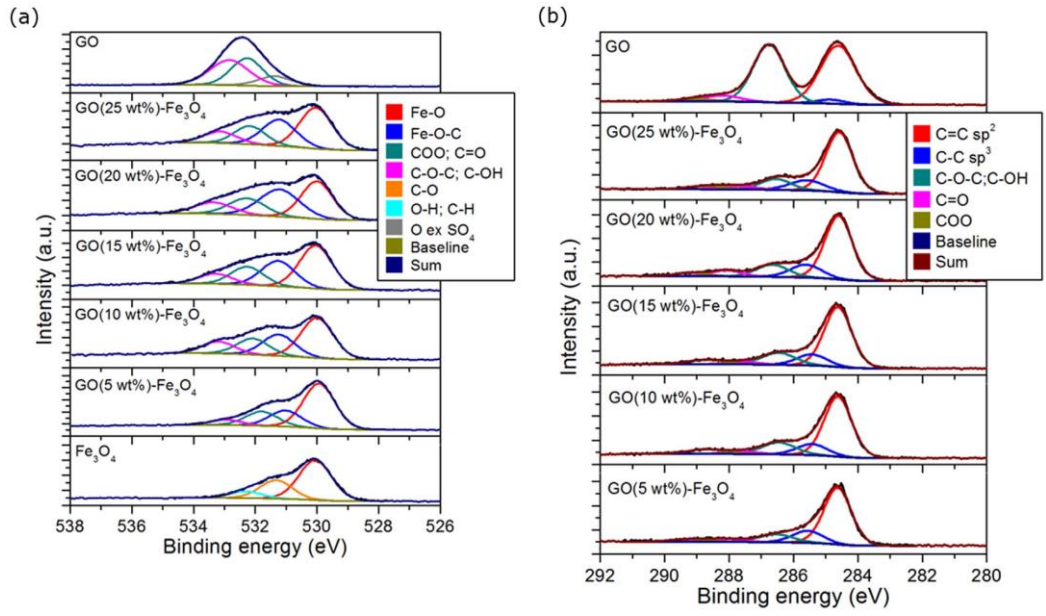

Figure 4 | **XPS curve fit of (a) O 1s and (b) C 1s spectra.**

Table 1 | Binding energy (B.E.) of metal–O–C bonds in O 1s spectra

Metal–O bond	B.E. (eV)	Metal–O–C bond	B.E. (eV)	Refs.
Fe–O	530.3	Fe–O–C	531.7	28
		Fe–O–C	533.0	33
Fe–O	529.8	Fe–O–C	531.2	This work
Ni–O	529.3	Ni–O–C	530.2	32
Cu–O	530.5	Cu–O–C	532.8	34

The state of GO as a support in these nanocomposites is further demonstrated by the C 1s spectra as shown in Fig. 4b. The spectrum of GO can be deconvoluted into five components corresponding to C = C sp^2 (284.6 eV), C–C sp^3 (285.1 eV), C–OH and/or C–O–C (286.7 eV), C = O (288.1 eV) and O–C = O (289.0 eV)[17,35,36]. It is observed that the intensity of C–OH and C–O–C peak is alike with the C = C sp^2, suggesting that GO is adequately oxidised and holds lots of hydroxyl and epoxy groups as compared to the carbonyl and carboxylate groups. Interestingly, the peak of C–C sp^3 in GO–Fe_3O_4 nanocomposites shifted to higher binding energy by 0.4 eV. This peak increased in its intensity together with C = C sp^2 upon the deposition of Fe_3O_4, while the oxygenated functional groups decreased, particularly for C–OH and C–O–C as the GO loading reduces. These results suggest the likelihood of GO to undergo partial reduction due to partial removal of epoxide and hydroxyl group on GO basal plane, which were deoxygenated under alkaline conditions during the preparation of GO–Fe_3O_4 nanocomposites.

Additionally, the formation of a new covalent bond, Fe–O–C, and the partial reduction in GO as supports for these nanocomposites were reaffirmed based on the atomic concentration and its respective ratio of deconvoluted peaks from O 1 s and C 1 s spectra (Fig. 4). The summarised data deduced from the respective peaks are presented in Fig. 5. The emergence of Fe–O–C bond was found to increase gradually in low GO loading (<10 wt%) and tends to level off once reaching 10 wt%. As the GO loading increases, the amount of Fe_3O_4 deposited raises progressively with the readily available oxygenated functional groups within the exfoliated GO sheets by the successful intercalation between both components. However, further increasing the GO loading (beyond 10 wt%) leads to the saturation of Fe–O–C bonding close to 25%, that possibly infers to a change in structure. The C = O/Fe–O ratio from the O 1 s spectra were found to increase gradually as a function of the GO loading, which signifies

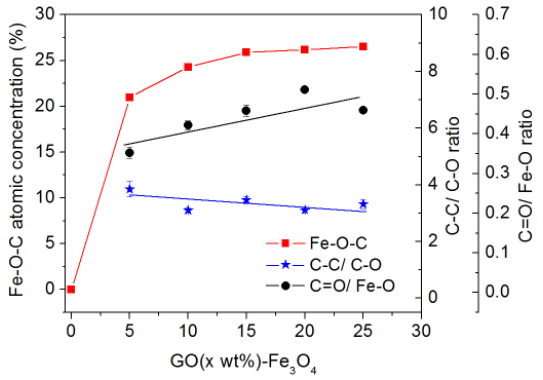

Figure 5 | Correlations between the Fe–O–C atomic content, C–C/C–O and C = O/Fe–O atomic ratio with increased in GO loading of GO–Fe_3O_4 nanocomposites.

higher GO's reduction can be obtained at lower loading compared to the higher one. Intriguingly, this finding can be verified by the ratio of atomic concentration for the carbon domain over the oxygenated functional groups (C–C/C–O) of GO in the C 1 s spectra of nanocomposites. The ratio of C–C/C–O declines steadily from 4 to nearly 3 with increasing GO loading, compared to the pristine GO value of 1. This correlation further corroborate with the state of GO as a support which undergoes partial reduction during co-precipitation through the gradual removal of oxygenated functional groups from its surfaces and edges.

The catalysis of GO–Fe_3O_4 nanocomposites and each individual component for the degradation of AO7 as the model organic pollutant was investigated in the heterogeneous Fenton-like reaction as shown in Fig. 6. The low GO loading (≤10 wt%) nanocomposites led to higher AO7 degradation within 92–98% of removal compared with lower values for pristine Fe_3O_4 NPs and GO. However, the removal efficiency of AO7 at higher GO loading (>10 wt%) declined gradually from 88 to 60% possibly attributed to the structural makeup of the nanocomposite.

Discussion

As the operation of heterogeneous Fenton-like reaction involved in concurrent adsorption and reactions at the solid-liquid interface, the surface accessibility of the GO–Fe_3O_4 nanocomposites is crucial in maintaining their catalytic activity. High accessibility of reactants towards the active sites ($\equiv Fe^{2+}/\equiv Fe^{3+}$) at low GO loading can be achieved by the increase of surface area and pore volume (Fig. 1c), which are able to diminish limitations in mass transfer during the reaction. This can be correlated with their unique structures as schematically represented in Fig. 7. The proposed structures are relying on the degree of GO loading, wherein the low (below 10 wt%) and high (above 10 wt%) GO loading form Structures I and II, respectively. The formation of these unique structures is attributed to the GO dispersion effect and similar behaviour has been reported for GO and nanowires[37], or GO and polystyrene[38].

Structure I schematically represents the intercalation of NPs between the GO sheets, as seen in the HRTEM micrograph in Fig. 2f. In this case, the hydroxylated iron complexes are able to homogeneously anchor onto both the surfaces and edges of exfoliated GO sheets through the oxygenated functional groups, i.e. hydroxyl, epoxy and carboxyl. Further condensation of complexes leads to the formation of nuclei and growth of Fe_3O_4 crystallites onto GO sheets as a result of redox reaction. Likewise, this correlates well with the observed variation in the desorption branch of isotherms between relative pressures of 0.55–0.4 of the nanocomposites as compared to 0.75–0.4 of the Fe_3O_4 NPs as displayed in Fig. 1a. This effect may be associated with the resultant pore structure from the combination of different building blocks between the GO sheets and Fe_3O_4 NPs. This finding can be further corroborated with the featured pore width of ≤10 nm for the nanocomposites that was not observed in pure Fe_3O_4 NPs as presented in Fig. 1b.

Meanwhile, Structure II is correlated with deposition of Fe_3O_4 NPs mainly onto the exterior surface of GO stacking at higher GO loading. The anticipated GO stacking may be ascribed to the reduction in the degree of exfoliation as the concentration of GO increases. High GO loading may induce a dominant effect of GO stacking through the π-π interactions which correspond to the van der Waals and hydrophobic fields around the carbon basal plane of GO sheets. In fact, this proposed structures are in well agreement with the surface area and pore volume profiles which showed nearly 30% reduction in both once the GO loading increased to 15 wt% or more (Fig. 1c). Therefore, at higher GO loading, the aggregation of Fe_3O_4 NPs on the exterior surface of GO stacking might hinder the effective diffusion and contact between the reactants towards the active sites, which went against the ample formation of hydroxyl radicals to decompose AO7 during the reaction.

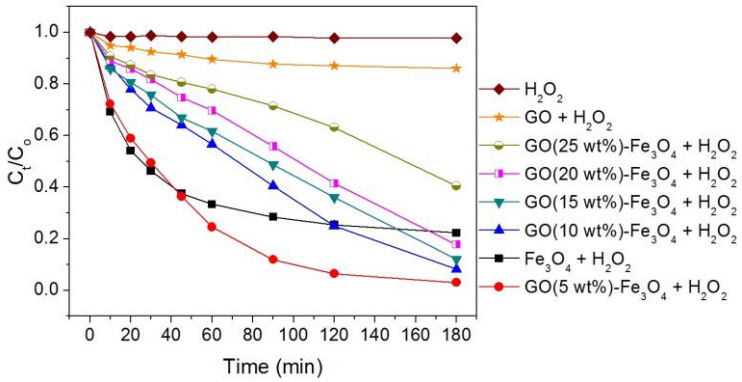

Figure 6 | Degradation profile of AO7 on GO, GO–Fe_3O_4 nanocomposites and Fe_3O_4 NPs samples in heterogeneous Fenton-like reaction. Experimental conditions: AO7 0.1 mM, H_2O_2 22 mM, catalyst 0.2 g L^{-1}, T = 25°C and pH 3.

Interestingly, the highest BET surface area of the nanocomposites was recorded at GO loading of 10 wt%, though the highest catalytic activity was found to be at GO loading of 5 wt% with the overall rate constant (k) of 0.02 min^{-1}. This indicates that the structure of the nanocomposites is not the only factor affecting their catalytic activity. With increasing GO loading, the catalytic activity of the nanocomposites gradually decreased, which means that there is a strong correlation between the catalytic activity and C–C/C–O ratio (Fig. 5). The higher reduction degree of GO at low GO loading promotes the transfer of electrons between Fe_3O_4 and GO through Fe-O-C bonds, which is beneficial for the degradation of AO7. The nanocomposite of 5 wt% GO loading delivered similar catalytic activity with the bare Fe_3O_4 NPs during the first 45 minutes of reaction as shown in Fig. 6, though the latter completely deactivated thereafter. Contrary to this detrimental result, the nanocomposite retained good stability by sustaining its activity throughout the entire reaction.

The degradation of AO7 occurs mainly at the solid-liquid interfaces of nanocomposites, where the formation of hydroxyl radicals ($HO^{\bullet}$) is due to the catalysed decomposition of hydrogen peroxide (H_2O_2) by the active sites ($\equiv Fe^{2+}/\equiv Fe^{3+}$) of Fe_3O_4 NPs. The symbol $\equiv$ represents the iron species bound to the surface of GO sheets. In addition, GO consists of unpaired π electrons by the presence of many semiconducting π-conjugated carbon sp^2 domain on its basal planes[39] which in turn are able to facilitate electron transfer between GO and iron centres[40]. This synergistic effect is beneficial in the regeneration of ferrous irons to speed up the redox cycle between the active sites, thus promoting the degradation and mineralisation of AO7.

The enhancement in chemical reactivity can be attributed to the synergistic effects between both optimized GO loading and Fe_3O_4 NPs. These effects may be explained by a combination of few factors. First, the high surface areas of exfoliated GO promotes good dispersion of Fe_3O_4 NPs onto GO sheets (Structure I). This was found to be beneficial in enhancing the mass transfer of reactants towards the active sites ($\equiv Fe^{2+}/\equiv Fe^{3+}$) during the reaction. Secondly, GO features a large aromatic ring structure on its basal plane that favours AO7 adsorption which has a similar aromatic ring structure through π-π interactions. This may provide an increase in AO7's local concentration[41] within the vicinity of the active sites to be further oxidised by the generated hydroxyl radicals[42]. Thirdly, the strong Fe_3O_4 NPs-GO interactions via Fe–O–C bonds facilitates the electron transfer between the NPs and the semiconducting GO sheets[40]. Lastly, the regeneration of ferrous ions was facilitated during the reaction possibly owing to the partial reduction in GO that helps electron transport to speed up the redox cycle between the active sites ($\equiv Fe^{2+}/\equiv Fe^{3+}$). This is evident for the low GO 5 wt% nanocomposite (see Fig. 5) as the C-C/C-O ratio is the highest thus demonstrating a higher removal of the oxygenated functional groups compared with the other nanocomposites at higher GO loading. In summary, this work demonstrates the structural and morphological relationship of GO–Fe_3O_4 nanocomposites at varies GO loadings on the overall catalytic activity of AO7 degradation in the heterogeneous Fenton-like oxidation.

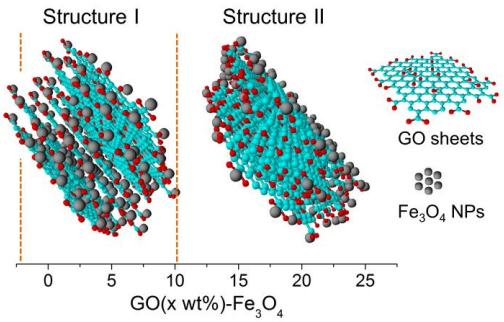

Figure 7 | The proposed two different structures of the GO–Fe_3O_4 nanocomposites at transitional GO loading of 10 wt% (the cyan, red and grey ball and stick model correspond to the carbon skeleton of GO sheet, oxygenated functional groups and Fe_3O_4 NPs, respectively).

Methods

Materials and preparation of GO–Fe_3O_4 nanocomposites. Graphite flakes, $FeCl_3 \cdot 6H_2O$ (97%), $FeCl_2 \cdot 4H_2O$ (99%) and AO7 (Orange II; 85%) were purchased from Sigma-Aldrich. All other reagents and solvents employed for synthesis were of analytical grade and used as received. Graphite oxide was synthesised via a modified Hummers method[43,44] and subsequently exfoliated by ultrasonication to attain an aqueous dispersion of GO. The GO–Fe_3O_4 nanocomposites were synthesised by co-precipitating pre-hydrolysed ferric and ferrous salts in the presence of GO. Briefly, an aqueous solution (100 mL) containing $FeCl_3 \cdot 6H_2O$ (4 mmol) and $FeCl_2 \cdot 4H_2O$ (2 mmol) was prepared with an initial pH of 1.48. However, GO sheets are prone to stack together at such low pH solutions, thus diminishing the effective surface of GO[45]. To address this problem, GO was not added into the mixture until the pH was adjusted to pH 4 via addition of NaOH (1 M). Subsequently, the GO solution (50 mL, 0.55 mg/mL) was gradually added into the pH 4 solution and stirred for another 30 min giving rise to a stable and homogeneous mixture. An appropriate amount of NaOH (1 M) was continuously added into this mixture to reach a pH of 10. The mixture was aged at constant stirring for a further 30 min at room temperature. The resulting black precipitate was magnetically separated and washed three times with deionized water and ethanol prior drying in an oven at 60°C for 48 h. The GO loadings for GO–Fe_3O_4 were set at 5, 10, 15, 20 and 25 wt%, respectively. Pure Fe_3O_4

NPs were also prepared via an analogous method without the addition of GO solution, for comparison purpose only.

Characterisation. Brunauer-Emmett-Teller (BET) specific surface area and pore volume were measured by nitrogen sorption using a Micromeritics Tristar 3020. The pore size distribution for each sample was calculated using non-local density functional theory (NLDFT), from the desorption branch of the isotherms. Microstructural investigation was carried out using a transmission electron microscopy (TEM, JOEL 1010) operated at 100 kV, and high-resolution transmission electron microscopy (HRTEM, JOEL 2010) with an acceleration voltage of 200 kV. Micrographic grids were prepared by placing a drop of diluted sample dispersion in ethanol onto a carbon-coated copper grid and dried at room temperature. X-ray photoelectron spectroscopy (XPS) was performed on Kratos Axis ULTRA X-ray photoelectron spectrometer equipped with monochromatic Al Kα ($h\nu = 1486.6$ eV) radiation to quantitatively analysed the chemical composition of samples. To determine the chemical functionality of the samples, the O 1 s and C 1 s spectra were curve fitted by combining the components and minimizing the total square-error fit of less than 2%. The curve fitting was performed using a Gaussian–Lorentzian peak shape and Shirley background function. The C 1 s photoelectron binding energy was set at 284.6 eV and used as reference for calibrating others peak positions.

Catalytic experiment. In order to investigate the catalytic activity of the as prepared GO–Fe_3O_4 nanocomposites, degradation of AO7 was studied in a heterogeneous Fenton-like reaction. All experiments were performed using GO–Fe_3O_4 (0.2 g L^{-1}) in AO7 (0.1 mM) aqueous solution of 250 mL at 25°C and pH 3. Prior to the batch runs, the initial pH of AO7 solution was adjusted with NaOH (1 M) or HCl (1 M) to 3. The reactions were initiated by adding H_2O_2 (22 mM) into the suspension and stirred at 350 rpm after 30 min of dark adsorption. Samples were periodically withdrawn, filtered through 0.2 μm Milipore syringe filters and immediately analysed. The AO7 degradation as a function of the time was analysed by measuring the absorbance of the solution at λ_{max} 484 nm using an UV-Vis spectrophotometer (Evolution 220, Thermo Fisher Sci.).

1. He, H. & Gao, C. Supraparamagnetic, conductive, and processable multifunctional graphene nanosheets coated with high-density Fe_3O_4 nanoparticles. *ACS Appl. Mater. Interfaces* **2**, 3201–3210 (2010).
2. Wei, Y. *et al.* Synthesis and cellular compatibility of biomineralized Fe_3O_4 nanoparticles in tumor cells targeting peptides. *Colloids Surf. B* **107**, 180–188 (2013).
3. Xu, L. & Wang, J. Fenton-like degradation of 2,4-dichlorophenol using Fe_3O_4 magnetic nanoparticles. *Appl. Catal. B* **123–124**, 117–126 (2012).
4. Thanikaivelan, P., Narayanan, N. T., Pradhan, B. K. & Ajayan, P. M. Collagen based magnetic nanocomposites for oil removal applications. *Sci. Rep.* **2**, 230; DOI:10.1038/srep00230 (2012).
5. Moodley, P., Scheijen, F. J. E., Niemantsverdriet, J. W. & Thüne, P. C. Iron oxide nanoparticles on flat oxidic surfaces—Introducing a new model catalyst for Fischer–Tropsch catalysis. *Catal. Today* **154**, 142–148 (2010).
6. Huazhang, L., Caibo, L., Xiaonian, L. & Yaqing, C. Effect of an iron oxide precursor on the H_2 desorption performance for an ammonia synthesis catalyst. *Ind. Eng. Chem. Res.* **42**, 1347–1349 (2003).
7. Bogdanov, S. S., Aleksić, B. D., Mitov, I. G., Klisurski, D. G. & Petranović, N. A. Comparative study of the reduction kinetics of magnetites and derived ammonia synthesis catalysts. *Thermochim. Acta* **173**, 71–79 (1990).
8. Zhang, S. *et al.* Superparamagnetic Fe_3O_4 nanoparticles as catalysts for the catalytic oxidation of phenolic and aniline compounds. *J. Hazard. Mater.* **167**, 560–566 (2009).
9. Zhu, M. & Diao, G. Synthesis of Porous Fe_3O_4 nanospheres and its ppplication for the catalytic degradation of xylenol orange. *J. Phys. Chem. C* **115**, 18923–18934 (2011).
10. Gao, L. *et al.* Intrinsic peroxidase-like activity of ferromagnetic nanoparticles. *Nat. Nanotechnol.* **2**, 577–583 (2007).
11. Gao, Y. *et al.* Fluorometric method for the determination of hydrogen peroxide and glucose with Fe_3O_4 as catalyst. *Talanta* **85**, 1075–1080 (2011).
12. Wei, H. & Wang, E. Fe_3O_4 magnetic nanoparticles as peroxidase mimetics and their ppplications in H_2O_2 and glucose detection. *Anal. Chem.* **80**, 2250–2254 (2008).
13. Deng, J., Wen, X. & Wang, Q. Solvothermal in situ synthesis of Fe_3O_4-multi-walled carbon nanotubes with enhanced heterogeneous Fenton-like activity. *Mater. Res. Bull.* **47**, 3369–3376 (2012).
14. Thi Dung, N., Ngoc Hoa, P., Manh Huy, D. & Kim Tham, N. Magnetic Fe_2MO_4 (M:Fe, Mn) activated carbons: Fabrication, characterization and heterogeneous Fenton oxidation of methyl orange. *J. Hazard. Mater.* **185**, 653–661 (2011).
15. Song, S., Rao, R., Yang, H., Liu, H. & Zhang, A. Facile synthesis of Fe_3O_4/MWCNTs by spontaneous redox and their catalytic performance. *Nanotechnol.* **21**, 185602–185607 (2010).
16. Prakash, A., Chandra, S. & Bahadur, D. Structural, magnetic, and textural properties of iron oxide-reduced graphene oxide hybrids and their use for the electrochemical detection of chromium. *Carbon* **50**, 4209–4219 (2012).
17. Fan, W. *et al.* Hybridization of graphene sheets and carbon-coated Fe_3O_4 nanoparticles as a synergistic adsorbent of organic dyes. *J. Mater. Chem.* **22**, 25108–25115 (2012).
18. Zeng, T., Zhang, X.-l., Ma, Y.-r., Niu, H.-y. & Cai, Y.-q. A novel Fe_3O_4-graphene-Au multifunctional nanocomposite: green synthesis and catalytic application. *J. Mater. Chem.* **22**, 18658–18663 (2012).
19. Choi, Y. *et al.* Hybrid gold nanoparticle-reduced graphene oxide nanosheets as active catalysts for highly efficient reduction of nitroarenes. *J. Mater. Chem.* **21**, 15431–15436 (2011).
20. Wu, H., Gao, G., Zhou, X., Zhang, Y. & Guo, S. Control on the formation of Fe_3O_4 nanoparticles on chemically reduced graphene oxide surfaces. *CrystEngComm* **14**, 499–504 (2012).
21. He, G. *et al.* Fe_3O_4@graphene oxide composite: A magnetically separable and efficient catalyst for the reduction of nitroarenes. *Mater. Res. Bull.* **48**, 1885–1890 (2013).
22. Song, Y., He, Z., Hou, H., Wang, X. & Wang, L. Architecture of Fe_3O_4–graphene oxide nanocomposite and its application as a platform for amino acid biosensing. *Electrochim. Acta* **71**, 58–65 (2012).
23. Dong, Y.-l. *et al.* Graphene oxide-Fe_3O_4 magnetic nanocomposites with peroxidase-like activity for colorimetric detection of glucose. *Nanoscale* **4**, 3969–3976 (2012).
24. Su, J., Cao, M., Ren, L. & Hu, C. Fe_3O_4–graphene nanocomposites with improved lithium storage and magnetism properties. *J. Phys. Chem. C* **115**, 14469–14477 (2011).
25. Zhou, G. *et al.* Graphene-wrapped Fe_3O_4 anode material with improved reversible capacity and cyclic stability for lithium ion batteries. *Chem. Mater.* **22**, 5306–5313 (2010).
26. Geng, Z. G. *et al.* Highly efficient dye adsorption and removal: a functional hybrid of reduced graphene oxide-Fe_3O_4 nanoparticles as an easily regenerative adsorbent. *J. Mater. Chem.* **22**, 3527–3535 (2012).
27. Chandra, V. *et al.* Water-dispersible magnetite-reduced graphene oxide composites for arsenic removal. *ACS Nano* **4**, 3979–3986 (2010).
28. Zhou, J., Song, H., Ma, L. & Chen, X. Magnetite/graphene nanosheet composites: interfacial interaction and its impact on the durable high-rate performance in lithium-ion batteries. *RSC Adv.* **1**, 782–791 (2011).
29. Adenier, A. *et al.* Covalent modification of iron surfaces by electrochemical reduction of aryldiazonium salts. *J. Am. Chem. Soc.* **123**, 4541–4549 (2001).
30. Shen, J. *et al.* One step synthesis of graphene oxide—magnetic nanoparticle composite. *J. Phys. Chem. C* **114**, 1498–1503 (2010).
31. Pei, S., Zhao, J., Du, J., Ren, W. & Cheng, H.-M. Direct reduction of graphene oxide films into highly conductive and flexible graphene films by hydrohalic acids. *Carbon* **48**, 4466–4474 (2010).
32. Zhou, G. *et al.* Oxygen bridges between NiO nanosheets and graphene for improvement of lithium storage. *ACS Nano* **6**, 3214–3223 (2012).
33. Combellas, C., Delamar, M., Kanoufi, F., Pinson, J. & Podvorica, F. I. Spontaneous grafting of iron surfaces by reduction of aryldiazonium salts in acidic or neutral aqueous solution. Application to the protection of iron against corrosion. *Chem. Mater.* **17**, 3968–3975 (2005).
34. Hurley, B. L. & McCreery, R. L. Covalent bonding of organic molecules to Cu and Al alloy 2024 T3 surfaces via diazonium ion reduction. *J. Electrochem. Soc.* **151**, B252–B259 (2004).
35. Fan, Z.-J. *et al.* Facile synthesis of graphene nanosheets via Fe reduction of exfoliated graphite oxide. *ACS Nano* **5**, 191–198 (2011).
36. Chen, W., Li, S., Chen, C. & Yan, L. Self-assembly and embedding of nanoparticles by in situ reduced graphene for preparation of a 3D graphene/nanoparticle aerogel. *Adv. Mater.* **23**, 5679–5683 (2011).
37. Li, Y. G. & Wu, Y. Y. Coassembly of graphene oxide and nanowires for large-area nanowire alignment. *J. Am. Chem. Soc.* **131**, 5851–5857 (2009).
38. Stankovich, S. *et al.* Graphene-based composite materials. *Nature* **442**, 282–286 (2006).
39. Matsumoto, Y. *et al.* Photoreaction of graphene oxide nanosheets in water. *J. Phys. Chem. C* **115**, 19280–19286 (2011).
40. Jasuja, K., Linn, J., Melton, S. & Berry, V. Microwave-reduced uncapped metal nanoparticles on graphene: Tuning catalytic, electrical, and raman properties. *J. Phys. Chem. Lett.* **1**, 1853–1860 (2010).
41. Qu, J.-C. *et al.* Facile synthesis of multifunctional graphene oxide/AgNPs-Fe_3O_4 nanocomposite: A highly integrated catalysts. *Chem. Eng. J.* **211–212**, 412–420 (2012).
42. Hu, X. *et al.* Adsorption and heterogeneous Fenton degradation of 17α-methyltestosterone on nano Fe_3O_4/MWCNTs in aqueous solution. *Appl. Catal. B* **107**, 274–283 (2011).
43. Hummers, W. S. & Offeman, R. E. Preparation of graphitic oxide. *J. Am. Chem. Soc.* **80**, 1339–1339 (1958).
44. Xiong, Z., Zhang, L. L. & Zhao, X. S. Visible-light-induced dye degradation over copper-modified reduced graphene oxide. *Chem. Eur. J.* **17**, 2428–2434 (2011).
45. Zubir, N. A., Zhang, X., Yacou, C. & Diniz da Costa, J. C. Fenton-like degradation of acid orange 7 using graphene oxide-iron oxide nanocomposite. *Sci. Adv. Mater.* **6**, 1–7 (2014).

Acknowledgments

The authors acknowledge funding support from The University of Queensland (NSRSF605709). The authors also acknowledge the facilities, and the scientific and technical assistance, of the Australian Microscopy & Microanalysis Research Facility at the

Centre for Microscopy and Microanalysis, The University of Queensland. Nor Aida Zubir gratefully acknowledges the generous financial support from Ministry of Higher Education Malaysia (MOHE) and Universiti Teknologi MARA (UiTM) for her PhD study leave. J.C. Diniz da Costa acknowledges support given by Australia Research Council Future Fellowship program (FT130100405).

Author contributions

N.A.Z. performed the experimental works, analysed results and wrote the manuscript. J.M. executed the HRTEM analysis. X.Z., C.Y. and J.C.D.d.C. advised N.A.Z. and reviewed the manuscript prior to submission.

Additional information

Competing financial interests: The authors declare no competing financial interests.

How to cite this article: Zubir, N.A., Yacou, C., Motuzas, J., Zhang, X.W. & Diniz da Costa, J.C. Structural and functional investigation of graphene oxide–Fe_3O_4 nanocomposites for the heterogeneous Fenton-like reaction. *Sci. Rep.* **4**, 4594; DOI:10.1038/srep04594 (2014).

Chapter 5

Optimisation of heterogeneous Fenton-like reaction using GO–Fe_3O_4 nanocomposites

5.1 Introduction

There is limited understanding on the catalytic reaction effect of GO–Fe_3O_4 nanocomposites in the heterogeneous Fenton-like oxidation of AO7 which warrants further research. Therefore, the aim of chapter 5 was to investigate the most influential operational parameters during the catalysis as it laid a foundation in understanding the impact of these effects towards the GO–Fe_3O_4 catalytic activity. Validation of the optimised conditions was carried out through the one-parameter-at-a-time and the response surface methodology methods. Moreover, this chapter also determines the reaction kinetics and mechanism which governed the oxidative degradation of AO7 using GO–Fe_3O_4 nanocomposites.

5.2 Contributions

This chapter systematically investigates the influence of different operational parameters on the oxidative degradation of AO7 using GO–Fe_3O_4 nanocomposites in the heterogeneous Fenton-like reaction. The major contribution of this work was the determination of optimal operational conditions for the oxidative degradation of AO7. This work also demonstrates the corroboration of reaction kinetics and mechanism in elucidating the rate of intrinsic chemical reaction on the surface of active sites of GO–Fe_3O_4 nanocomposites during the catalysis.

Journal of Environmental Chemical Engineering 2 (2014) 1881–1888

Contents lists available at ScienceDirect

Journal of Environmental Chemical Engineering

journal homepage: www.elsevier.com/locate/jece

Optimisation of graphene oxide–iron oxide nanocomposite in heterogeneous Fenton-like oxidation of Acid Orange 7

Nor Aida Zubir [a,b], Christelle Yacou [a], Xiwang Zhang [c], João C. Diniz da Costa [a,*]

[a] The University of Queensland, FIMLab—Films and Inorganic Membrane Laboratory, School of Chemical Engineering, Brisbane,Queensland 4072, Australia
[b] Universiti Teknologi MARA (UiTM), Faculty of Chemical Engineering, Pulau Pinang 13500, Malaysia
[c] Department of Chemical Engineering, Monash University, Clayton, Victoria 3800, Australia

ARTICLE INFO

Article history:
Received 6 March 2014
Received in revised form 10 June 2014
Accepted 1 August 2014

Keywords:
Graphene oxide
Iron oxide
Nanocomposites
Heterogeneous Fenton-like reaction
Acid Orange 7

ABSTRACT

Well-dispersed iron oxide nanoparticles supported onto graphene oxide sheets (i.e. GO–Fe_3O_4 nanocomposite) were synthesised and used as heterogeneous Fenton-like catalyst for the degradation of Acid Orange 7 dye (AO7). The reaction was systematically investigated under various experimental conditions such as nanocomposite dosage, pH, temperature, oxidant and dye concentrations. Best results showed a fast 80% degradation in ~20 min, whilst ~98% of AO7 was successfully removed after 180 min of reaction time. The degradation kinetics of AO7 was most influenced by pH and temperature, and can be described by a pseudo-first-order reaction following the Langmuir–Hinshelwood mechanism. Analysis of the spent nanocomposite suggested that the phase of iron oxide nanoparticles remained unchanged whilst minor pore volume losses occurred via carbon deposition and/or re-stacking of GO sheets.

Introduction

The disposal of organic pollutants into water resources is an issue of environmental significance, particularly due to the scarcity of potable water facing our contemporary society. One of the industries under strong scrutiny is the textile industry, as previous practices of direct discharge of spent dyes into effluents had led to detrimental effects in both environment and human health due to toxicity, biodegradability and aesthetic impacts [1–3]. Therefore, it is imperative that efficient textile wastewater treatment technologies are put in place to remove these toxic contaminants prior to discharge into natural water bodies. Oxidation using Fenton or Fenton-like reaction has been proven as promising and attractive treatment method for effective decolourisation and degradation of textile dyes. This is attributed to the simplicity of the Fenton reaction operation, together with being an environmentally benign process which produces highly reactive hydroxyl radicals ($HO^{\bullet}$) that oxidise dyes efficiently and non-selectively [4,5]. Nonetheless, the usage of homogeneous Fenton or Fenton-like reaction operation has several significant disadvantages, such as post-treatment requirements prior to discharge as a result of iron hydroxide sludge formation, narrow pH operational range and unattainable regeneration of catalyst which hampers the economic feasibility of this process [6].

To overcome these disadvantages, numerous attempts have been made to develop heterogeneous catalysts including the incorporation of iron ions or iron oxides within the structure of catalyst support [7–10]. The nature and properties of support play a crucial role in the modulation of the activity in catalytic sites [11]. The decomposition of hydrogen peroxide (H_2O_2) in heterogeneous Fenton-like reaction was suggested according to the Eqs. (1) and (2) where ≡ represents the iron species bound to the surface of catalyst support [12]:

$$\equiv Fe^{3+} + H_2O_2 \rightarrow \equiv Fe^{2+} + HOO^{\bullet} + H^{+} \quad (1)$$

$$\equiv Fe^{2+} + H_2O_2 \rightarrow \equiv Fe^{3+} + HO^{\bullet} + OH^{-} \quad (2)$$

Iron catalyst supports, such as carbon based materials (activated carbon; AC) [9,13,14], carbon aerogel [9], ion exchange resin [15], carbon nanotubes (CNTs) [10,16–18], graphene and its derivative graphene oxide (GO) [19,20] have recently been reported. Among these works, carbon nanomaterials (CNTs and GO) were reported to outperform the macroscale carbon systems (AC) in sustaining stable and higher catalytic activity over a number of cycles for H_2O_2 decomposition in aqueous phase [21]. Such improvement is inextricably linked to the morphology, surface functionalities and chemistry of the carbon nanomaterials. Therefore, immobilisation of iron compounds within the structure of these carbon nanomaterials seem to be beneficial in improving

* Corresponding author. Tel.: +61 7 3365 6960; fax: +61 7 3365 4199.
E-mail address: j.dacosta@uq.edu.au (J.C. Diniz da Costa).

http://dx.doi.org/10.1016/j.jece.2014.08.001
2213-3437/

the catalytic activity of heterogeneous Fenton-like reaction. Instead of CNTs, GO is considered to be more economic favourable as catalyst support since it can be conveniently synthesised by the oxidation of graphite which is cheap and naturally abundant.

GO consists of a hexagonal ring-based carbon network with both sp^2 and sp^3 hybridised carbon atoms in two-dimensional structure that contain copious oxygen functional groups such as epoxy, hydroxyl, carbonyl and carboxyl groups on surfaces and edges [22–25]. These oxygen functional groups serve as activation sites for nucleation and growth of iron precursors to form GO supported iron-containing nanocomposites [26,27]. Recently, GO-Fe(III) complexes were used for processing Rhodamine B (RhB) dye resulting in a 38% degradation in 120 min (heterogeneous) and almost 100% within 45 min (photo-assisted) Fenton-like reactions [19]. In a similar fashion, GO–Fe_2O_3 hybrid exhibited 17% higher RhB degradation under the visible-light irradiation over the heterogeneous Fenton-like reactions [20]. These reports have highlighted the efficacy of using GO supported iron-containing nanocomposites in photo Fenton-like rather than heterogeneous reaction.

This work focuses on using GO as a support for magnetite (Fe_3O_4) nanoparticles for the heterogeneous Fenton-like reaction, which simplifies equipment design by dispensing the need of lamp irradiation and extra process controls. The choice of magnetite over the other iron oxide phases is based on its highest Fenton activity [28,29]. Exfoliated GO sheets were used to anchor Fe_3O_4 nanoparticles, thus forming a GO–Fe_3O_4 nanocomposite catalyst [30]. Although GO–Fe_3O_4 nanocomposite [31], where the GO was prepared by the Hummers method [32], were tested for the degradation of Acid Orange 7 (AO7), these works focused mainly on materials development rather than on catalytic reaction. In other words, there is limited understanding of the catalytic reaction effect of GO–Fe_3O_4 nanocomposites on the heterogeneous Fenton-like oxidation of AO7, which warrants further research. Therefore, this work investigates the most influential operational parameters (i.e. dosage, pH, concentration of H_2O_2, concentration of dye and temperature) on the oxidative degradation of AO7 using GO–Fe_3O_4 nanocomposite, supported by a global parametric optimisation. Further, the reaction kinetics is studied and a model is validated following the Langmuir–Hinshelwood mechanism to explain the rate of intrinsic chemical reaction on the surface of active sites on the nanocomposites. Finally, the characterisation of the spent catalyst samples was performed by nitrogen sorption and spectroscopy techniques to verify the stability of the GO–Fe_3O_4 nanocomposite prior to and after the catalytic degradation of AO7 testing.

Experimental

Materials synthesis and characterisation

Graphite flakes, $FeCl_3{\cdot}6H_2O$ (97%), $FeCl_2{\cdot}4H_2O$ (99%), Na_2SO_3 (98%), H_2O_2 (30% w/w) and AO7 (Orange II; 85%) were purchased from Sigma–Aldrich. Other reagents and solvents used were of analytical grade and without further purification. The GO–Fe_3O_4 nanocomposites were synthesised by co-precipitating of pre-hydrolysed ferric and ferrous salts in the presence of GO as described elsewhere [31]. Briefly, GO was first prepared via a modified Hummers method [32,33] and subsequently exfoliated by ultrasonication to attain an aqueous dispersion of GO. Then NaOH (1 M) was added dropwise into 100 mL of precursor solution containing of $FeCl_3{\cdot}6H_2O$ (4 mmol) and $FeCl_2{\cdot}4H_2O$ (2 mmol) until pH 4 under constant stirring. GO solution (50 mL, 0.55 mg mL^{-1}) was then gradually added into a mixture and stirred for another 30 min. NaOH (1 M) was continuously added dropwise into the mixture until reaching pH 10 and then aged for 30 min. The resulting black precipitate was magnetically separated and washed several times with deionised water and ethanol, and dried at 333 K for 48 h.

Microstructural investigation was carried out by transmission electron microscopy (TEM, JOEL 1010) operated at 100 kV. Samples were prepared by placing a drop of diluted sample dispersion in ethanol onto a carbon-coated copper grid and dried at room temperature. The XRD patterns of nanocomposite were obtained using X-ray diffraction by a Bruker D8 Advance diffractometer at 40 kV and 40 mA using filtered Cu Kα radiation (λ = 1.5418 Å). The textural properties of nanocomposite were determined by nitrogen sorption analysis using Tristar II 3020 (Micromeritics).

Oxidation degradation and sorption of AO7

Detailed parametric studies were performed using of GO–Fe_3O_4 nanocomposite in heterogeneous Fenton-like reaction by changing one variable at a time, whilst keeping the others constant. The oxidative degradation of AO7 was determined in the following initial ranges of parameters: (i) nanocomposite dosage (0.1–0.3 g L^{-1}); (ii) pH (2.5–6.3); (iii) concentration of H_2O_2 (2.75–44 mM); (iv) concentration of dye (15–55 mg L^{-1}) and (v) temperature (298–328 K). These testing conditions were chosen based on previous works carried out in the heterogeneous Fenton reaction using iron oxide supported based catalysts [9,12,13]. The reaction was initiated by adding H_2O_2 into the suspension and stirred at 350 rpm after 30 min of dark adsorption. Sampling was carried out periodically. The collected suspension was filtered through 0.2 μm Millipore syringe filters and the filtrates were then immediately analysed. Concentration of AO7 was determined by measuring the absorbance of the solution at 484 nm, corresponding to the maximum absorption wavelength of AO7 in visible region by Evolution 220 UV–vis spectrophotometer (Thermo, Fisher Sci.). The experiments had a reproducible with an average experimental variation of ±7%. The total carbon (TC) analysis was carried out using Shimadzu 5000 TOC-VCSH analyser (Shimadzu), equipped with an automatic sample injector. The TC values represent the average of triplicate measurements.

In order to verify if adsorption was concurrently taking place to the heterogeneous Fenton reaction as reported elsewhere [34,35], adsorption analysis was carried out by mixing an amount of nanocomposite (0.2 g L^{-1}) in a conical flask containing different initial concentration of AO7 ranging from 15 to 55 mg L^{-1} and magnetically stirred at 350 rpm. For equilibrium adsorption studies, the experiments were carried out at pH 3 and 298 K for 24 h to ensure equilibrium was reached. The concentration of AO7 in the supernatant was analysed consecutively. The AO7 uptake at equilibrium, q_e (mg g^{-1}) was calculated according to Eq. (3).

$$q_e = \frac{(C_0 - C_e)V}{W} \quad (3)$$

where C_0 and C_e are the solution concentrations at initial and equilibrium (mg L^{-1}), respectively. V is the volume of solution (L) and W is the mass of the nanocomposite (g).

Results and discussion

Optimisation analysis

GO–Fe_3O_4 nanocomposite containing 5 wt% of GO loading was used in this study due to their optimal catalytic activity [31]. Fig. 1 presents the degradation profile of AO7 at different nanocomposite dosage ranging from 0.1–0.3 g L^{-1}. These results demonstrated that the degradation profile of AO7 increased significantly as a function of the dosage from 0.1 to 0.2 g L^{-1}. Such enhancement in

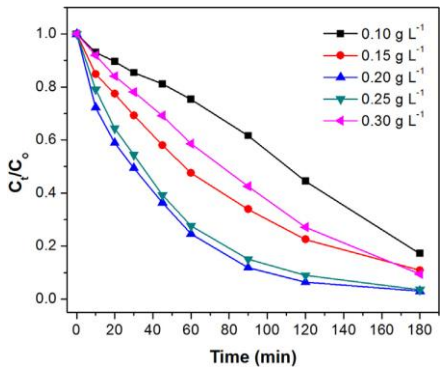

Fig. 1. Effect of GO–Fe_3O_4 nanocomposite dosage on the degradation of AO7. Experimental conditions: AO7 = 35 mg L^{-1}; H_2O_2 = 22 mM; pH = 3 and 298 K.

degradation was ascribed to the increased number of active catalytic sites which are responsible for the decomposition of H_2O_2 into HO• radicals. Nevertheless, further increase of dosage (0.3 g L^{-1}) inhibited the degradation of AO7. This result is attributed to possible scavenging of HO• radicals (Eq. (4)) by the reaction between the excess active sites and the HO• radicals, therefore induced a decline of AO7 degradation [13,36]. Dosages of 0.20 and 0.25 g L^{-1} delivered comparable degradation profile. However, lower nanocomposite dosage is always preferred in catalysis and thus 0.2 g L^{-1} was chosen for all subsequent experiments.

$$\equiv Fe^{2+} + HO^{\bullet} \rightarrow \equiv Fe^{3+} + OH^{-} \quad (4)$$

It is known that pH has a significant impact in heterogeneous Fenton-like reaction, which directly affects the oxidative degradation of dyes by HO• radicals. This is clearly shown in Fig. 2, as the optimal AO7 degradation value of 98% was achieved at pH 3 within 180 min reaction. When the pH was lowered to 2.5, the AO7 degradation decreased to nearly 80%. This result suggests that the protonation of H_2O_2 in forming an oxonium ion ($H_3O_2^+$) had occurred, which then enhances H_2O_2 stability and reduces its reactivity towards $\equiv Fe^{2+}$ (Eq. (5)) [37]. Besides that, the scavenging effect of HO• radicals by the excessive H^+ (Eq. (6)) [11] is also enhanced at pH 2.5. The reduction in AO7 degradation was also observed when the initial pH was higher than 3. This can be explained by decomposition of more H_2O_2 into molecular oxygen and water on the active sites without the formation of appreciable amounts of HO• radicals [38].

$$H_2O_2 + H^+ \rightarrow H_3O_2^+ \quad (5)$$

$$HO^{\bullet} + H^+ + e^- \rightarrow H_2O \quad (6)$$

Oxidant concentration is also regarded as a key operational parameter in producing HO• radicals in oxidative degradation of dye. Fig. 3 depicts the relationship between AO7 degradation at different oxidant (H_2O_2) concentrations. As the H_2O_2 concentration increased from 2.75 to 22 mM, the degradation of AO7 improved from 75% to 98% over 180 min, respectively. These results suggest that more HO• radicals are formed as H_2O_2 concentration increased, which leads to an increased rate in AO7 degradation. However, when the H_2O_2 concentration is over 22 mM, for example 44 mM; the degradation rate slowed down and dropped to 90%. The excess concentration of H_2O_2 may induce parallel undesirable reactions between HO• radicals with H_2O_2 and producing hydroperoxyl radicals (HOO•), as expressed in Eq. (7). The oxidation potential of produced HOO• radicals (1.78 V) is much lower so that they are less reactive to oxidise dyes compared with HO• radicals (2.80 V) [38].

$$H_2O_2 + HO^{\bullet} \rightarrow H_2O + HOO^{\bullet} \quad (7)$$

Fig. 4a illustrates the dependence of AO7 degradation on the initial concentration of dye ranging from 15 to 55 mg L^{-1}. The initial concentration affected the reaction which progressively slowed down as a function of AO7 concentration. For instance, by increasing the initial AO7 concentration, ~80% of AO7 degradation was achieved in 30 min (15 mg L^{-1}), and doubled to 60 min (25 mg L^{-1}) and then increased by more than six fold to 180 min (55 mg L^{-1}). This is attributed to inductive effects caused by the high AO7 concentration, as available active sites were predominantly covered by the dye molecules. As a result, this effect limits the amount of H_2O_2 freely available to interact with the active sites of the GO–Fe_3O_4 nanocomposite for effective generation of HO• radicals. Similar behaviour was also reported elsewhere for the oxidation of dyes [39,40].

The profile of normalised concentrations with time (Fig. 4a) follows an exponential pattern, which may describe the degradation of AO7 according to the pseudo-first-order kinetics reaction:

$$\frac{-dC_{AO7}}{dt} = k_{obs}(C_{AO7}) \quad (8)$$

where the C_{AO7} represents the concentration of AO7 (mg L^{-1}) at time t and k_{obs} is the pseudo first-order rate constant (min^{-1}) for the degradation of AO7. The integration of Eq. (8) yields Eq. (9).

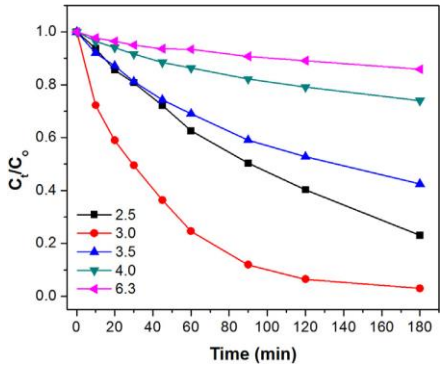

Fig. 2. Effect of initial pH on the degradation of AO7. Experimental conditions: AO7 = 35 mg L^{-1}; Dosage = 0.2 g L^{-1}; H_2O_2 = 22 mM and 298 K.

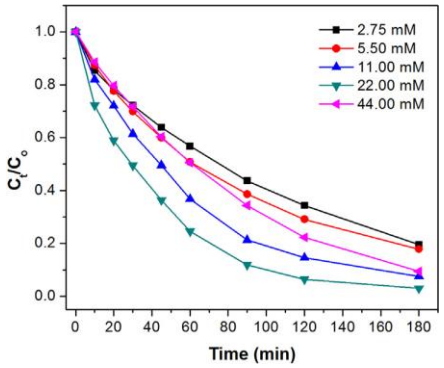

Fig. 3. Effect of H_2O_2 concentration on the degradation of AO7. Experimental conditions: AO7 = 35 mg L^{-1}; Dosage = 0.2 g L^{-1}; pH = 3 and 298 K.

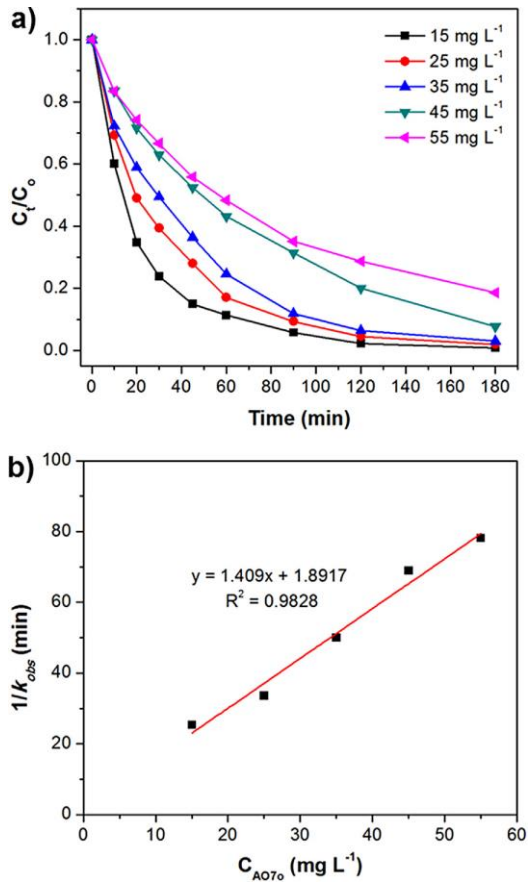

Fig. 4. (a) Effect of dye initial concentration on the degradation of AO7. (b) Relationship between the $1/k_{obs}$ and C_{AO7_0} using Langmuir–Hinshelwood model. Experimental conditions: Dosage = 0.2 g L^{-1}; H_2O_2 = 22 mM; pH = 3 and 298 K.

$$\ln \frac{C_{AO7_0}}{C_{AO7}} = k_{obs}t \quad (9)$$

The slope of the straight line for a plot of $\ln(C_{AO7_0}/C_{AO7})$ vs. t determines the k_{obs} value which are summarised in Table S1 (see Supplementary information). The results in this work shown that the k_{obs} values decreased as the initial concentration increased.

The heterogeneous reaction for the degradation of organics encompasses with both reaction and adsorption that occurs simultaneously [41], and can be described by the Langmuir–Hinshelwood mechanism [39,42], which can be expressed as follows:

$$k_{obs} = \frac{k_c K_{AO7}}{1 + K_{AO7} C_{AO7_0}} \quad (10)$$

$$\frac{1}{k_{obs}} = \frac{1}{k_c}(C_{AO7_0}) + \frac{1}{k_c K_{AO7}} \quad (11)$$

where the k_c is the intrinsic surface reaction rate constant (mg L^{-1} min^{-1}) and K_{AO7} is the Langmuir–Hinshelwood adsorption equilibrium constant (L mg^{-1}). The values of k_c and K_{AO7} can be calculated by plotting the ($1/k_{obs}$) against C_{AO7_0}. As can be seen in Fig. 4b, the experimental data fits reasonably well (R^2 = 0.983) with the proposed Langmuir–Hinshelwood mechanism. In other words, the catalytic surface reactions between the nanocomposite active sites, AO7 and HO• radicals can be used in determining the kinetics of the heterogeneous reaction. The k_c and K_{AO7} values were calculated as 0.710 mg L^{-1} min^{-1} and 0.745 L mg^{-1}, respectively. The K_{AO7} value was found to be lower than the sorption constant (K_L = 1.109 L mg^{-1}) in absence of oxidant according to the Langmuir adsorption model as shown in Fig. S1 and Table S2 (see Supplementary information), indicating the existence of competitive adsorption between AO7 and H_2O_2 towards the active sites during the reaction.

The temperature has a pronounced effect on AO7 degradation as shown in Fig. 5a. Fast rates are observed within minutes for an AO7 concentration of 35 mg L^{-1} (expected in textile wastewater), and 80% degradation was reached less than ~20 min at 328 K. Longer reaction time of ~70 min is required as the temperature is reduced to 298 K. Hence, raising the temperature of the reaction likewise increases k_{obs}, translating in shorter reaction time. This phenomenon is attributed to the exponential dependency of k_{obs} with reaction temperature in accordance with the Arrhenius's law. High temperature leads to an increased rate between H_2O_2 and the active sites of GO–Fe_3O_4 nanocomposite in generating more HO• radicals to readily oxidised AO7. These results suggest that the mobility of AO7 and H_2O_2 towards the surface of active sites are promoted by increasing reaction temperature. However, raising the temperature from ambient conditions at 298–328 K requires energy, which in turn affects the operating costs of wastewater treatment. Unless a source of waste heat is available, or solar heat can be used effectively, 298 K was chosen in this work as the preferred temperature in the heterogeneous Fenton-like reaction due to the consideration of the potential operating costs.

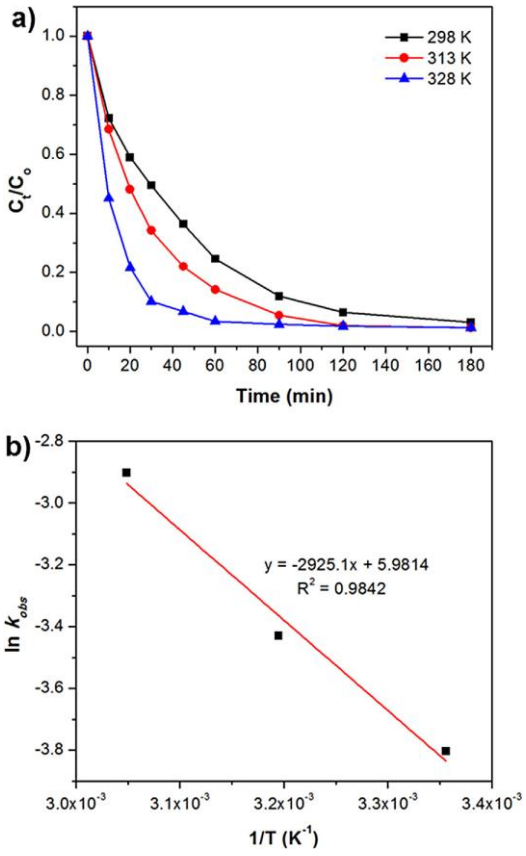

Fig. 5. (a) Effect of temperature on AO7 degradation. (b) Arrhenius plot of reaction rate constant. Experimental conditions: AO7 = 35 mg L^{-1}; Dosage = 0.2 g L^{-1}; H_2O_2 = 22 mM and pH 3.

The k_{obs} parameter for the AO7 degradation for each temperature was calculated to determine the activation energy of reaction. It was found that the k_{obs} values at temperatures of 298, 313 and 328 K were 0.022, 0.032 and 0.053 min^{-1}, respectively. The correlation between temperature and k_{obs} can be presented in Fig. 5b using the linear form of Arrhenius equation:

$$\ln k_{obs} = \ln A + \left(\frac{-E_a}{RT}\right) \quad (12)$$

where A is a constant, R is the gas constant (8.314 J mol^{-1} K^{-1}), T is the solution temperature and E_a is the activation energy. The E_a was found to be 24.3 kJ mol^{-1}. This value is higher than E_a of the diffusion-controlled reaction that usually ranges within 10–13 kJ mol^{-1} [43], which implies that the k_{obs} for this heterogeneous reaction is dominated by the rate of intrinsic chemical reactions on the surface of active sites rather than the rate of mass transfer as reported elsewhere [39,44].

Global optimisation

The optimisation carried out so far follows one dimensional pattern for a single condition. Hence, there is a need to understand the best global optimised condition. To address this point, a 2^3-factorial design was used to elucidate the global interaction based on a face centred central composite design (FCCD) under response surface methodology (RSM). Three significant parameters (i.e. dosage, pH and temperature) and their ranges were chosen based on the findings of one-parameter-at-a-time method. The details of the design matrix and the response surface regression analysis are presented in Tables S3 and S4, respectively (Supplementary information). From the analysis of variance (ANOVA) of response surface regression, an empirical relationship between the degradation of AO7 and the coded parameters was expressed by the following equation:

$$\begin{aligned}\text{Degradation of AO7}(\%) = {} & 95.89 + 2.82A - 6.25B + 3.66C \\ & + 0.38AB + 2.29AC + 3.15BC \\ & - 1.86A^2 - 19.44B^2 + 0.36C^2 \end{aligned} \quad (13)$$

This derived model is graphically represented through the contour plot (Fig. 6a). This plot illustrates the interactive effects between the pH and temperature at optimal dosage of 0.205 g L^{-1} on the degradation of AO7. At the same time, determination of the optimal condition between those parameters can be facilitated by the elliptical nature of the contour plots. Validation of derived model was confirmed by diagnostic plot (Fig. 6b), which shows high correlation between the experimental and predicted values. The model adequacy was corroborated by the high coefficient value of 0.9742, hence given confidence to the global optimised results.

From this analysis, the optimal condition for degradation of AO7 was obtained at dosage of 0.205 g L^{-1}, pH of 3 and temperature of 326.7 K with desirability of 1. In one hand, raising the temperature is beneficial in terms of increasing the reaction kinetics. On the other hand, the increase in temperature must be traded off against energy input to the reaction which attracts extra undesirable operational cost. Unless free waste heat is available, we have considered 298 K as the preferred temperature in the heterogeneous Fenton-like reaction. Based on these findings, there

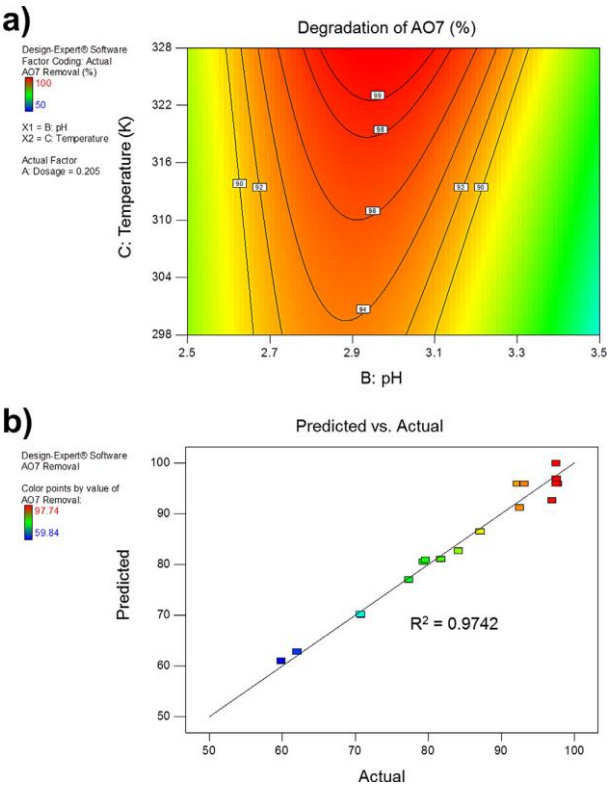

Fig. 6. (a) Contour plot of the derived response surface quadratic model. (b) Correlation between the actual and predicted degradation of AO7.

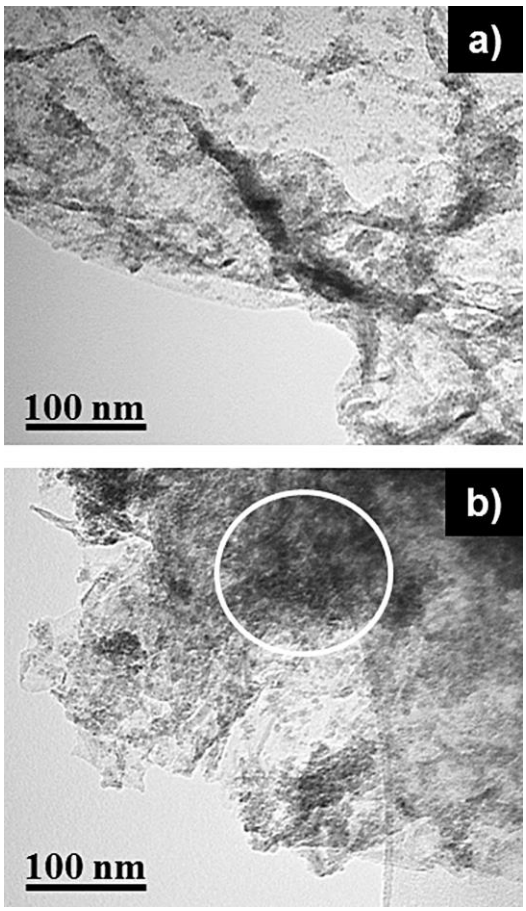

Fig. 7. TEM images of pristine (a) and spent (b) GO–Fe_3O_4 nanocomposites.

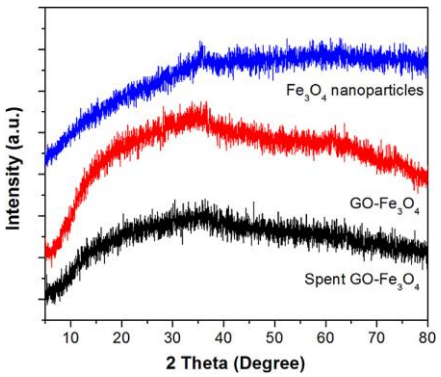

Fig. 8. XRD patterns of Fe_3O_4 nanoparticles, pristine and spent GO–Fe_3O_4 nanocomposites.

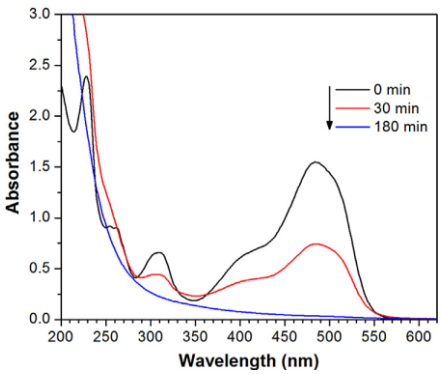

Fig. 10. UV–vis spectra changes during the oxidative degradation of AO7 by GO–Fe_3O_4 nanocomposite in the presence of H_2O_2. Experimental conditions: AO7 = 35 mg L^{-1}; Dosage = 0.2 g L^{-1}; H_2O_2 = 22 mM; pH = 3 and 298 K.

are no significant differences (except for temperature) on the optimal condition between the one-parameter-at-a-time and the global optimisation.

Characterisation

The analysis of spent GO–Fe_3O_4 nanocomposite was performed to compare against its pristine properties. TEM images in Fig. 7 indicate that there are no significant differences in the morphology between both samples. The Fe_3O_4 nanoparticles were well dispersed throughout the surface of GO sheets in both cases. There is a slight aggregation within the corrugated GO surfaces in both cases. This is attributed to the surface defects and edges of GO which facilitates the nucleation and growth of the Fe_3O_4 nanoparticles [45]. However, there is a thick area on the spent nanocomposite in Fig. 7b (highlighted white circle) possibly originating from disorder stacking of GO–Fe_3O_4 nanocomposite. XRD patterns in Fig. 8 show that both pristine and spent GO–Fe_3O_4 nanocomposites exhibited relatively weak and broad diffraction peaks similar to Fe_3O_4 nanoparticles. Interestingly, the phase of Fe_3O_4 remained unchanged throughout the AO7 oxidation reaction because no discernible changes in diffraction peaks of spent catalyst were observed.

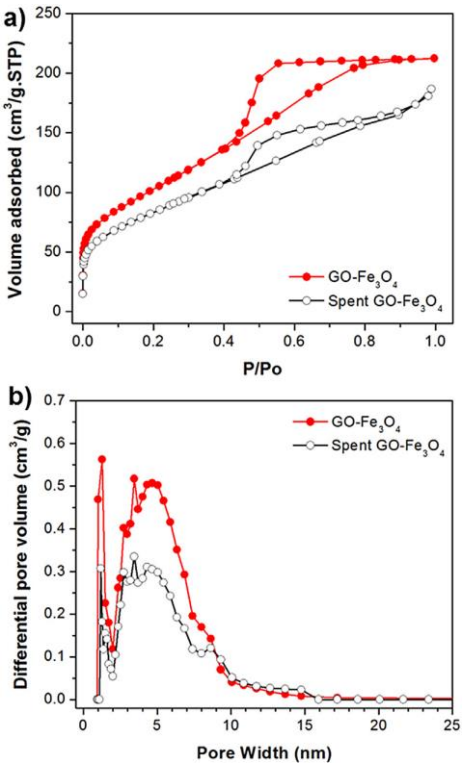

Fig. 9. Isotherms (a) and pore size distribution (b) of pristine and spent GO–Fe_3O_4 nanocomposites.

Minor changes were observed between the nitrogen isotherms of spent and pristine GO–Fe_3O_4 nanocomposites as displayed in Fig. 9a. Both isotherms are of type IV with H2 hysteresis loop, indicative of mesoporous structures. The spent sample resulted in surface area loss of 19.7% (from 373 to 300 $m^2 g^{-1}$) and pore volume loss of 15.6% (from 0.328 to 0.277 $cm^3 g^{-1}$). These results suggest that the spent nanocomposite underwent structural densification, though the pore size distribution remained similar to the pristine catalyst (Fig. 9b). The spent nanocomposite was washed, dried and degassed prior to the nitrogen adsorption testing. If the intermediates of the AO7 degradation through carbon deposition remained adsorbed, then this could explain the loss in both the surface area and volume of the spent nanocomposite. Alternatively, there may have been re-stacking of the GO sheets during successive catalytic reaction, washing and drying processes, thus reflecting the observed changes.

Finally, the total carbon (TC) analysis showed that 90.48% of carbon was successfully being removed and decomposed into carbon dioxide after undergoing 180 min of reaction. This can be clearly seen in Fig. 10 as the degradation of AO7 was monitored by UV–vis spectra. There are three absorbance peaks at 484, 310, and 230 nm and one shoulder at 430 nm. The peaks at 484 and 430 nm in the visible region are ascribed to the hydrazone and azo form, whilst the other two peaks, at 310 and 230 nm in the ultraviolet region, are assigned to the naphthalene and benzene rings of AO7, respectively [6]. The absorbance at 310 and 230 nm increased slightly in the first 30 min, attributed to the formation of naphthalene- and/or benzene-type intermediates during catalysis. All peaks almost disappeared at 180 min of reaction due to the destruction of azo bond (—N═N—) in the chromophoric structure of AO7.

Conclusions

The degradation of AO7 dye by the heterogeneous Fenton-like reaction was systematically investigated using GO–Fe_3O_4 nanocomposite catalyst. The optimal operational condition was

obtained with a catalyst concentration of 0.2 g L^{-1}, an initial pH of 3 and 22 mM of H_2O_2 concentration at 298 K. The AO7 degradation was mainly ascribed to heterogeneous Fenton-like reaction and well described by a pseudo-first-order kinetic through the Langmuir–Hinshelwood mechanism. This heterogeneous reaction is dominated by the rate of intrinsic chemical reactions on the surface of active sites rather than the rate of mass transfer. The GO–Fe_3O_4 nanocomposite delivered best AO7 degradation of 98%. The spent catalysts was mainly stable, as the Fe_3O_4 phase remained similar to a pristine catalyst, though minor changes in surface area and pore volume were observed possibly attributed to the adsorption of intermediates or re-stacking of the GO–Fe_3O_4 sheets during the reaction. These findings present new insights into the influence of operational parameters in the heterogeneous Fenton-like oxidation of AO7 using GO–Fe_3O_4 nanocomposite.

Acknowledgments

The authors acknowledge the assistance of Dr Julius Motuzas, and the facilities and the scientific and technical assistance of the Australian Microscopy & Microanalysis Research Facility at the Centre for Microscopy and Microanalysis, The University of Queensland. Nor Aida Zubir gratefully acknowledges the generous financial support from Ministry of Higher Education Malaysia (MOHE) and Universiti Teknologi MARA (UiTM) for her study leave. X. Zhang thanks the Australia Research Council for the support on Discovery Project (DP110103533) and his Australian Research Fellowship. J. C. Diniz da Costa acknowledges support via the Australian Research Council Future Fellowship Program (FT130100405).

Appendix A. Supplementary data

Supplementary data associated with this article can be found, in the online version, at http://dx.doi.org/10.1016/j.endend.2009.01.011.

References

[1] V.M. Correia, T. Stephenson, S.J. Judd, Characterisation of textile wastewaters – a review, Environ. Technol. 15 (1994) 917–929, doi:http://dx.doi.org/10.1080/09593339409385500.
[2] M. Aleksić, H. Kušić, N. Koprivanac, D. Leszczynska, A.L. Božić, Heterogeneous Fenton type processes for the degradation of organic dye pollutant in water – the application of zeolite assisted AOPs, Desalination 257 (2010) 22–29, doi:http://dx.doi.org/10.1016/j.desal.2010.03.016.
[3] J. Labanda, J. Sabaté, J. Llorens, Modeling of the dynamic adsorption of an anionic dye through ion-exchange membrane adsorber, J. Membr. Sci. 340 (2009) 234–240, doi:http://dx.doi.org/10.1016/j.memsci.2009.05.036.
[4] S.P. Sun, C.J. Li, J.H. Sun, S.H. Shi, M.H. Fan, Q. Zhou, Decolorization of an azo dye orange G in aqueous solution by Fenton oxidation process: effect of system parameters and kinetic study, J. Hazard. Mater. 161 (2009) 1052–1057, doi:http://dx.doi.org/10.1016/j.jhazmat.2008.04.080. 18538927.
[5] J.H. Ramirez, F.M. Duarte, F.G. Martins, C.A. Costa, L.M. Madeira, Modelling of the synthetic dye Orange II degradation using Fenton's reagent: from batch to continuous reactor operation, Chem. Eng. J. 148 (2009) 394–404, doi:http://dx.doi.org/10.1016/j.cej.2008.09.012.
[6] S.H. Tian, Y.T. Tu, D.S. Chen, X. Chen, Y. Xiong, Degradation of Acid Orange II at neutral pH using $Fe_2(MoO_4)_3$ as a heterogeneous Fenton-like catalyst, Chem. Eng. J. 169 (2011) 31–37, doi:http://dx.doi.org/10.1016/j.cej.2011.02.045.
[7] N.K. Daud, M.A. Ahmad, B.H. Hameed, Decolorization of acid Red 1 dye solution by Fenton-like process using Fe–montmorillonite K10 catalyst, Chem. Eng. J. 165 (2010) 111–116, doi:http://dx.doi.org/10.1016/j.cej.2010.08.072.
[8] P.P. Gan, S.F.Y. Li, Efficient removal of rhodamine B using a rice hull-based silica supported iron catalyst by Fenton-like process, Chem. Eng. J. 229 (2013) 351–363, doi:http://dx.doi.org/10.1016/j.cej.2013.06.020.
[9] J.H. Ramirez, F.J. Maldonado-Hódar, A.F. Pérez-Cadenas, C. Moreno-Castilla, C. A. Costa, L.M. Madeira, Azo-dye Orange II degradation by heterogeneous Fenton-like reaction using carbon-Fe catalysts, Appl. Catal. B Environ. 75 (2007) 312–323, doi:http://dx.doi.org/10.1016/j.apcatb.2007.05.003.
[10] X. Hu, B. Liu, Y. Deng, H. Chen, S. Luo, C. Sun, P. Yang, S. Yang, Adsorption and heterogeneous Fenton degradation of 17α-methyltestosterone on nano Fe_3O_4/MWCNTs in aqueous solution, Appl. Catal. B Environ. 107 (2011) 274–283, doi:http://dx.doi.org/10.1016/j.apcatb.2011.07.025.
[11] S. Navalon, A. Dhakshinamoorthy, M. Alvaro, H. Garcia, Heterogeneous Fenton catalysts based on activated carbon and related materials, ChemSusChem 4 (2011) 1712–1730, doi:http://dx.doi.org/10.1002/cssc.201100216. 22162405.
[12] H. Hassan, B.H. Hameed, Fe–clay as effective heterogeneous Fenton catalyst for the decolorization of reactive Blue 4, Chem. Eng. J. 171 (2011) 912–918, doi:http://dx.doi.org/10.1016/j.cej.2011.04.040.
[13] T.D. Nguyen, N.H. Phan, M.H. Do, K.T. Ngo, Magnetic Fe_2MO_4 (M:Fe, Mn) activated carbons: fabrication, characterization and heterogeneous Fenton oxidation of methyl orange, J. Hazard. Mater. 185 (2011) 653–661, doi:http://dx.doi.org/10.1016/j.jhazmat.2010.09.068. 20952129.
[14] A. Rodriguez, G. Ovejero, J.L. Sotelo, M. Mestanza, J. Garcia, Heterogeneous Fenton catalyst supports screening for mono azo dye degradation in contaminated wastewaters, Ind. Eng. Chem. Res. 49 (2010) 498–505, doi:http://dx.doi.org/10.1021/ie901212m.
[15] Z. Yaping, H. Jiangyong, Photo-Fenton degradation of 17β-estradiol in presence of α-FeOOHR and H_2O_2, Appl. Catal. B Environ. 78 (2008) 250–258, doi:http://dx.doi.org/10.1016/j.apcatb.2007.09.026.
[16] J. Deng, X. Wen, Q. Wang, Solvothermal in situ synthesis of Fe_3O_4-multi-walled carbon nanotubes with enhanced heterogeneous Fenton-like activity, Mater. Res. Bull. 47 (2012) 3369–3376, doi:http://dx.doi.org/10.1016/j.materresbull.2012.07.021.
[17] S. Song, R. Rao, H. Yang, H. Liu, A. Zhang, Facile synthesis of Fe_3O_4/MWCNTs by spontaneous redox and their catalytic performance, Nanotechnology 21 (2010) 185602–185607, doi:http://dx.doi.org/10.1088/0957-4484/21/18/185602.
[18] S. Song, H. Yang, R. Rao, H. Liu, A. Zhang, High catalytic activity and selectivity for hydroxylation of benzene to phenol over multi-walled carbon nanotubes supported Fe_3O_4 catalyst, Appl. Catal. A Gen. 375 (2010) 265–271, doi:http://dx.doi.org/10.1016/j.apcata.2010.01.008.
[19] Y. Dong, J. Li, L. Shi, J. Xu, X. Wang, Z. Guo, W. Liu, Graphene oxide-iron complex: synthesis, characterization and visible-light-driven photocatalysis, J. Mater. Chem. A 1 (2013) 644–650, doi:http://dx.doi.org/10.1039/c2ta00371f.
[20] S. Guo, G. Zhang, Y. Guo, J.C. Yu, Graphene oxide–Fe_2O_3 hybrid material as highly efficient heterogeneous catalyst for degradation of organic contaminants, Carbon 60 (2013) 437–444, doi:http://dx.doi.org/10.1016/j.carbon.2013.04.058.
[21] K.V. Voitko, R.L.D. Whitby, V.M. Gun'ko, O.M. Bakalinska, M.T. Kartel, K. Laszlo, A.B. Cundy, S.V. Mikhalovsky, Morphological and chemical features of nano and macroscale carbons affecting hydrogen peroxide decomposition in aqueous media, J. Coll. Interf. Sci. 361 (2011) 129–136, doi:http://dx.doi.org/10.1016/j.jcis.2011.05.048. 21676406.
[22] D.R. Dreyer, S. Park, C.W. Bielawski, R.S. Ruoff, The chemistry of graphene oxide, Chem. Soc. Rev. 39 (2010) 228–240, doi:http://dx.doi.org/10.1039/b917103g. 20023850.
[23] C. Su, K.P. Loh, Carbocatalysts: graphene oxide and its derivatives, Acc. Chem. Res. 46 (2013) 2275–2285.
[24] Y. Matsumoto, M. Koinuma, S. Ida, S. Hayami, T. Taniguchi, K. Hatakeyama, H. Tateishi, Y. Watanabe, S. Amano, Photoreaction of graphene oxide nanosheets in water, J. Phys. Chem. C 115 (2011) 19280–19286, doi:http://dx.doi.org/10.1021/jp206348s.
[25] A. Lerf, H. He, M. Forster, J. Klinowski, Structure of graphite oxide revisited, J. Phys. Chem. B102 (1998) 4477–4482.
[26] M.Z. Kassaee, E. Motamedi, M. Majdi, Magnetic Fe_3O_4-graphene oxide/polystyrene: fabrication and characterization of a promising nanocomposite, Chem. Eng. J. 172 (2011) 540–549, doi:http://dx.doi.org/10.1016/j.cej.2011.05.093.
[27] C. Xu, X. Wang, Graphene oxide-mediated synthesis of stable metal nanoparticle colloids, Coll. Surf. A Physicochem. Eng. Asp. 404 (2012) 78–82, doi:http://dx.doi.org/10.1016/j.colsurfa.2012.04.017.
[28] R. Matta, K. Hanna, S. Chiron, Fenton-like oxidation of 2,4,6-trinitrotoluene using different iron minerals, Sci. Total Environ. 385 (2007) 242–251, doi:http://dx.doi.org/10.1016/j.scitotenv.2007.06.030. 17662375.
[29] R.C.C. Costa, M.F.F. Lelis, L.C.A. Oliveira, J.D. Fabris, J.D. Ardisson, R.R.V.A. Rios, C. N. Silva, R.M. Lago, Novel active heterogeneous Fenton system based on $Fe_{3-x}M_xO_4$ (Fe, Co, Mn, Ni): the role of M^{2+} species on the reactivity towards H_2O_2 reactions, J. Hazard. Mater. 129 (2006) 171–178, doi:http://dx.doi.org/10.1016/j.jhazmat.2005.08.028. 16298475.
[30] N.A. Zubir, X. Zhang, C. Yacou, J.C. Diniz da Costa, Fenton-like degradation of acid Orange 7 using graphene oxide-iron oxide nanocomposite, Sci. Adv. Mater. 6 (2014) 1382–1388, doi:http://dx.doi.org/10.1166/sam.2014.1812.
[31] N.A. Zubir, C. Yacou, J. Motuzas, X. Zhang, J.C. Diniz da Costa, Structural and functional investigation of graphene oxide–Fe_3O_4 nanocomposites for the heterogeneous Fenton-like reaction, Sci. Rep. 4 (2014) 4594, doi:http://dx.doi.org/10.1038/srep04594. 24699690.
[32] W.S. Hummers, R.E. Offeman, Preparation of graphitic oxide, J. Am. Chem. Soc. 80 (1958) 1339, doi:http://dx.doi.org/10.1021/ja01539a017.
[33] Z. Xiong, L.L. Zhang, X.S. Zhao, Visible-light-induced dye degradation over copper-modified reduced graphene oxide, Chem. (Weinheim an Der Bergstrasse, Germany) 17 (2011) 2428–2434, doi:http://dx.doi.org/10.1002/chem.201002906. 21319236.
[34] F. Duarte, F.J. Maldonado-Hódar, L.M. Madeira, New insight about orange II elimination by characterization of spent activated carbon/Fe Fenton-like catalysts, Appl. Catal. B Environ. 129 (2013) 264–272, doi:http://dx.doi.org/10.1016/j.apcatb.2012.09.037.
[35] R. Gonzalez-Olmos, U. Roland, H. Toufar, F.D. Kopinke, A. Georgi, Fe-zeolites as catalysts for chemical oxidation of MTBE in water with H_2O_2, Appl. Catal. B

Environ. 89 (2009) 356–364, doi:http://dx.doi.org/10.1016/j.apcatb.2008.12.014.
[36] J. Herney-Ramirez, M. Lampinen, M.A. Vicente, C.A. Costa, L.M. Madeira, Experimental design to optimize the oxidation of Orange II dye solution using a clay-based Fenton-like catalyst, Ind. Eng. Chem. Res. 47 (2007) 284–294.
[37] N.K. Daud, B.H. Hameed, Decolorization of acid Red 1 by Fenton-like process using rice husk ash-based catalyst, J. Hazard. Mater. 176 (2010) 938–944, doi:http://dx.doi.org/10.1016/j.jhazmat.2009.11.130. 20042285.
[38] J.H. Ramirez, C.A. Costa, L.M. Madeira, G. Mata, M.A. Vicente, M.L. Rojas-Cervantes, A.J. López-Peinado, R.M. Martín-Aranda, Fenton-like oxidation of Orange II solutions using heterogeneous catalysts based on saponite clay, Appl. Catal. B Environ. 71 (2007) 44–56, doi:http://dx.doi.org/10.1016/j.apcatb.2006.08.012.
[39] X. Xue, K. Hanna, M. Abdelmoula, N. Deng, Adsorption and oxidation of PCP on the surface of magnetite: kinetic experiments and spectroscopic investigations, Appl. Catal. B Environ. 89 (2009) 432–440, doi:http://dx.doi.org/10.1016/j.apcatb.2008.12.024.
[40] J. Herney-Ramirez, A.M.T. Silva, M.A. Vicente, C.A. Costa, L.M. Madeira, Degradation of acid Orange 7 using a saponite-based catalyst in wet hydrogen peroxide oxidation: kinetic study with the Fermi's equation, Appl. Catal. B Environ. 101 (2011) 197–205, doi:http://dx.doi.org/10.1016/j.apcatb.2010.09.020.
[41] W. Xu, J.S. Kong, Y.-T.E. Yeh, P. Chen, Single-molecule nanocatalysis reveals heterogeneous reaction pathways and catalytic dynamics, Nat. Mater. 7 (2008) 992–996, doi:http://dx.doi.org/10.1038/nmat2319. 18997774.
[42] N. Daneshvar, M.H. Rasoulifard, A.R. Khataee, F. Hosseinzadeh, Removal of C.I. Acid Orange 7 from aqueous solution by UV irradiation in the presence of ZnO nanopowder, J. Hazard. Mater. 143 (2007) 95–101, doi:http://dx.doi.org/10.1016/j.jhazmat.2006.08.072. 17030415.
[43] W. Stumm, J.J. Morgan, Aquatic Chemistry: Chemical Equilibria and Rates in Natural Waters, third edition, Wiley Interscience, New York, 1996.
[44] S.-S. Lin, M.D. Gurol, Catalytic decomposition of hydrogen peroxide on iron oxide: kinetics, mechanism, and implications, Environ. Sci. Technol. 32 (1998) 1417–1423, doi:http://dx.doi.org/10.1021/es970648k.
[45] Z.G. Geng, Y. Lin, X.X. Yu, Q.H. Shen, L. Ma, Z.Y. Li, N. Pan, X.P. Wang, Highly efficient dye adsorption and removal: a functional hybrid of reduced graphene oxide-Fe_3O_4 nanoparticles as an easily regenerative adsorbent, J. Mater. Chem. 22 (2012) 3527–3535, doi:http://dx.doi.org/10.1039/c2jm15544c.

Chapter 6

Recyclability and longevity of the catalyst based on the synergistic effect of GO and iron oxide in the heterogeneous Fenton-like reaction

Abstract

This work shows for the first time that the recyclability and longevity of the catalyst is associated with the synergistic interfacial effects between iron oxide (Fe_3O_4) nanoparticles and graphene oxide (GO). This is evidenced by the continuous, constant performance of GO–Fe_3O_4 nanocomposites, contrary to a conventional iron oxide catalyst which exhibited a severe loss of activity for the oxidative degradation of acid orange 7 (AO7) in the heterogeneous Fenton-like reaction. The GO–Fe_3O_4 nanocomposites exhibited superior stability with more than 98% AO7 removal compared to the bare Fe_3O_4 nanoparticles. It is postulated that this stability is attributed to the fast regeneration of immobilised ferrous ions to catalytically decompose hydrogen peroxide into hydroxyl radicals due to the intrinsic donor-acceptor surface properties of GO. This proposed stability mechanism is supported by the X-ray spectroscopy (XPS) analysis, which shed light on the different behaviour of surface activity between the nanocomposites and bare nanoparticles after undergoing successive cycles of reaction.

6.1 Introduction

The employment of environmentally benign technologies to treat industrial wastewaters is becoming paramount, particularly to meet stringent environmental regulations. The heterogeneous Fenton reaction offers many advantages to process wastewaters loaded with undesirable refractory organic compounds using cheap iron oxide catalyst and hydrogen peroxide (H_2O_2) oxidant. The downside of this process is the lack of recyclability of the iron oxide as these catalysts continuously lose their activity after a few reaction cycles, thus requiring the addition of fresh catalysts. To address this lack of recyclability, immobilisation of iron oxide nanoparticles (NPs) onto the surface of solid supports has gained increasing attention in heterogeneous catalysis [1-6]. The modulation of overall catalytic

activity is intimately related to the nature and properties of the supports [7], as well as the specific interaction between the iron oxide's active sites and the supports [8]. Various types of carbonaceous materials such as activated carbons [9, 10], carbon aerogel [9], mesoporous carbon [11], carbon nanotubes [2, 12, 13], graphene and its derivative graphene oxide (GO) [14, 15] have been considered as promising supports in the oxidative degradation of refractory organic pollutants. Moreover, these carbonaceous materials could also act as co-catalysts due to the donor–acceptor properties of the carbon surfaces based on an electron-transfer mechanism similar to the Fenton reaction [16, 17].

Among them, the deposition of NPs onto the unique two-dimensional structure of graphene or GO is desirable due to the highly effective surface area and the lack of ink-bottle pores [18]. These allow high accessibility of reactants towards the actives sites which are able to diminish limitations in mass transfer during catalysis. Further, GO exhibits a highly heterogeneous electronic structure determined by the interplay of conducting π-states from sp^2 carbon atoms within the large energy gap (σ-states) of sp^3 domains with oxygenated functional groups [19-21]. Thus, the changes in carbon to oxygen (C/O) ratio may modify the GO electronic properties from insulating to semiconducting properties [22, 23]. These functional properties of GO have been explored in recent years, by immobilising iron oxide on GO sheets as GO–Fe_3O_4 nanocomposites for the degradation of organic pollutants such as bisphenol A [3], acid orange 7 (AO7) [14], Rhodamine B and 4-nitrophenol [15]. Although these works have shown significant degradation of refractory organic pollutants using the incumbent GO–iron oxide nanocomposites in heterogeneous catalysis, the synergistic interactions between NPs and GO as the catalyst support, which influences the overall catalytic activity, has yet to be fully understood.

Inspired by environmentally benign concepts, this work focuses on a systematic investigation of the recyclability and long-term stability performance of GO–Fe_3O_4 nanocomposites for the heterogeneous Fenton-like oxidation of AO7, which is an organic compound pollutant of worldwide significance used in the production of textiles. To this end, the underlying interactions of the GO and iron oxide NPs are fully explored and explained based on the characterisation of both pristine and spent materials at their respective cycles of reaction. Moreover, a mechanism on the synergistic effect of GO–Fe_3O_4 is proposed to provide new insights into the recyclability and longevity of this hybrid catalyst in the heterogeneous Fenton-like reaction.

6.2 Experimental

6.2.1 Preparation of GO–Fe_3O_4 nanocomposites

The GO–Fe_3O_4 nanocomposites were prepared by co-precipitating pre-hydrolysed ferric and ferrous salts in the presence of GO as described previously [14]. Briefly, an aqueous suspension of GO solution was first prepared by 30 min ultrasonication of graphite oxide. The precursor solution (100 mL) containing $FeCl_3 \cdot 6H_2O$ (4 mmol) and $FeCl_2 \cdot 4H_2O$ (2 mmol) was pre-hydrolysed by the dropwise addition of aqueous NaOH (1 M) under constant stirring. Once the pH of mixture reached pH 4, the GO dispersion (50 mL, 0.55 mg mL^{-1}) was gradually added and stirred for another 30 min until homogeneously mixed. NaOH was then continuously added into the mixture until a pH of 10 was obtained and then the suspension was aged for 30 min. The resulting black precipitate was magnetically separated and washed several times with deionised water and ethanol, and dried at 60 °C for 48 h for further use. For comparison, Fe_3O_4 NPs were also prepared via an analogous condition in the absence of GO.

6.2.2 Catalytic and stability performance

The stability of nanocomposites was tested in continuous operation up to seven cycles at optimised reaction conditions [24] (0.2 g L^{-1} GO–Fe_3O_4, initial pH of 3, 22 mM H_2O_2, 35 mg L^{-1} AO7 at 25 °C) for the oxidative degradation of AO7. The oxidative degradation was carried out without reclaiming the nanocomposite throughout the stability test. A known amount of AO7 stock solution was added into the reaction mixture in each cycle of reaction to keep its initial concentration constant prior to the re-initiation of reaction by H_2O_2. Sampling was carried out periodically and the concentration of AO7 was determined by measuring the absorbance of the solution at 484 nm by Evolution 220 UV-Vis spectrophotometer (Thermo Fisher Scientific).

6.2.3 Characterisation

X-ray photoelectron spectroscopy (XPS) was performed on Kratos Axis ULTRA X-ray photoelectron spectrometer equipped with monochromatic Al Kα (hν = 1486.6 eV) radiation to quantitatively analyse the chemical composition of GO–Fe_3O_4 nanocomposites. The curve fitting was performed using a Gaussian–Lorentzian peak shape and Shirley background function. The C 1s photoelectron binding energy was set at 284.6 eV and used as a reference for calibrating all peak positions. Microstructural investigation was carried out by high resolution transmission electron microscopy (HRTEM, JOEL 2010) with an accelerating voltage of 200 kV. Samples were prepared by placing a

drop of diluted sample dispersion in ethanol onto a carbon-coated copper grid and dried at room temperature. Field emission scanning electron microscope (FESEM) images were obtained using JEOL JSM-7001F. Atomic force microscopy (AFM) images of GO and GO–Fe_3O_4 nanocomposites on a freshly cleaved mica surface were taken with a Veeco MultiMode AFM in tapping mode using OLTESPA-R3 silicon probe (Bruker). The XRD patterns of the nanocomposites were obtained using X-ray diffraction by a Bruker D8 Advance diffractometer operating at 40 kV and 40 mA using filtered Cu Kα radiation (λ = 1.5418 Å). Leaching of iron into solution was analysed by Inductively Coupled Plasma-Optical Emission spectroscopy (ICP-OES) (PerkinElmer).

6.3 Results and discussion

6.3.1 Catalytic and stability performance

Figure 6.1 shows that the GO–Fe_3O_4 nanocomposites exhibited excellent stability compared to the Fe_3O_4 NPs over the seven tested cycles, without losing activity for the degradation of AO7. Conversely, this removal efficiency was found to decline quickly for Fe_3O_4 NPs. The efficiency of the Fe_3O_4 NPs profoundly declined over the second to fifth cycles where the AO7 removal decreased from 70% to nearly 0.7% with no further discernible removal observed in the later cycles. This result is somewhat counter-intuitive, as the iron oxide immobilised onto the GO sheets did not suffer such loss of activity. Therefore, there is a mechanism associated with the synergistic effect between the interfacial interaction of GO and iron oxide which grants the GO–Fe_3O_4 nanocomposites catalytic stability over the tested cycles. In principle, the significant catalytic deactivation experienced by Fe_3O_4 NPs can be described by a combination of passivation effects originating from the possible: (i) formation of a passivated iron oxide surface due to part of the $\equiv Fe^{2+}$ in the outermost layer of the active sites being oxidised to $\equiv Fe^{3+}$ which remained in the latter state due to ineffective regeneration of $\equiv Fe^{2+}$ during catalysis [2, 25], and (ii) surface passivation by adsorbed AO7 and intermediates might physically block the access of H_2O_2 towards the active sites hindering the effective formation of hydroxyl radicals ($HO^{\bullet}$) at the surfaces of active sites [26, 27]. Thus, the lack of surface passivation of GO–Fe_3O_4 nanocomposites confers this catalyst a significant difference as compared to conventional iron oxide catalysts in the heterogeneous Fenton like reaction.

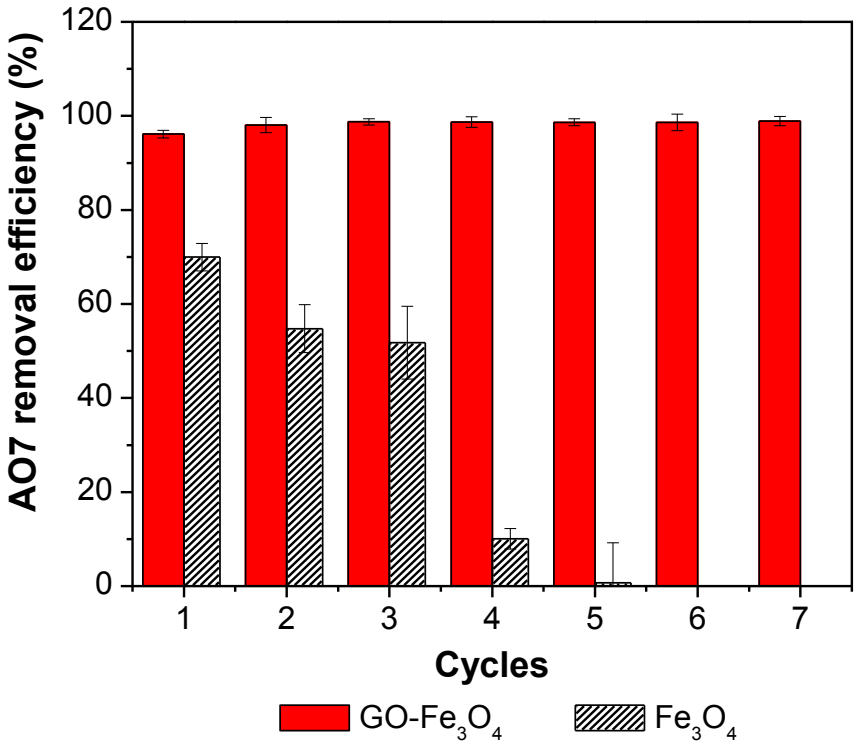

Figure 6.1: AO7 removal in the long-term stability test using GO–Fe_3O_4 nanocomposites and Fe_3O_4 NPs in the heterogeneous Fenton-like reaction.

The stability of the nanocomposites was further assessed by measuring the amount of iron leached into solution after the reaction as shown in Figure 6.2. The maximum leaching concentration amongst the seven cycles was about 0.723 ppm. Such relatively small levels of iron leaching, which are below the European Union directive values (< 2 ppm) [28], indicates that the Fe_3O_4 NPs were strongly deposited on the GO sheets possibly through Fe–O–C bonds [14] rather than homogeneously being dissolved into the reaction mixture. The minor leaching could be attributed to a marginal proportion of loose Fe_3O_4 NPs not bonded to GO sheets. Hence, the contribution of homogeneous reaction towards the total catalytic activity was performed with similar concentration of iron leached (0.8 ppm) at the optimum reaction conditions as presented in Figure 6.2. These results strongly suggest that the degradation of AO7 was dominated by the GO–Fe_3O_4 nanocomposites, rather than by the minor contribution of the leached iron. This is mainly attributed to the heterogeneous catalysis on the surface of the GO–Fe_3O_4 nanocomposites' active sites in producing more $HO^{\bullet}$ radicals to readily oxidise AO7.

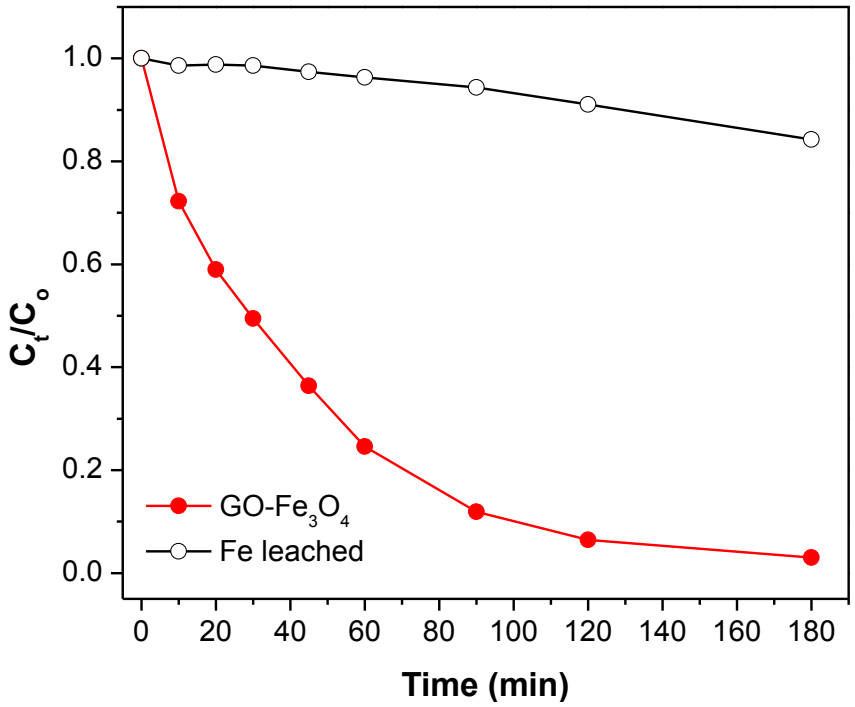

Figure 6.2: The effect of homogeneous and heterogeneous Fenton-like reaction on degradation of AO7. Experimental conditions: AO7 35 mg L^{-1}, H_2O_2 22 mM, pH 3 and T=25 °C.

6.3.2 Nanocomposite characterisation

X-ray photoelectron spectroscopy (XPS) analysis was carried out for both GO–Fe_3O_4 nanocomposites and Fe_3O_4 NPs to elucidate the underlying synergistic effect between the interfacial Fe_3O_4 NPs and GO sheets after their successive use in oxidative degradation of AO7. As shown in Figure 6.3a-b, the Fe 2p spectra of the pristine and spent samples (i.e GO–Fe_3O_4 nanocomposites and Fe_3O_4 NPs) present spin–orbit doublets with binding energies of 711.1 and 724.6 eV, which correspond to Fe $2p_{3/2}$ and Fe $2p_{1/2}$, respectively. Further deconvolution of these peaks into Fe^{3+} and Fe^{2+} components were carried out in order to determine the possible oxidation of the catalyst surface during the catalysis by quantifying the changes in Fe^{3+}/Fe^{2+} ratio. The details of Fe^{3+} and Fe^{2+} peaks with respect to their ratio are summarised in Table 6.1. In both pristine samples of GO–Fe_3O_4 nanocomposites and Fe_3O_4 NPs, the major component was found to be Fe^{3+} which contributed to 65.8 and 66.6% of the total iron surface atoms, respectively, while the remaining 33.8 and 33.3% were in the Fe^{2+} state. The ratio from these values are similar to the literature values [2, 29-31], which corresponds with the Fe_3O_4 crystal structure.

A notable increase in Fe^{3+}/Fe^{2+} ratio after undergoing successive reactions was only observed for the Fe_3O_4 NPs rather than the nanocomposites. The increase in Fe^{3+}/Fe^{2+} ratio from 2.01 to 3.31 could be associated with a proportion of the $\equiv Fe^{2+}$ being oxidised into $\equiv Fe^{3+}$ on the surface of Fe_3O_4 NPs during the heterogeneous Fenton-like reaction. Interestingly, no changes in the ratio of Fe^{3+}/Fe^{2+} were found in the nanocomposites (Table 6.1). These findings plausibly suggest that the regeneration of immobilised ferrous ion ($\equiv Fe^{2+}$) on the active sites of GO–Fe_3O_4 nanocomposites was due to the presence of synergistic interaction between the GO and Fe_3O_4 NPs throughout the catalysis. In fact, these findings are correlate well with the ability of GO–Fe_3O_4 nanocomposites to sustaining a high removal of AO7 (Figure 6.1) compared to the bare Fe_3O_4 NPs during the long-term stability test.

The involvement of the GO during catalysis was further substantiated by the deconvoluted peaks of the O 1s and C 1s spectra as shown in Figure 6.3c and Figure 6.3d, respectively. After the successive reactions, a discernible increase in the relative intensities of O–C=O, C=O and C–O–C, and C–OH peaks were observed in both O 1s and C 1s spectra of GO–Fe_3O_4 nanocomposites. At the same time, the relative intensity of the peak assigned to the C=C was found to be decreasing gradually upon successive reaction cycles. Approximately 18.7% of the sp^2 carbon domain was reduced (Table 6 S1, see Supplementary Information in Appendix C) after seven cycles; which implies that slight oxidation in GO occurred during the catalysis. This can be attributed to the conceivable introduction of defect sites in the GO sheet arising from the oxygenated functional groups attached to the sp^3 carbon. These results strongly suggest that the $HO^{\bullet}$ attacks the peripheral unsaturated bonds of GO planes by electrophilic addition reaction and that there was an incomplete recovery of sp^2 carbon domain during the heterogeneous Fenton-like reaction. This outcome is interesting in the sense that it has not previously been observed for GO, but similar behaviour has been reported for the effect of $HO^{\bullet}$ radicals in the oxidation of carbon nanotubes by Li et al. [32] and Zhang et al. [33].

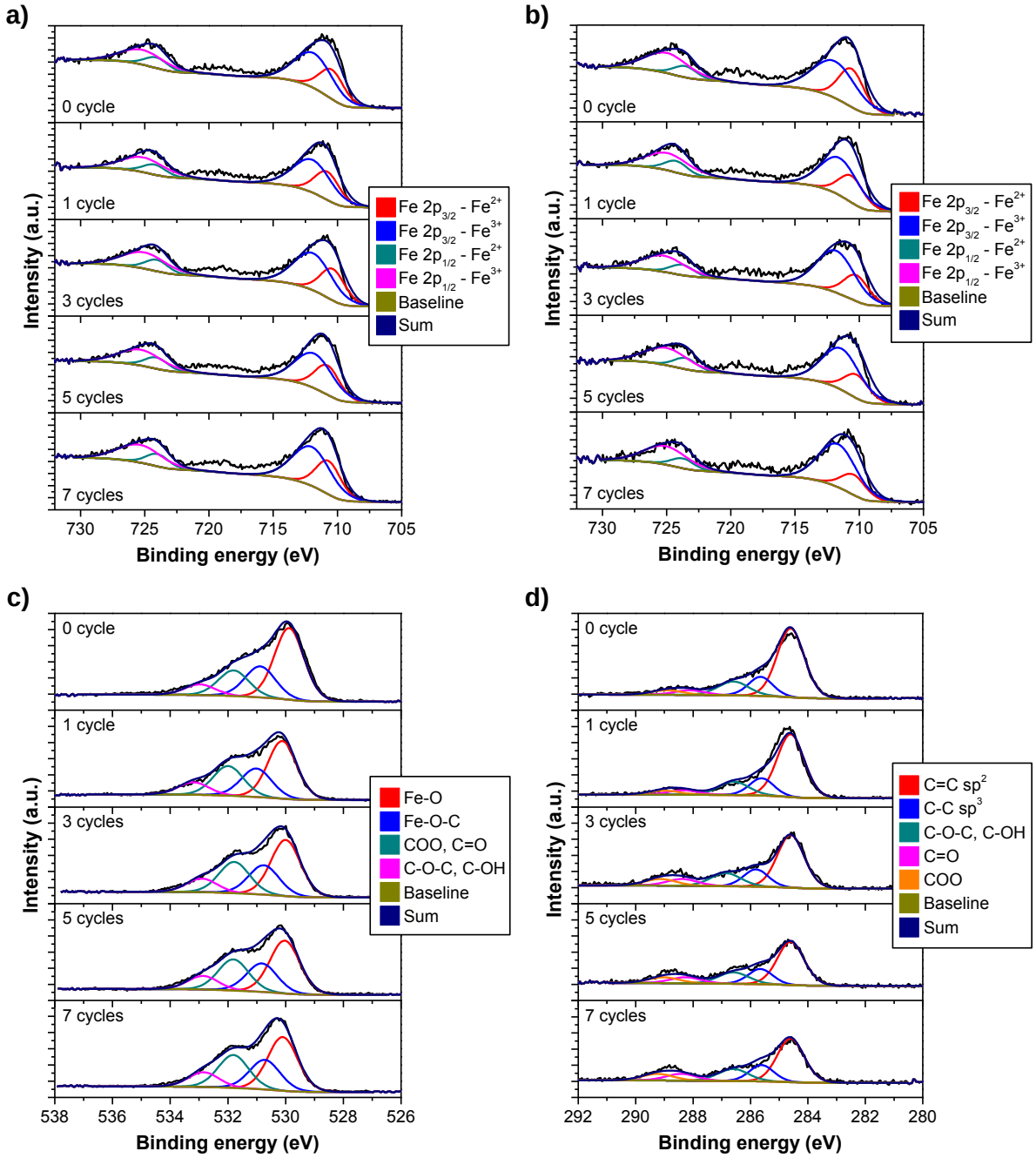

Figure 6.3: Fe 2p core-level XPS spectra of (a) GO–Fe_3O_4 nanocomposites and (b) Fe_3O_4 NPs; (c) O 1s and (d) C 1s core-level XPS spectra GO–Fe_3O_4 nanocomposites before and after long-term stability test.

Table 6.1: Atomic surface concentration of Fe^{3+} and Fe^{2+} on the samples before and after long-term stability test.

Sample	Cycles	Fe $2p_{3/2}$		Fe $2p_{1/2}$		Fe^{3+}/Fe^{2+} ratio
		Fe^{2+} (%)	Fe^{3+} (%)	Fe^{2+} (%)	Fe^{3+} (%)	
Fe_3O_4	0	26.24	43.15	7.026	23.58	2.01
	1	21.51	45.79	8.57	24.13	2.32
	3	20.47	50.02	7.56	21.95	2.57
	5	18.65	49.52	8.14	23.69	2.73
	7	16.07	51.56	7.13	25.24	3.31
GO–Fe_3O_4	0	24.96	44.97	8.31	21.76	2.01
	1	25.01	43.96	8.24	22.79	2.01
	3	24.9	44.53	8.34	22.23	2.01
	5	24.55	43.92	8.71	22.81	2.01
	7	24.85	43.77	8.46	22.91	2.00

The morphology and nanostructure of the GO–Fe_3O_4 nanocomposites were investigated by field emission scanning electron microscopy (FESEM), high resolution transmission electron microscopy (HRTEM) and atomic force microscopy (AFM). High dispersion of Fe_3O_4 NPs deposited across the surface and edges of GO sheets can be clearly observed by FESEM and HRTEM, as presented in Figure 6.4a-c and Figure 6.5a-c. The AFM image (Figure 6.6a) also discloses similar morphology of GO–Fe_3O_4 nanocomposites as observed in both FESEM and HRTEM images. The inset line profile displays uniform height distribution across its lateral dimension with a thickness of about 4 to 5 nm (Figure 6.6a). These findings suggest a uniform coverage of Fe_3O_4 NPs were deposited on the GO surface. The crystallite size of the Fe_3O_4 NPs were calculated to be ~4 nm [24] and the thickness of the GO (Figure 6.6b) was determined at ~1 nm. Therefore, it is inferred that a monolayer of Fe_3O_4 NPs was successfully deposited onto a single layer of GO sheet. Such morphological behaviours are anticipated to be favourable for an effective interaction with H_2O_2 in generating $HO^{\bullet}$ radicals during the catalysis.

In fact, the spent nanocomposites (Figure 6.4d-f and Figure 6.5d-f) still presented relatively similar morphological features with the pristine nanocomposites, although some slightly thicker areas were spotted on the spent nanocomposites (Figure 6.5d); suggesting to possible disordered stacking between nanocomposites during catalysis. The distance between the adjacent lattice fringes in both pristine and spent nanocomposites (Figure 6.5c, f) were about 0.25 nm, which corresponds well to the (311) lattice planes of Fe_3O_4. In addition, no phase change of Fe_3O_4 NPs was observed in the spent nanocomposites as shown in Figure 6.S1 (see Supplementary Information in Appendix C). Collectively, these observations proved the stability and recyclability of GO–Fe_3O_4 nanocomposites catalyst after undergoing successive seven cycles of reaction.

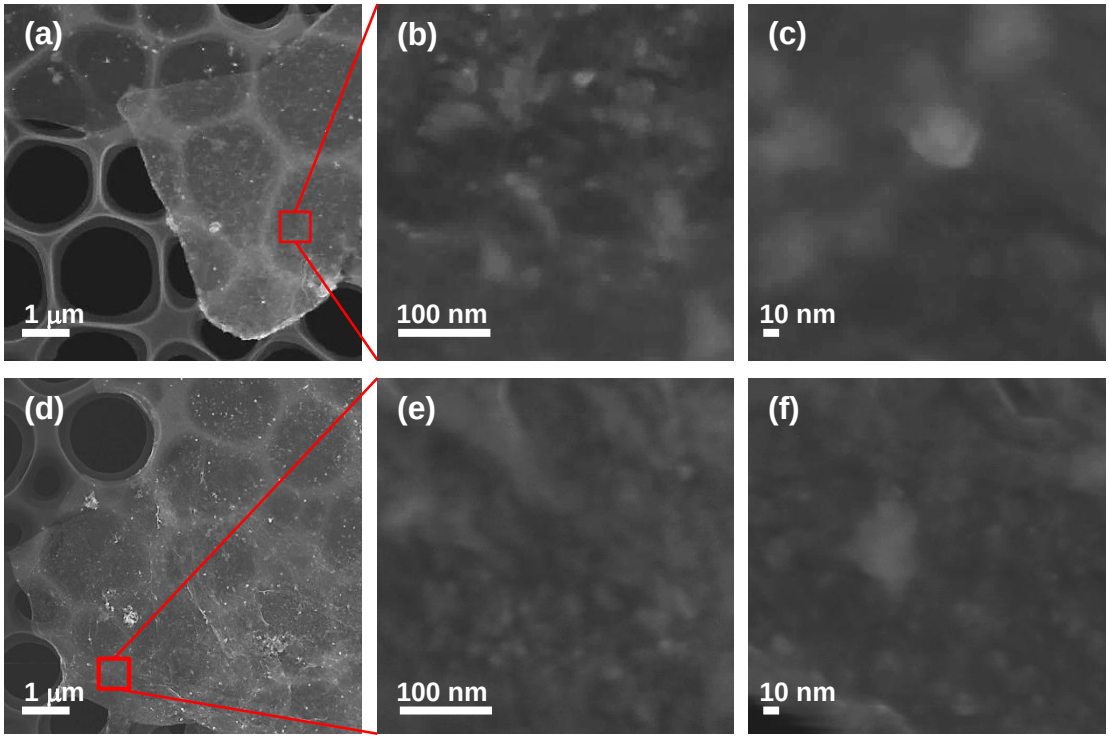

Figure 6.4: Typical FESEM images at different magnifications of uncoated pristine (a–c) and spent (d–f) GO–Fe_3O_4 nanocomposites after long-term stability test.

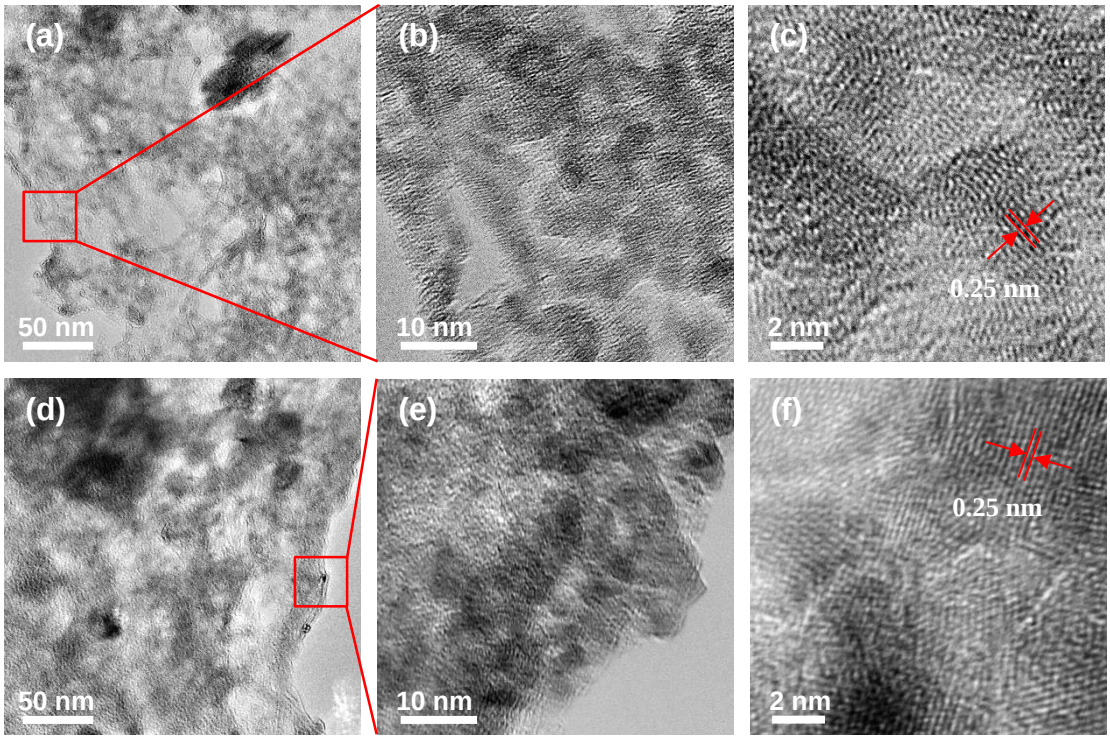

Figure 6.5: HRTEM images at different magnifications of pristine (a-c) and spent (d-f) GO–Fe_3O_4 nanocomposites after long-term stability test.

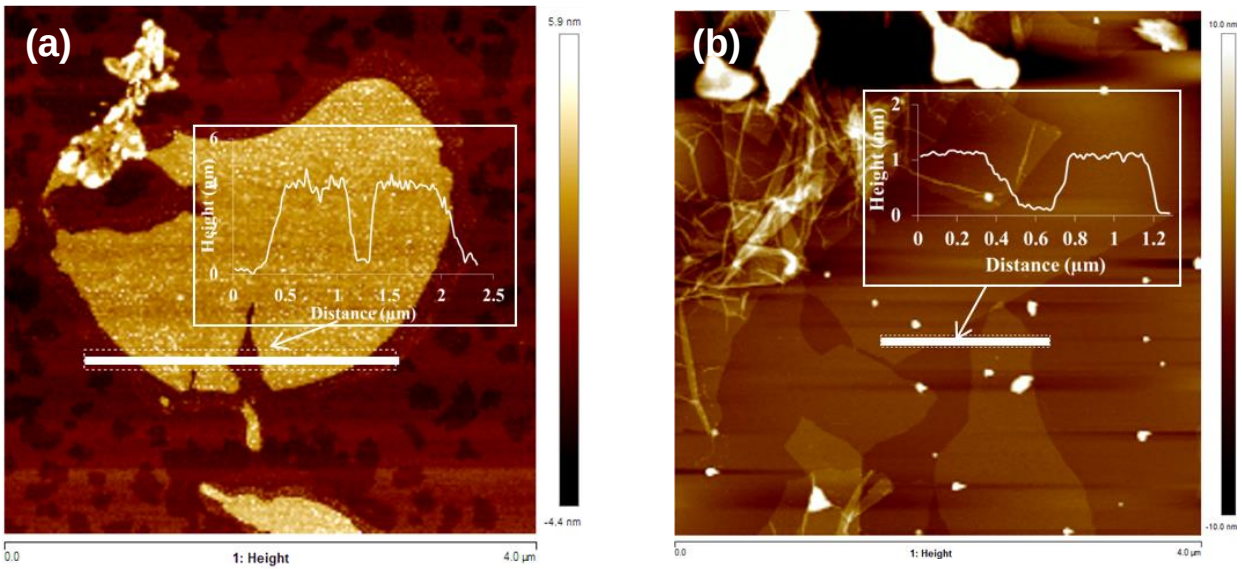

Figure 6.6: AFM images of pristine GO–Fe_3O_4 nanocomposites (a) and GO sheets (b) the on mica surface. The insets show the height profile along the dashed line in the panel of pristine nanocomposites and GO, respectively.

6.3.3 Proposed synergistic interaction mechanism of GO–Fe_3O_4 nanocomposites

The major findings in this chapter on the recyclability and longevity of the GO–Fe_3O_4 nanocomposites as catalyst are novel indeed. In order to explain this major finding, Figure 6.7 shows a schematic of the proposed mechanism related to the synergistic interfacial effect of the GO sheet and iron oxide NPs in delivering the unexpected stabilisation behaviour. In principle, the reaction mainly takes place at the solid-liquid interface, where the actives sites ($\equiv Fe^{2+}/\equiv Fe^{3+}$) of Fe_3O_4 NPs linked to the surface of GO sheets catalytically decomposed the adsorbed H_2O_2 into $HO^{\bullet}$ radicals and hydroperoxyl radicals ($HOO^{\bullet}$) according to Equation 6.1 and 6.2. Instead of just the Fe_3O_4 active sites, H_2O_2 was also being activated and decomposed on the GO surfaces to form $HO^{\bullet}$ radicals [34]. This phenomenon is attributed to the intrinsic donor-acceptor surface properties of carbon materials [13, 17, 35, 36] via an electron transfer reaction similar to the Fenton mechanism, with $GO_{C=Csp2}$ and $GO_{C\text{-}Csp3}$ as the reduced and oxidised carbon actives sites (Equation 6.3 and 6.4). Additionally, GO consists of unpaired π electrons by the presence of many semiconducting π-conjugated sp^2 carbon domains on its basal planes [19-21] which in turn are able to facilitate electron transfer between GO and iron centres [12, 37] via Fe–O–C bonds [14]. This electron transfer could be correlated with the reduction potential of the GO that is about –0.19 V *vs.* saturated calomel electrode (SCE) [38], which is lower than the standard reduction potential of Fe^{3+}/Fe^{2+} (+0.771 V) [13, 39]. Based on this fact, spontaneous reduction of $\equiv Fe^{3+}$ to $\equiv Fe^{2+}$ was conceivable because the electron could be donated from the GO basal planes towards the oxidised active sites. Such synergistic interaction between the GO and Fe_3O_4 NPs is beneficial in accelerating the $\equiv Fe^{3+}/\equiv Fe^{2+}$ redox cycles (Equation 6.5) for the fast reduction of $\equiv Fe^{3+}$ to $\equiv Fe^{2+}$ which is actively participating in the decomposition of adsorbed H_2O_2 into $HO^{\bullet}$ radicals during catalysis, since the reduction of $\equiv Fe^{3+}$ by H_2O_2 to $\equiv Fe^{2+}$ [40] was relatively quite slow. Therefore, the efficient cyclical electron transfer between GO and Fe_3O_4 NPs in the GO–Fe_3O_4 nanocomposites plays a dominant role in altering the surface redox processes which were able to sustain the high removal of AO7 in the heterogeneous Fenton-like reaction.

$$\equiv Fe^{2+} + H_2O_2 \rightarrow \equiv Fe^{3+} + {}^{\bullet}OH + OH^{-} \qquad (6.1)$$

$$\equiv Fe^{3+} + H_2O_2 \rightarrow \equiv Fe^{2+} + HOO^{\bullet} + H^{+} \qquad (6.2)$$

$$GO_{C=Csp^2} + H_2O_2 \rightarrow GO_{C-Csp^3} + {}^{\bullet}OH + OH^{-} \qquad (6.3)$$

$$GO_{C-Csp^3} + H_2O_2 \rightarrow GO_{C=Csp^2} + HOO^{\bullet} + H^{+} \qquad (6.4)$$

$$GO_{C=Csp^2} + \equiv Fe^{3+} \rightarrow GO_{C-Csp^3} + \equiv Fe^{2+} \qquad (6.5)$$

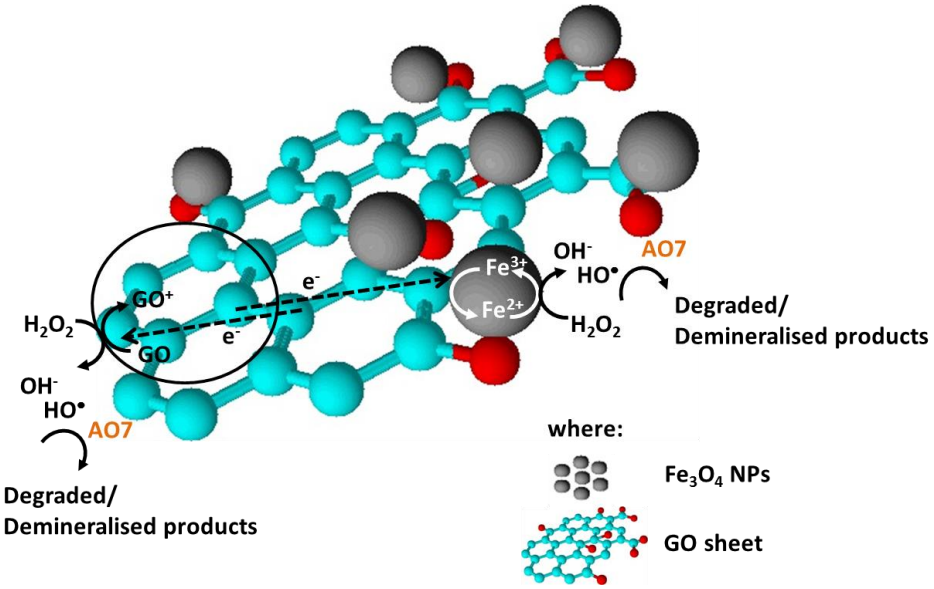

Figure 6.7: Proposed mechanism for degradation of AO7 with GO–Fe_3O_4/ H_2O_2 in heterogeneous Fenton-like reaction.

6.4 Conclusions

The GO–Fe_3O_4 nanocomposites demonstrated superior catalytic activity and stability by sustaining nearly 98% of AO7 removal with insignificant iron leaching over seven consecutive cycles of oxidative degradation compared to the bare Fe_3O_4 NPs. Such enhancement can be attributed to the presence of synergistic interfacial interactions between the GO and Fe_3O_4 NPs during the heterogeneous catalysis. These synergistic interactions can be well explained based on the systematic investigation surface activity of both catalysts at their respective cycles of reaction. Interestingly, GO–Fe_3O_4 nanocomposites were able to preserve its surface activity by keeping its initial Fe^{3+}/Fe^{2+} ratio of 2 and similar morphological features even after undergoing seven cycles of reaction. Meanwhile, Fe_3O_4 NPs exhibited a noteworthy increase in Fe^{3+}/Fe^{2+} ratio from 2.01 up to 3.31. The increase in Fe^{3+}/Fe^{2+} ratio can be ascribed by a proportion of $\equiv Fe^{2+}$ being oxidised into $\equiv Fe^{3+}$ which remained in the latter state due to ineffective regeneration of $\equiv Fe^{2+}$ on the surface of the Fe_3O_4 NPs. Based on these findings, it is postulated that the presence of synergistic interactions between both components in GO–Fe_3O_4 contributes to the conceivable spontaneous reduction of $\equiv Fe^{3+}$ to regenerate $\equiv Fe^{2+}$ due to the intrinsic donor-acceptor surface properties of GO, which facilitates the electron transfer between GO and oxidised active sites ($\equiv Fe^{3+}$) via Fe–O–C bonds. At the same time, GO was found to undergo slight oxidation with 18.71% reduction in the sp^2 carbon domain observed,

possibly from the attack of HO• on the GO planes and also the incomplete recovery of sp^2 carbon domains during the catalysis. In summary, the presence of these synergistic effects in GO–Fe_3O_4 nanocomposites plays a dominant role in accelerating the redox cycles of active sites in the regeneration of $\equiv Fe^{2+}$, which confers the catalyst's superior recyclability and longevity for oxidative degradation of AO7 in the heterogeneous Fenton-like reaction.

References

[1] H. Lim, J. Lee, S. Jin, J. Kim, J. Yoon, T. Hyeon, Highly active heterogeneous Fenton catalyst using iron oxide nanoparticles immobilized in alumina coated mesoporous silica, Chem. Commun. (2006) 463-465.

[2] X. Hu, B. Liu, Y. Deng, H. Chen, S. Luo, C. Sun, P. Yang, S. Yang, Adsorption and heterogeneous Fenton degradation of 17α-methyltestosterone on nano Fe_3O_4/MWCNTs in aqueous solution, Appl. Catal. B 107 (2011) 274-283.

[3] Z. Hua, W. Ma, X. Bai, R. Feng, L. Yu, X. Zhang, Z. Dai, Heterogeneous Fenton degradation of bisphenol A catalyzed by efficient adsorptive Fe_3O_4/GO nanocomposites, Environ. Sci. Pollut. Res. 21 (2014) 7737-7745.

[4] J.H. Ramirez, C.A. Costa, L.M. Madeira, G. Mata, M.A. Vicente, M.L. Rojas-Cervantes, A.J. López-Peinado, R.M. Martín-Aranda, Fenton-like oxidation of orange II solutions using heterogeneous catalysts based on saponite clay, Appl. Catal. B 71 (2007) 44-56.

[5] L. Xu, J. Wang, Magnetic nanoscaled Fe_3O_4/CeO_2 composite as an efficient Fenton-like heterogeneous catalyst for degradation of 4-chlorophenol, Environ. Sci. Technol. 46 (2012) 10145-10153.

[6] V. Cleveland, J.-P. Bingham, E. Kan, Heterogeneous Fenton degradation of bisphenol A by carbon nanotube-supported Fe_3O_4, Sep. Purif. Technol. 133 (2014) 388-395.

[7] S. Navalon, A. Dhakshinamoorthy, M. Alvaro, H. Garcia, Heterogeneous Fenton catalysts based on activated carbon and related materials, ChemSusChem 4 (2011) 1712-1730.

[8] S. Aksel, D. Eder, Catalytic effect of metal oxides on the oxidation resistance in carbon nanotube-inorganic hybrids, J. Mater. Chem. 20 (2010) 9149-9154.

[9] J.H. Ramirez, F.J. Maldonado-Hódar, A.F. Pérez-Cadenas, C. Moreno-Castilla, C.A. Costa, L.M. Madeira, Azo-dye orange II degradation by heterogeneous Fenton-like reaction using carbon-Fe catalysts, Appl. Catal. B 75 (2007) 312-323.

[10] A. Rodriguez, G. Ovejero, J.L. Sotelo, M. Mestanza, J. Garcia, Heterogeneous Fenton catalyst supports screening for mono azo dye degradation in contaminated wastewaters, Ind. Eng. Chem. Res. 49 (2010) 498-505.

[11] J. Chun, H. Lee, S.-H. Lee, S.-W. Hong, J. Lee, C. Lee, J. Lee, Magnetite/mesocellular carbon foam as a magnetically recoverable Fenton catalyst for removal of phenol and arsenic, Chemosphere 89 (2012) 1230 - 1237.

[12] J. Deng, X. Wen, Q. Wang, Solvothermal in situ synthesis of Fe_3O_4-multi-walled carbon nanotubes with enhanced heterogeneous Fenton-like activity, Mater. Res. Bull. 47 (2012) 3369-3376.

[13] S. Song, H. Yang, R. Rao, H. Liu, A. Zhang, High catalytic activity and selectivity for hydroxylation of benzene to phenol over multi-walled carbon nanotubes supported Fe_3O_4 catalyst, Appl. Catal. A 375 (2010) 265-271.

[14] N.A. Zubir, C. Yacou, J. Motuzas, X. Zhang, J. C. Diniz da Costa, Structural and functional investigation of graphene oxide-Fe_3O_4 nanocomposites for the heterogeneous Fenton-like reaction, Sci. Rep. 4 (2014) 4594 1-8.

[15] S. Guo, G. Zhang, Y. Guo, J.C. Yu, Graphene oxide–Fe_2O_3 hybrid material as highly efficient heterogeneous catalyst for degradation of organic contaminants, Carbon 60 (2013) 437-444.

[16] O. Taran, E. Polyanskaya, O. Ogorodnikova, V. Kuznetsov, V. Parmon, M. Besson, C. Descorme, Influence of the morphology and the surface chemistry of carbons on their catalytic performances in the catalytic wet peroxide oxidation of organic contaminants, Appl. Catal. A 387 (2010) 55-66.

[17] C.M. Domínguez, P. Ocón, A. Quintanilla, J.A. Casas, J.J. Rodriguez, Highly efficient application of activated carbon as catalyst for wet peroxide oxidation, Appl. Catal. B 140–141 (2013) 663-670.

[18] W. Baaziz, L. Truong-Phuoc, C. Duong-Viet, G. Melinte, I. Janowska, V. Papaefthimiou, O. Ersen, S. Zafeiratos, D. Begin, S. Begin-Colin, C. Pham-Huu, Few layer graphene decorated with homogeneous magnetic Fe_3O_4 nanoparticles with tunable covering densities, J. Mater. Chem. A 2 (2014) 2690-2700.

[19] Y. Matsumoto, M. Koinuma, S. Ida, S. Hayami, T. Taniguchi, K. Hatakeyama, H. Tateishi, Y. Watanabe, S. Amano, Photoreaction of graphene oxide nanosheets in water, J. Phys. Chem. C 115 (2011) 19280-19286.

[20] K.P. Loh, Q. Bao, G. Eda, M. Chhowalla, Graphene oxide as a chemically tunable platform for optical applications, Nat. Chem. 2 (2010) 1015-1024.

[21] L.M. Pastrana-Martínez, S. Morales-Torres, V. Likodimos, J.L. Figueiredo, J.L. Faria, P. Falaras, A.M.T. Silva, Advanced nanostructured photocatalysts based on reduced graphene oxide–TiO_2 composites for degradation of diphenhydramine pharmaceutical and methyl orange dye, Appl. Catal. B 123–124 (2012) 241-256.

[22] A. Bagri, C. Mattevi, M. Acik, Y.J. Chabal, M. Chhowalla, V.B. Shenoy, Structural evolution during the reduction of chemically derived graphene oxide, Nat. Chem. 2 (2010) 581-587.

[23] G. Liao, S. Chen, X. Quan, H. Yu, H. Zhao, Graphene oxide modified g-C_3N_4 hybrid with enhanced photocatalytic capability under visible light irradiation, J. Mater. Chem. 22 (2012) 2721-2726.

[24] N.A. Zubir, C. Yacou, X. Zhang, J.C. Diniz da Costa, Optimisation of graphene oxide–iron oxide nanocomposite in heterogeneous Fenton-like oxidation of Acid Orange 7, J. Environ. Chem. Eng. 2 (2014) 1881-1888.

[25] A.D. Bokare, R.C. Chikate, C.V. Rode, K.M. Paknikar, Iron-nickel bimetallic nanoparticles for reductive degradation of azo dye orange G in aqueous solution, Appl. Catal. B 79 (2008) 270-278.

[26] X. Xue, K. Hanna, M. Abdelmoula, N. Deng, Adsorption and oxidation of PCP on the surface of magnetite: Kinetic experiments and spectroscopic investigations, Appl. Catal. B 89 (2009) 432-440.

[27] K. Rusevova, F.-D. Kopinke, A. Georgi, Nano-sized magnetic iron oxides as catalysts for heterogeneous Fenton-like reactions—Influence of Fe(II)/Fe(III) ratio on catalytic performance, J. Hazard. Mater. 241–242 (2012) 433-440.

[28] S. Sabhi, J. Kiwi, Degradation of 2,4-dichlorophenol by immobilized iron catalysts, Water Res. 35 (2001) 1994-2002.

[29] C. Yang, G. Wang, Z. Lu, J. Sun, J. Zhuang, W. Yang, Effect of ultrasonic treatment on dispersibility of Fe_3O_4 nanoparticles and synthesis of multi-core Fe_3O_4/SiO_2 core/shell nanoparticles, J. Mater. Chem. 15 (2005) 4252-4257.

[30] S. Tiwari, R. Prakah, R.J. Choudhary, D.M. Phase, Oriented growth of Fe_3O_4 thin film on crystalline and amorphous substrates by pulsed laser deposition, J. Phys. D 40 (2007) 4943-4947.

[31] F.-Y. Ran, Y. Tsunemaru, T. Hasegawa, Y. Takeichi, A. Harasawa, K. Yaji, S. Kim, A. Kakizaki, Angle-resolved photoemission syudy of Fe_3O_4 (001) films across verwey transition, J. Phys. D 45 (2012) 275002-275006.

[32] W. Li, Y. Bai, Y. Zhang, M. Sun, R. Cheng, X. Xu, Y. Chen, Y. Mo, Effect of hydroxyl radical on the structure of multi-walled carbon nanotubes, Synthetic Met. 155 (2005) 509-515.

[33] X. Zhang, L. Lei, B. Xia, Y. Zhang, J. Fu, Oxidization of carbon nanotubes through hydroxyl radical induced by pulsed O_2 plasma and its application for O_2 reduction in electro-Fenton, Electrochim. Acta 54 (2009) 2810-2817.

[34] W. Zhang, C. Wang, Z. Li, Z. Lu, Y. Li, J.-J. Yin, Y.-T. Zhou, X. Gao, Y. Fang, G. Nie, Y. Zhao, Unraveling stress-induced toxicity properties of graphene oxide and the underlying mechanism, Adv. Mater. 24 (2012) 5391-5397.

[35] C.M. Domínguez, A. Quintanilla, P. Ocón, J.A. Casas, J.J. Rodriguez, The use of cyclic voltammetry to assess the activity of carbon materials for hydrogen peroxide decomposition, Carbon 60 (2013) 76-83.

[36] F. Lücking, H. Köser, M. Jank, A. Ritter, Iron powder, graphite and activated carbon as catalysts for the oxidation of 4-chlorophenol with hydrogen peroxide in aqueous solution, Water Res. 32 (1998) 2607-2614.

[37] K. Jasuja, J. Linn, S. Melton, V. Berry, Microwave-reduced uncapped metal nanoparticles on graphene: Tuning catalytic, electrical, and raman properties, J. Phys. Chem. Lett. 1 (2010) 1853-1860.

[38] N. Karousis, A.S.D. Sandanayaka, T. Hasobe, S.P. Economopoulos, E. Sarantopoulou, N. Tagmatarchis, Graphene oxide with covalently linked porphyrin antennae: Synthesis, characterization and photophysical properties, J. Mater. Chem. 21 (2011) 109-117.

[39] S. Song, R. Rao, H. Yang, H. Liu, A. Zhang, Facile synthesis of Fe_3O_4/MWCNTs by spontaneous redox and their catalytic performance, Nanotechnol. 21 (2010) 185602-185607.

[40] E.G. Garrido-Ramírez, B.K.G. Theng, M.L. Mora, Clays and oxide minerals as catalysts and nanocatalysts in Fenton-like reactions — A review, Appl. Clay Sci. 47 (2010) 182-192.

Chapter 7

Physicochemical characterisation and catalytic properties investigation of graphene oxide with zinc partially substituted magnetite ($GO–Fe_{3-x}Zn_xO_4$) nanocomposites

Abstract

In this study, a series of nanocomposites containing graphene oxide and zinc partially substituted magnetite nanoparticles ($GO–Fe_{3-x}Zn_xO_4$, $0 \leq x \leq 0.4$), were synthesised through a facile precipitation-oxidation method. The partial substitution of zinc into the magnetite structure was confirmed by the collective findings of XRD, TG-DTG, XPS and STEM-EDS analysis. This work shows that the GO played a major role by increasing the oxidative degradation of acid orange 7 (AO7) efficiency by ~30% or more attributed to the enhancement of the catalytic activity in the UV-assisted Fenton-like reactions. Interestingly, even the nanocomposites without the photo-luminescent zinc (x=0) as $GO–Fe_3O_4$, also delivered high catalytic activity under UV-assisted conditions as close as the samples containing zinc. Overall, it was found that significant improvements were obtained when GO was incorporated into the nanocomposites as a catalyst support, whilst zinc provided minor changes in the catalytic activity only. The catalytic kinetic activity peaked for x=0.2 samples, which was attributed to the higher sp^2 carbon domains on the GO basal planes that were responsible for the transfer of electrons from the GO to the zinc partially substituted magnetite nanoparticles.

7.1 Introduction

Growing research interest has been paid to the heterogeneous Fenton-like reaction for the degradation of persistent organic compounds using GO supported iron oxide nanocomposites, mainly due to their high surface area and decent catalytic properties [1-5]. Compared to other types of iron oxide, magnetite (Fe_3O_4) offers higher catalytic activity with several interesting structural features [6, 7]. First, the presence of Fe^{2+} occupying the octahedral site of Fe_3O_4 plays a key role as an electron donor

to initiate decomposition of hydrogen peroxide (H_2O_2) into hydroxyl radicals ($HO^{\bullet}$) following the Haber–Weiss mechanism [7, 8]. Second, magnetite accommodates both Fe^{2+} and Fe^{3+} on the octahedral sites, allowing the Fe species to be reversibly oxidised and reduced while keeping the structure unchanged [7]. Third, the Fe cations in the Fe_3O_4 structure can be isomorphically substituted with different types of transition metal cations which can significantly affect the microstructure, physicochemical properties and catalytic activity of the resulting materials [9-11].

Moreover, recent studies have revealed that the isomorphic substitution of Fe_3O_4 with Co [12, 13], Mn [9, 14], Ti [15, 16], Cr [17] , V[15, 18] have significantly enhanced its catalytic activity in various reactions. The exception is the substitution of Fe_3O_4 with Ni [7, 19], which led to a decrease in catalytic activity as Ni^{2+} were mainly substituted with Fe^{2+} within the structure of Fe_3O_4. These variations were greatly dependent on the types of substituting metals, it's concentration as well as the occupancy of substitution sites which stimulates an effective generation of $HO^{\bullet}$ radicals during catalysis. With respect to this strategy, it is postulated that GO also plays a synergistic role in the UV-assisted Fenton-like reaction when coupled with the heterogeneous Fenton-like catalyst (e.g. magnetite) and the photoluminescence catalyst (zinc oxide). Therefore, this work investigates the influence of GO coupled with Fe_3O_4 and zinc oxide for the oxidative degradation of persistent organic compounds which remains unaddressed in the open literature.

This work shows for the first time the investigation of a series of zinc partially substituted magnetite nanoparticles (NPs) with different concentrations being immobilised onto graphene oxide sheets as GO–$Fe_{3-x}Zn_xO_4$ nanocomposites. Of particular interest, the effect of zinc on the physicochemical and catalytic properties of GO–$Fe_{3-x}Zn_xO_4$ nanocomposites were systematically investigated by varying the zinc molar ratio $0 \leq x \leq 0.4$. The catalytic performances of GO–$Fe_{3-x}Zn_xO_4$ nanocomposites were evaluated using a model reaction of AO7 oxidative degradation in the heterogeneous and UV-assisted Fenton-like reactions.

7.2 Experimental

7.2.1 Materials

$FeCl_3{\cdot}6H_2O$ (97%), $FeCl_2{\cdot}4H_2O$ (99%), $Zn(NO_3)_2{\cdot}6H_2O$ (98%), NH_4OH (30 wt% NH_3), H_2O_2 (30%, w/w) and AO7 (Orange II; 85%) were purchased from Sigma-Aldrich. All chemicals were of analytical grade and used as received except for graphite oxide which was prepared from graphite flakes (Sigma Aldrich) by the modified Hummer's method [20, 21].

7.2.2 Synthesis of GO–zinc partially substituted magnetite (GO–$Fe_{3-x}Zn_xO_4$) nanocomposites and zinc partially substituted magnetite ($Fe_{3-x}Zn_xO_4$) NPs.

A series of GO–$Fe_{3-x}Zn_xO_4$ nanocomposites with a zinc molar ratio (x) ranging from 0 to 0.4 were synthesised through a precipitation-oxidation method [17, 22, 23] in the presence of graphene oxide (GO). The x values were calculated based on the assumption that the amount of zinc being partially substituted into magnetite (Fe_3O_4) corresponded to the molar ratio of Zn^{2+} to Fe^{2+} salt solutions used in the synthesis method. For instance, by taking into account the GO–$Fe_{3-x}Zn_xO_4$ with x=0.2, the typical synthesis route is described as follows. Briefly, 62 mL of graphite oxide suspension (0.85 mg mL^{-1}) was exfoliated under ultrasonication for 1 h to obtain an aqueous dispersion of GO. Then, 8.64 mmol of $FeCl_3{\cdot}6H_2O$, 4.32 mmol of $FeCl_2{\cdot}4H_2O$ and 0.86 mmol of $Zn(NO_3)_2{\cdot}6H_2O$ were dissolved in 200 mL deionised water. After stirring for 30 min, this solution was heated to 90 °C. At this stage, NH_4OH solution was added dropwise into the heated solution until pH 4 was reached under constant stirring. This was followed by the gradual addition of GO suspension into the heated mixture and continuously stirred for another 30 min until homogeneously mixed.

Subsequently, an appropriate amount of NH_4OH solution was continuously added dropwise into the mixture until the pH reached a value of 11. The mixture was cooled to room temperature after being aged for 1 h at 90 °C under constant stirring. The resulting black precipitate was magnetically separated and washed three times with deionised water and ethanol and then dried at 60 °C for 48 h. For comparison, the same procedure was employed to synthesise zinc partially substituted magnetite NPs ($Fe_{3-x}Zn_xO_4$) with different zinc molar ratios (x=0, 0.1, 0.2, 0.4) in the absence of GO solution.

7.2.3 Characterisation

The textural properties of the resultant samples were characterised by nitrogen sorption using a Tristar II 3020 (Micromeritics). The specific surface area and pore volume were determined using Brunauer-Emmett-Teller (BET) equation and the single point method. The pore size distribution curves were calculated using non-local density functional theory (NLDFT), from the desorption branch of the isotherms. The XRD patterns of nanocomposites were obtained using X-ray diffraction by a Bruker D8 Advance diffractometer at 40 kV, 40 mA and step size of 0.02° using a filtered Cu Kα radiation (λ = 1.5418 Å). Thermogravimetric analysis was performed on a TGA-DSC 1 Thermogravimetric Analyser (Mettler Toledo). The analysis was carried out by heating the samples from 30 to 800 °C at a heating rate of 10 °C min^{-1} under nitrogen atmosphere at a flow rate of 60 mL min^{-1}. Surface analysis was performed on a Kratos Axis ULTRA X-ray photoelectron spectrometer (XPS) equipped with monochromatic Al Kα (hν = 1486.6 eV) radiation. The curve fitting was performed using a

Gaussian–Lorentz peak shape and Shirley background function. The binding energy was calibrated versus the carbon signal at 284.6 eV. The high resolution transmission electron microscopy (HRTEM) and scanning transmission electron microscope-energy dispersive X-ray spectrometer (STEM-EDS) elemental mappings were performed on JOEL 2010 operating at 200 kV, equipped with an energy dispersive X-ray (EDS) detector. Samples were prepared by placing a drop of diluted sample dispersion in ethanol onto a carbon-coated copper grid and air-dried prior to examination.

7.2.4 Catalytic activity measurements

The influence of zinc on the catalytic activity of GO–$Fe_{3-x}Zn_xO_4$ nanocomposites and $Fe_{3-x}Zn_xO_4$ NPs were tested in the heterogeneous and UV-assisted Fenton-like reaction for the oxidative degradation of AO7. In brief, a similar procedure and reaction conditions (0.2 g L^{-1} of catalyst, initial pH of 3, 22 mM of H_2O_2 concentration and 35 mg L^{-1} AO7 at 25 °C) were employed in the heterogeneous Fenton-like reaction as described in our previous work (see Chapter 5) [3]. For the UV-assisted Fenton-like reaction, the experiments were performed by using a custom made photocatalysis set-up equipped with 4 × 8W UV-A lamps (Sylvania Blacklite F8 W/BL350, $330<\lambda<370$ nm) [24]. A 200 mL quartz tube was placed in the centre of the set-up, which was surrounded by the 4 UV-A lamps fitted to the wall of cylindrical lead-line chamber in concentric arrangement. The distance of quartz tube was fixed at 10 cm from the UV lamps. In a typical experiment, 20 mg of nanocomposites and/or NPs were added into the quartz tube consisting of 100 mL of 35 mg L^{-1} AO7 at initial pH solution of 3. The mixed suspension was kept under constant air bubbling for 30 min of dark adsorption. The reaction was initiated by turning on the UV lamps after the addition of H_2O_2 (22 mM) into the suspension. Sampling was carried out periodically at selected time intervals. The collected suspension was then filtered through 0.22 μm Milipore syringe filters and immediately analysed. The concentration of AO7 was analysed by Evolution 220 UV–Vis spectrophotometer (Thermo Fisher Scientific) at λ_{max} 484 nm.

7.3 Characterisation Results

7.3.1 Nitrogen sorption

The textural properties of the synthesised samples were investigated using nitrogen sorption analysis and results are shown in Figure 7.1. The nitrogen adsorption–desorption isotherms for the $Fe_{3-x}Zn_xO_4$ NPs (Figure 7.1a) are of type IV with H2 hysteresis, indicating the formation of mesoporous materials. Noticeable changes in the hysteresis loops of $Fe_{3-x}Zn_xO_4$ NPs are observed once the zinc molar ratio (x) increases from 0.1 to 0.4, accompanied by the reduction of the total volume. The low

x (0 and 0.1) are characterised by narrow hysteresis starting at P/P_o= 0.6. This shape broadens for x=0.2 and 0.4 whilst the hysteresis starting points are P/P_o= 0.5 and 0.4, respectively. Although these changes in morphology are related to a reduction in interparticle voids, these materials are essentially mesoporous. This is further verified by the pore size distributions in Figure 7.1b, clearly indicating the broadness of the pore size distribution reduces as the zinc molar ratio increases.

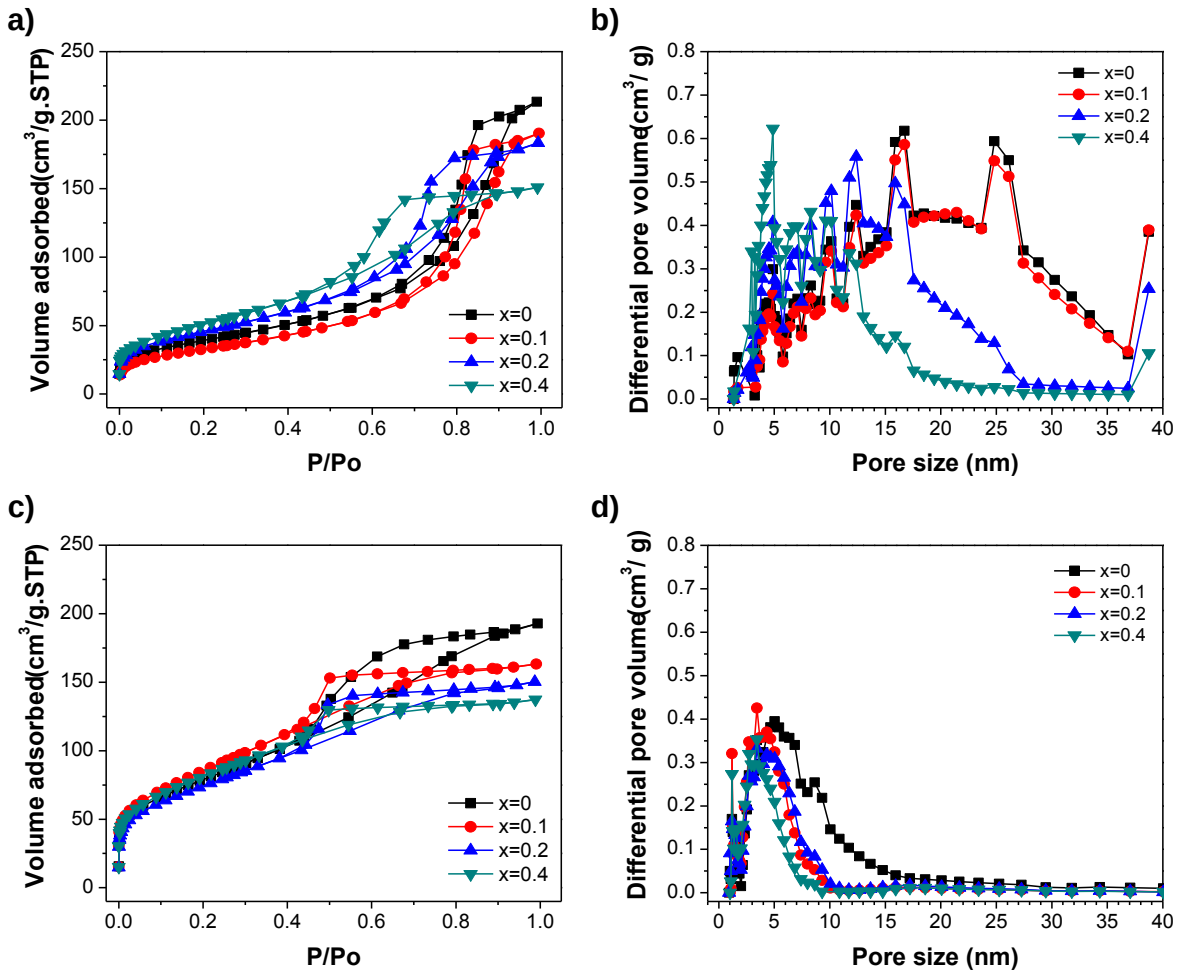

Figure 7.1: Nitrogen adsorption-desorption isotherms and pore size distributions of $Fe_{3-x}Zn_xO_4$ NPs (a, b) and GO–$Fe_{3-x}Zn_xO_4$ nanocomposites (c, d) at different zinc molar ratios (x).

The nitrogen adsorption–desorption isotherms for the GO–$Fe_{3-x}Zn_xO_4$ nanocomposites (Figure 7.1c) are also type IV with H2 hysteresis. However, the hysteresis loops for all samples start at $P/P_o < 0.4$. These results strongly suggest that once the $Fe_{3-x}Zn_xO_4$ NPs were immobilised onto GO sheets, their morphology changes as compared to the morphology of the NPs in Figure 7.1a. In fact, the GO–$Fe_{3-x}Zn_xO_4$ nanocomposites consisted of more uniform and narrower pore size distributions within the range of 1–10 nm (Figure 7.1d). The addition of GO and in-situ growth of $Fe_{3-x}Zn_xO_4$ NPs onto the GO sheets during the synthesis induced a reconstruction of the porous structure in GO–$Fe_{3-x}Zn_xO_4$ nanocomposites increasing the microporosity, based on the volumes adsorbed at

relative pressures below 0.2. This can be explained by the integration of a high aspect ratio two-dimensional (GO sheets) and zero-dimensional (NPs) structures into a single material [2, 25].

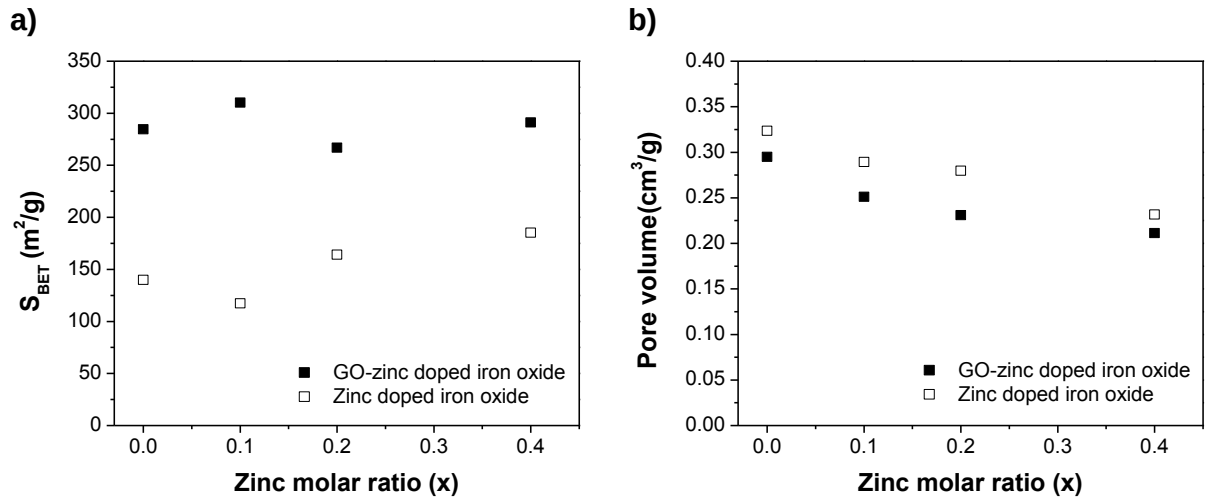

Figure 7.2: BET surface area (a) and pore volume (b) of $Fe_{3-x}Zn_xO_4$ NPs and GO–$Fe_{3-x}Zn_xO_4$ nanocomposites.

These results can be further supported by the greater than 58% increase in the specific surface area (see Figure 7.2a) of the GO–$Fe_{3-x}Zn_xO_4$ nanocomposites (270–310 m^2 g^{-1}) compared to the $Fe_{3-x}Zn_xO_4$ NPs (117–185 m^2 g^{-1}) which can be associated with the intercalation of GO within the NPs. The effect of the zinc was only observed for $Fe_{3-x}Zn_xO_4$ NPs as the specific area increased by nearly 30% as zinc molar ratio (x) was varied from 0 to 0.4, though there were no appreciable differences in the specific area of GO–$Fe_{3-x}Zn_xO_4$ nanocomposites. The pore volumes for both samples (Figure 7.2b) slightly decreased from 0.32 to 0.23 cm^3 g^{-1} and 0.29 to 0.21 cm^3 g^{-1} in the $Fe_{3-x}Zn_xO_4$ NPs and GO–$Fe_{3-x}Zn_xO_4$ nanocomposites, respectively. Hence, increasing the amount of zinc led to dense structures.

7.3.2 XRD

The XRD patterns of $Fe_{3-x}Zn_xO_4$ NPs and GO–$Fe_{3-x}Zn_xO_4$ nanocomposites are displayed in Figure 7.3a and b, respectively. The diffraction peaks of $Fe_{3-x}Zn_xO_4$ and GO–$Fe_{3-x}Zn_xO_4$ were approximately similar in both samples without zinc (x=0). The diffraction peaks at the 2θ values of ca. 30.2°, 35.6°, 43.3°, 53.6°, 57.4° and 63.1° were assigned to the (220), (311), (400), (422), (511) and (440) crystal planes of Fe_3O_4 with spinel structure (JCPDS No. 19-0629). A slight peak shift of (311) planes towards lower angle were observed (Figure 7.3a, b) with increasing the x values up to 0.4, thus suggesting variations in the resultant crystal structure possibly due to the effect of zinc partial

substitution into the Fe_3O_4 spinel structure. Moreover, there was no visible secondary phase or impurity peaks, thus clearly confirming that zinc was isomorphically substituted into the Fe_3O_4 crystal structure. These results are in good agreement with reports elsewhere by Pati et al. [22] and Byrne et al. [26].

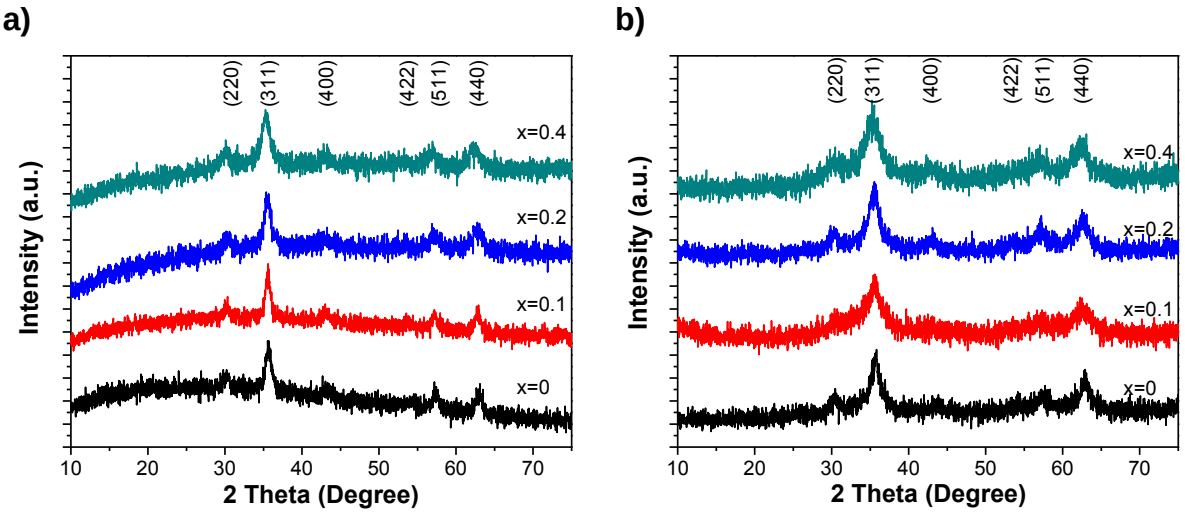

Figure 7.3: XRD pattern of $Fe_{3-x}Zn_xO_4$ NPs (a) and GO–$Fe_{3-x}Zn_xO_4$ nanocomposites (b) at different zinc molar ratio (x).

The crystal domain characteristics of (311) planes of both samples were summarised in Table 7.1. The crystallite size of the samples reduces with increasing the zinc molar ratio (x) from 0 to 0.4. Whereas a slight expansion in the interplanar spacing of (311) planes were found from 0.2519 to 0.2544 nm. These findings are attributed to a slight alteration in the spinel structural framework due to the difference in ionic radius between iron (Fe^{2+}, 0.645 Å and Fe^{3+}, 0.64Å) [12, 16] and zinc (Zn^{2+}, 0.74Å) [22, 27] cations. However, it is interesting that the crystallite size calculated according to Scherrer's equation shows that by increasing the zinc molar ratio, the crystallite size reduces by 30% (10.08 to 6.99 nm) for $Fe_{3-x}Zn_xO_4$ NPs and by 40% (7.39 to 4.43 nm) for GO–$Fe_{3-x}Zn_xO_4$ nanocomposites. In addition, the GO containing samples also conferred ~32% smaller crystallite sizes than non-GO samples, excluding a large variation of 56% for x=0.1.

Table 7.1: Crystal domain characteristics of $Fe_{3-x}Zn_xO_4$ NPs and GO–$Fe_{3-x}Zn_xO_4$ nanocomposites

Samples	**$2\theta_{(311)plane}$ (degree)**	**$d_{spacing}$ (nm)**	**Crystallite size (nm)**
$Fe_{3-x}Zn_xO_4$, x=0	35.64	0.2519	10.08
$Fe_{3-x}Zn_xO_4$, x=0.1	35.57	0.2524	11.71
$Fe_{3-x}Zn_xO_4$, x=0.2	35.53	0.2526	8.34
$Fe_{3-x}Zn_xO_4$, x=0.4	35.31	0.2543	6.99
GO–$Fe_{3-x}Zn_xO_4$, x=0	35.63	0.2519	7.39
GO–$Fe_{3-x}Zn_xO_4$, x=0.1	35.45	0.2531	5.16
GO–$Fe_{3-x}Zn_xO_4$, x=0.2	35.46	0.2529	5.73
GO–$Fe_{3-x}Zn_xO_4$, x=0.4	35.30	0.2544	4.43

7.3.3 Thermogravimetric analysis

Figure 7.4 presents the thermogravimetric-differential thermogravimetric (TG-DTG) curves of $Fe_{3-x}Zn_xO_4$ NPs and GO–$Fe_{3-x}Zn_xO_4$ nanocomposites in nitrogen atmosphere. Two mass loss patterns were observed within 30–150 °C and 150–400 °C for $Fe_{3-x}Zn_xO_4$ NPs (Figure 7.4a). The former pattern is associated with the dehydration of physisorbed water on the surface of NPs, while the latter is assigned to the dehydroxylation of surface hydroxyl groups. The mass loss in the dehydroxylation process increases from 1.9 to 3.0% as the zinc molar ratio (x) increases from 0 to 0.4. This observation corresponds well with the gradual increase in the dehydroxylation temperature as shown by the respective DTG curves. The dehydroxylation temperature was found to be at 251, 271, 273 and 282 °C for x values of 0, 0.1, 0.2 and 0.4, respectively. The presence of surface hydroxyl groups were mainly derived from the dissociation of the water molecules adsorbed on the oxygen defect sites which can be correlated with the isomorphic partial substitution of zinc into the Fe_3O_4 structure [15, 18, 28]. These surface hydroxyl groups can significantly influence the surface properties of materials [10, 16] and adsorption of pollutants within the vicinity of the active sites during catalysis [29].

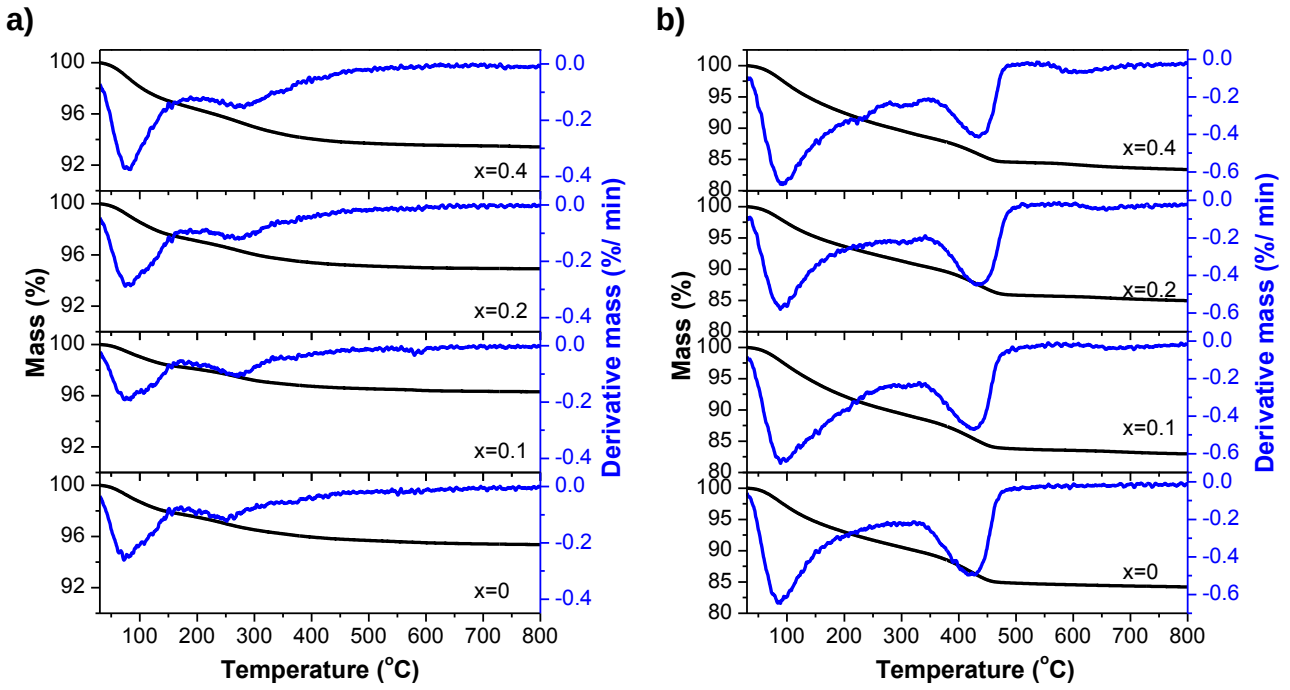

Figure 7.4: The TG and DTG curves of $Fe_{3-x}Zn_xO_4$ NPs (a) and GO–$Fe_{3-x}Zn_xO_4$ nanocomposites (b) under nitrogen atmosphere at different dopant molar ratio (x)

Interestingly, the DTG curve of GO–$Fe_{3-x}Zn_xO_4$ nanocomposites (Figure 7.4b) did not exhibit such a distinct peak of hydroxylation temperature within 150–400 °C at zinc molar ratio (x) of less than 0.2. A weak peak of higher hydroxylation temperature ~315 °C was only observed at x value of 0.4. Such behaviour is attributed to the plausible stabilisation of GO–$Fe_{3-x}Zn_xO_4$ nanocomposites due to the strong interaction [30] between the oxygenated functional groups of GO and $Fe_{3-x}Zn_xO_4$ NPs. This stabilisation can be further substantiated with the higher temperature required for the decomposition of GO from 426 to 443 °C with increasing zinc molar ratio (x).

7.3.4 XPS

The synthesised GO–$Fe_{3-x}Zn_xO_4$ nanocomposites were further examined by XPS analysis. The wide scan spectra of the nanocomposites (Figure 7.5a, except x=0) confirm the presence of Zn 2p photoelectron peaks at binding energy of 1020 eV. As shown in Figure 7.5b, the spin-orbit doublet centred at 1021.7 and 1044.8 eV corresponded to the Zn $2p_{3/2}$ and Zn $2p_{1/2}$, respectively. The observed spin-orbit splitting between these two peaks was about 23 eV. These findings are in agreement with those reported values of Zn^{2+} state [27, 31-33].

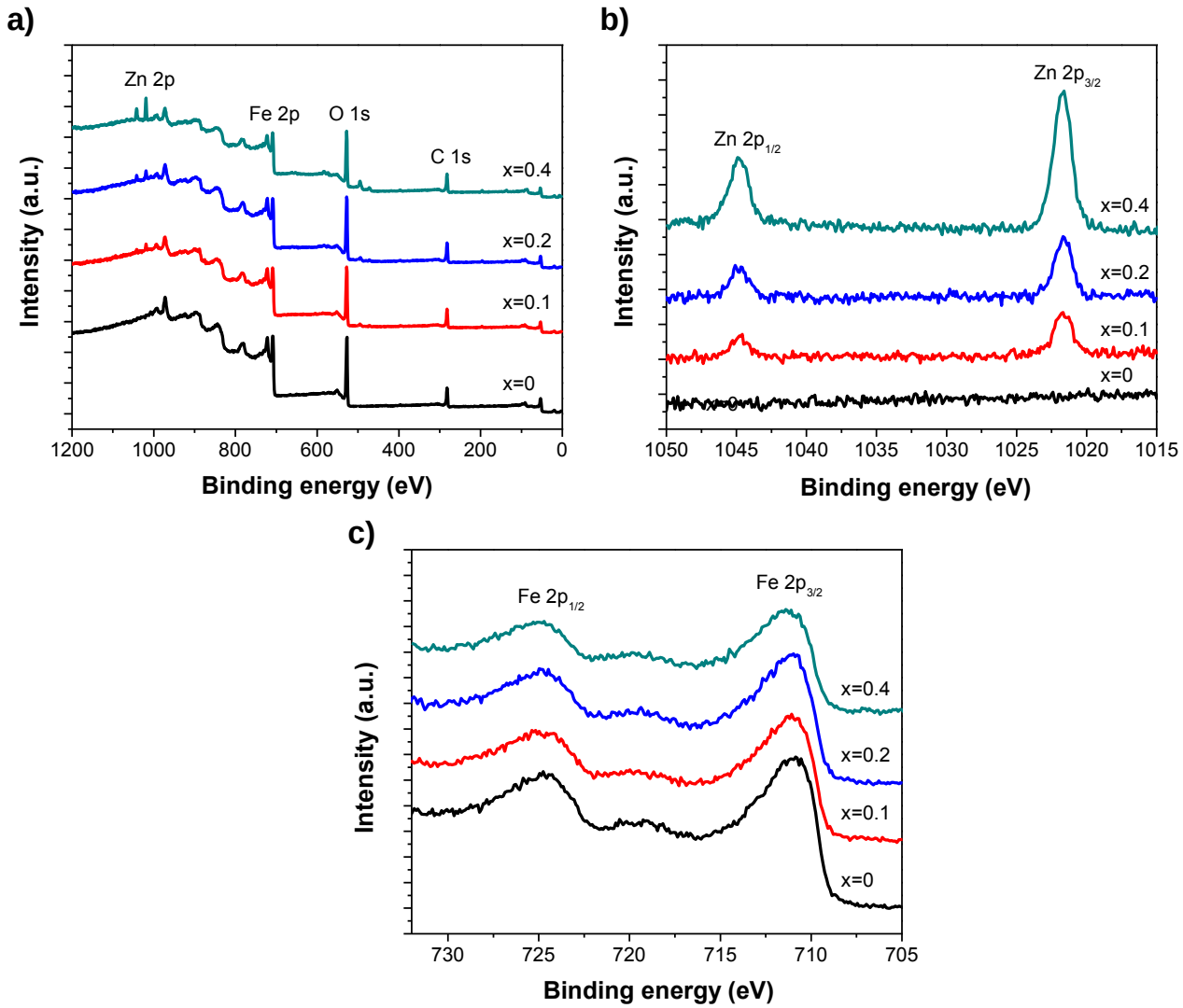

Figure 7.5: Wide scan XPS spectra (a), high resolution spectra of Zn 2p (b) and Fe 2p (c) of GO–$Fe_{3-x}Zn_xO_4$ nanocomposites at different zinc molar ratio (x).

The photoelectron peaks at 711.1 and 724.6 eV in the high resolution Fe 2p scan (Figure 7.5c) were attributed to Fe $2p_{3/2}$ and Fe $2p_{1/2}$ of Fe_3O_4 [2, 34, 35]. The peak of Fe $2p_{3/2}$ shift towards higher binding energy from 711.1 to 711.9 eV and became less intense with the increase in zinc molar ratio (x). These differences can be explained by the plausible changes in the electronic state of Fe and the Fe–O bond after zinc was partially substituted into Fe_3O_4. A similar observation was also reported by Amrousse et al. [12] based on the effect of Co substitution into Fe_3O_4 NPs.

The incorporation of zinc has slightly decreased the relative intensity of Fe–O peak as shown in O 1s spectra (Figure 7.6a). Further decreases in the relative intensity of Fe–O peak at higher zinc molar ratio (x) of more than 0.2 were also noted, which corresponds to nearly 15.9% reduction in its atomic concentration as the x values increased from 0.2 to 0.4. A similar finding was observed with the decrease in the relative intensity of C=C peak (Figure 7.6b), resulting in 11.7% reduction of the sp^2

carbon domain. This can be ascribed to the effect of zinc partial substitution into the Fe_3O_4 structure which may affect the chemical interaction between the $Fe_{3-x}Zn_xO_4$ NPs and GO.

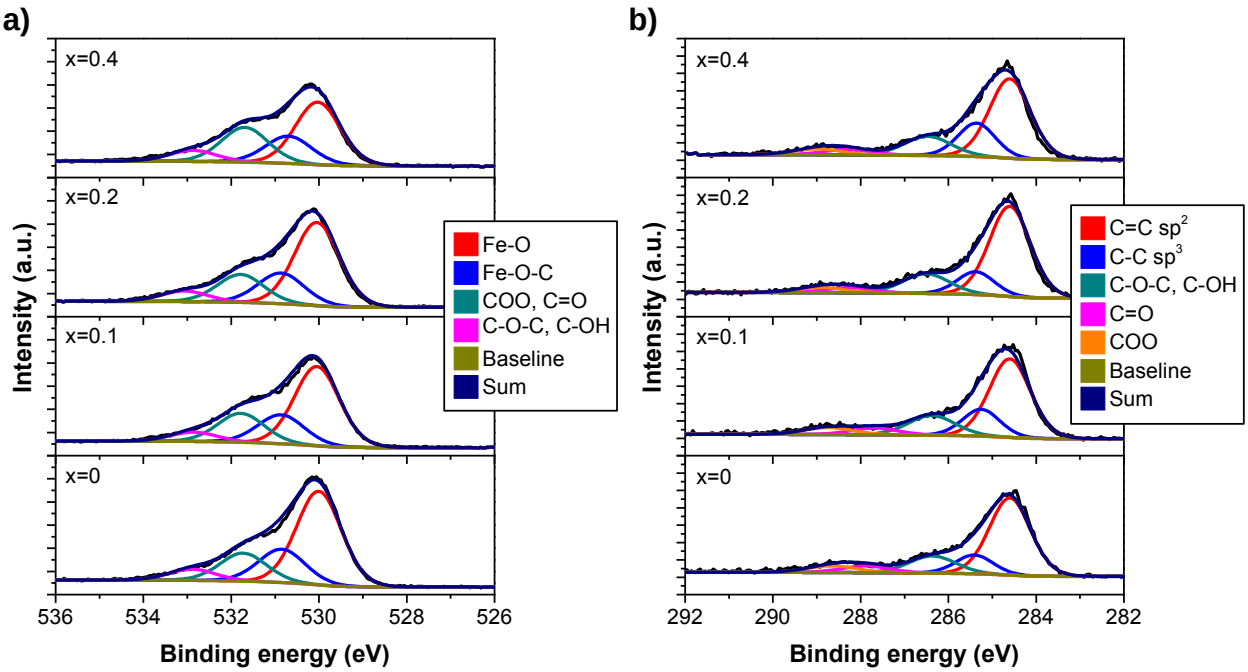

Figure 7.6: XPS curve fit of O 1s (a) and C 1s (b) spectra of GO–$Fe_{3-x}Zn_xO_4$ nanocomposites at different dopant molar ratio (x).

The area of the deconvoluted peaks in Figure 7.6 were determined by a CasaXPS software to calculate the concentration of carbon bound to carbon (C–C) as total of sp^2 and sp^3 carbon domain, and the oxygenated functional groups of carbon bound to oxygen (C–O) as a total of C–O–C, C–OH,C=O and COO. The results are listed in Table 7.2, which shows that the C–C/ C–O ratio peaks at 3.2 for x=0.2.

Table 7.2: Deconvolution results of C 1s spectra for GO and GO–$Fe_{3-x}Zn_xO_4$ nanocomposites.

Group	Relative concentration of functional groups (At. %)					Carbon bound to carbon (C–C)	Carbon bound to oxygen (C–O)	(C–C)/ (C–O)
	C=C sp^2	C–C sp^3	C–O–C, C–O–H	C=O	COO			
Binding energy (eV)	284.6	285.1–285.4	286.4–285.8	287.9–288.2	288.7–289.0	—	—	—
GO	48.1	2.5	42.1	5.1	2.2	50.7	49.3	1.0
GO–$Fe_{3-x}Zn_xO_4$, x=0	59.7	13.2	15.1	5.9	6.1	73.0	27.1	2.7
GO–$Fe_{3-x}Zn_xO_4$, x=0.1	55.7	17.3	15.8	5.4	5.8	72.9	27.1	2.7
GO–$Fe_{3-x}Zn_xO_4$, x=0.2	62.1	14.3	15.4	4.1	4.2	76.3	23.7	3.2
GO–$Fe_{3-x}Zn_xO_4$, x=0.4	54.8	21.0	15.1	4.4	4.8	75.8	24.2	3.1

7.3.5 HRTEM and STEM-EDS

Figure 7.7 shows the HRTEM images of the GO–$Fe_{3-x}Zn_xO_4$ nanocomposites. There were no significant differences in the morphology in both nanocomposites with x=0 and x=0.2. It was found that large amounts of Fe_3O_4 and $Fe_{3-x}Zn_xO_4$ NPs were dispersed throughout the surface of GO sheets (Figure 7.7a and c). From the magnified images indicated in Figure 7.7b and d, high density of roughly spherical NPs with diameters of about 10–15 nm were observed to be anchored on GO sheets. Furthermore, the inset HRTEM images revealed that the interplanar spacing of the lattice fringes was 0.25 nm that corresponded well to the (311) planes of both Fe_3O_4 and $Fe_{3-x}Zn_xO_4$. These findings are in agreement with the previous XRD analysis.

The presence of zinc in the nanocomposites were examined by STEM-EDS elemental mapping. As displayed in Figure 7.8a–c and e–g, the elements of Fe and O were detected and dispersed throughout the surface of both nanocomposite matrices, while the zinc was only observed as white dots in Figure 7.8h (GO–$Fe_{3-x}Zn_xO_4$, x=0.2) but not in Figure 7.8d (GO–$Fe_{3-x}Zn_xO_4$, x=0). Thus, these results further confirm the presence of zinc in GO-$Fe_{3-x}Zn_xO_4$ nanocomposites, which are in accordance with the above TEM observations.

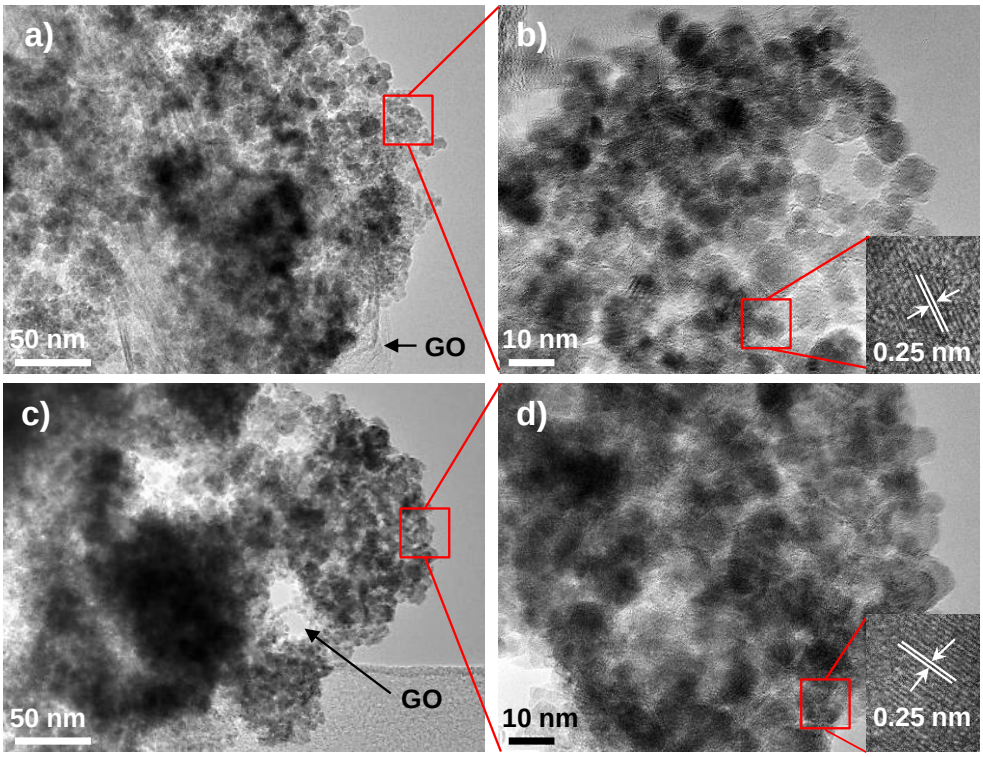

Figure 7.7: HRTEM images of GO–$Fe_{3-x}Zn_xO_4$ nanocomposites at x=0 (a, c) and x=0.2 (c, d).

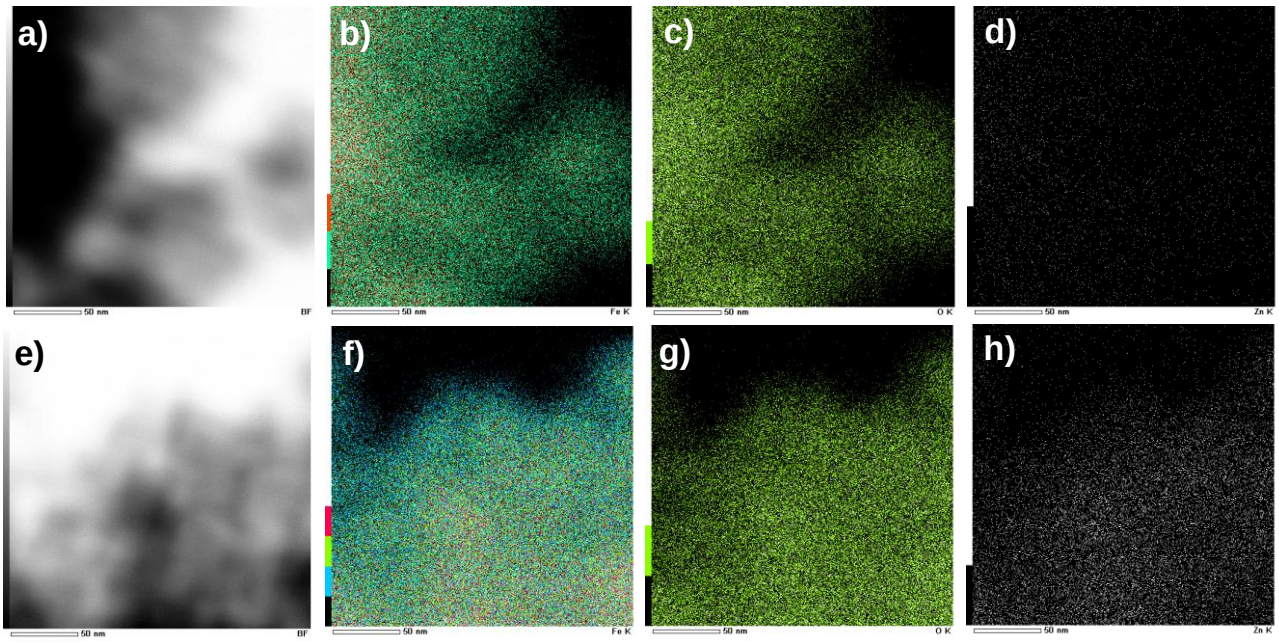

Figure 7.8: STEM images of GO–$Fe_{3-x}Zn_xO_4$ nanocomposites at x=0 (a) and x=0.2 (e) with their corresponding EDS elemental mapping of Fe (b, f), O (c, g) and Zn (d, h).

7.4 Catalytic activity results

Oxidative degradation of AO7 in the presence of H_2O_2 was used as a model system to quantitatively evaluate the catalytic activity of the synthesised samples. Initially, the samples were analysed for the heterogeneous Fenton-like reaction in order to investigate whether the partial substitution of zinc was beneficial or detrimental towards the oxidative degradation of AO7. Figure 7.9 shows the removal efficiency of AO7 as a function of the zinc molar ratio (x). These results clearly indicated that altering the amount of zinc in the $Fe_{3-x}Zn_xO_4$ NPs did not affect their catalytic activity, which remained constant at ~30% (±2%) as the x values varied from 0 to 0.4.

On the other hand, a pronounced increase in the catalytic performance was observed when GO is incorporated as a catalyst support, forming the GO–$Fe_{3-x}Zn_xO_4$ nanocomposites. The removal efficiency of AO7 increased from 50% at x=0 and peaked at 72% for x=0.2. However, a decline in removal efficiency to ~52% was observed at an excess zinc molar ratio of x=0.4, which is similar to the samples without zinc (x=0). Nevertheless, the enhancement of the catalytic performance is clearly attributed to the effect of GO.

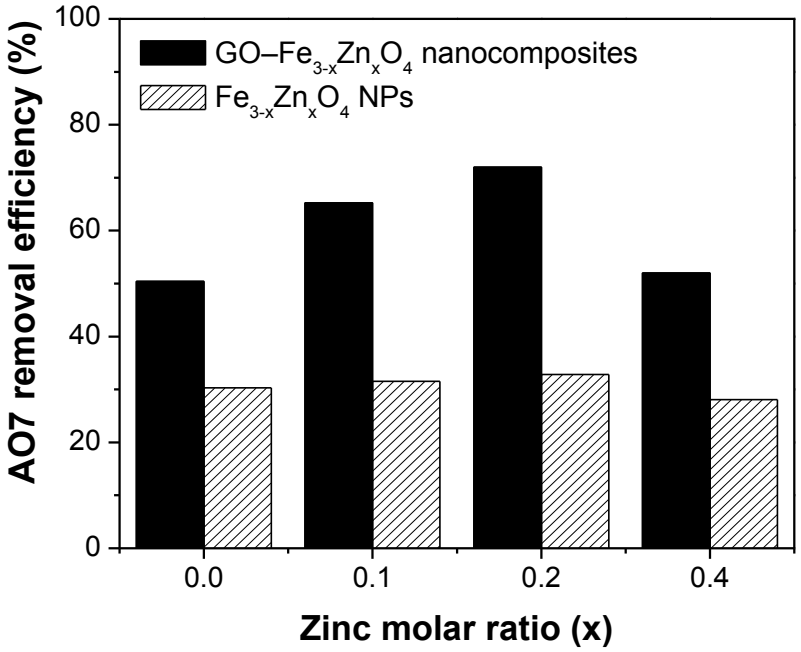

Figure 7.9: The AO7 removal efficiency by GO–$Fe_{3-x}Zn_xO_4$ nanocomposites and $Fe_{3-x}Zn_xO_4$ NPs at different zinc molar ratio (x) in the heterogeneous Fenton-like. Experimental conditions: AO7 35 mg L^{-1}, H_2O_2 22 mM, catalyst 0.2 g L^{-1}, T = 25 °C, pH 3 and 180 min of reaction, which were the optimised conditions as per Chapter 5.

Further evaluation on the catalytic performance of the nanocomposites were performed in the UV-assisted heterogeneous Fenton-like reaction, particularly to test the hypothesis of the partial substitution of zinc into Fe_3O_4 structure to promote improvements in the catalytic activity. The results in Figure 7.10 show a completely different set of values for the samples with and without GO. First, the UV-assisted reaction was positive as it increased the catalytic activity for the $Fe_{3-x}Zn_xO_4$ NPs by comparing Figures 7.9 and 7.10. For instance, AO7 degradation improved from ~30% at 180 min to 47% and 52% at 90 min for x=0 and x=0.2, respectively. The overall improvement of the AO7 degradation is modest at 5% (from 47 to 52%), though it proves that zinc has slightly improved the catalytic activity of the resultant NPs.

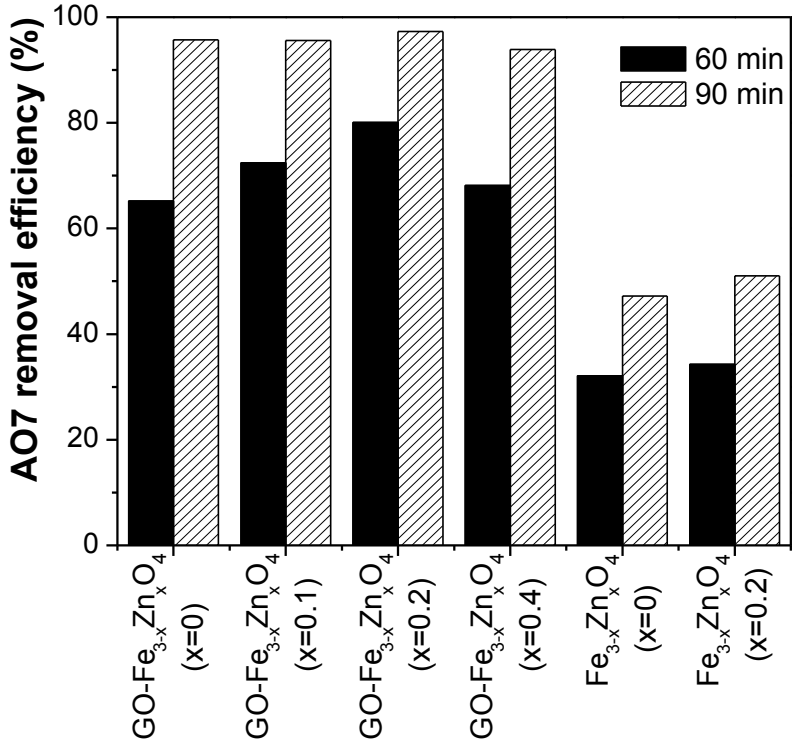

Figure 7.10: The AO7 removal efficiency by GO–$Fe_{3-x}Zn_xO_4$ nanocomposites and $Fe_{3-x}Zn_xO_4$ NPs at different zinc molar ratio (x) in the UV-assisted heterogeneous Fenton-like reaction. Experimental conditions: AO7 35 mg L^{-1}, H_2O_2 22 mM, catalyst 0.2 g L^{-1}, pH 3, 4 x 8W UV-A and 90 min of reaction.

Let us now consider the catalysts containing GO. As observed in Figure 7.10 a significant enhancement in efficiency occurred within the first 60 min of UV-irradiation. Of particular attention, the AO7 degradation increased to 65% (x=0) and peaked at 80% (x=0.2), thus clearly showing that (i) a higher catalytic activity is achieved for the partially substituted zinc nanocomposites and (ii) UV-assisted process also enhanced the heteregeneous Fenton-like reaction as compared with the

lower non UV-assisted AO7 degradation values observed in Figure 7.9. It is also very interesting to note that the AO7 degradation goes almost to completion at ~98% at 120 min for all samples tested under UV-assisted conditions.

Table 7.3: The rate constants of GO–$Fe_{3-x}Zn_xO_4$ nanocomposites in both heterogeneous and UV-assisted Fenton-like reactions

Sample	Heterogeneous Fenton-like reaction		UV-assisted heterogeneous Fenton-like reaction	
	Kinetic constant, k (min^{-1})	R^2	Kinetic constant, k (min^{-1})	R^2
GO–$Fe_{3-x}Zn_xO_4$, x=0	0.0054	0.9379	0.0367	0.9304
GO–$Fe_{3-x}Zn_xO_4$, x=0.1	0.0083	0.9773	0.0399	0.9375
GO–$Fe_{3-x}Zn_xO_4$, x=0.2	0.0119	0.9331	0.0450	0.9516
GO–$Fe_{3-x}Zn_xO_4$, x=0.4	0.0062	0.9287	0.0358	0.9367
$Fe_{3-x}Zn_xO_4$, x=0	0.0023	0.9482	0.0092	0.9521
$Fe_{3-x}Zn_xO_4$, x=0.2	0.0024	0.9601	0.0102	0.9512

Further analyses of results suggest that the oxidative degradation of AO7 using GO–$Fe_{3-x}Zn_xO_4$ nanocomposites fitted well the pseudo-first-order reaction kinetics ($R^2 > 0.93$) as summarised in Table 7.3. From the data, it can be inferred that the catalytic activity of the nanocomposites were highly dependent on the presence of GO as a catalyst support, whereas faster AO7 oxidative degradation was attained in the presence of UV-irradiation during the heterogeneous Fenton-like reaction. The increase in photocatalytic activity is attributed to the combined effect between the GO and also the partial substitution of zinc into the Fe_3O_4 structure, which improved the photoresponse of Fe_3O_4 [36] by preventing direct recombination of photo induced electrons and holes during catalysis [37-39] as evidenced in the UV–vis diffuse reflectance spectroscopy analysis (UV–vis DRS) shown in Figure S1 and Table S2 (see Supplementary Information in Appendix D). The fast reaction rate at x=0.2 is addressed in more detail in the discussion section below.

7.5 Discussion

One important point to observe is the AO7 degradation efficiency of ~30% (Figure 7.9) is low compared with ~76% for Fe_3O_4 NPs in Chapter 4. However, it is not the case that the partial

substitution of zinc into $Fe_{3-x}Zn_xO_4$ NPs is proving to be detrimental. This is mainly attributed to the changes in the synthesis methods. For instance, in this work the synthesis was carried at 90 ºC and using NH_4OH as the precipitating agent. The synthesis of the catalysts in Chapter 4 was carried out at room temperature and using NaOH. As a different precipitating agent and temperature conditions were used, this led to different growth of NPs being deposited onto the GO sheets, which can be correlated with the dominant effect of Ostwald ripening phenomena during the synthesis. As an example, larger particle (10–15 nm) growth of Fe_3O_4 were observed (Figure 7.7a,b) in GO–$Fe_{3-x}Zn_xO_4$ as compared to GO–Fe_3O_4 (<10 nm) in Chapter 4. Further, surface areas are much lower in this work for Fe_3O_4 NPs of 140 $m^2\ g^{-1}$ as compared with that in Chapter 4 of 289 $m^2\ g^{-1}$. Hence, the synthesis method used in this work led to the formation of different morphologies with lower surface area which explains the reduction in catalytic activity. However, this synthesis method was important to incorporate zinc into the Fe_3O_4 catalysts.

A major finding of this work is the effect conferred by GO in significantly improving the catalytic activity of the nanocomposites, whether as in UV-assisted heterogeneous reaction or not. This is clearly evidenced by the results in Figures. 7.9 and 7.10. Hence, the discussion from hereon is focussed on the GO–$Fe_{3-x}Zn_xO_4$ nanocomposites only. Again it must be pointed out that the surface areas of the GO–$Fe_{3-x}Zn_xO_4$ (~300 $m^2\ g^{-1}$) are lower than that of GO–Fe_3O_4 (374 $m^2\ g^{-1}$) in Chapter 4, and the arguments on the reduction of catalytic activity are the same.

It is noteworthy that the highest catalytic activity was found to be at zinc molar ratio of x=0.2 for both non-UV and UV-assisted heterogeneous Fenton-like reaction, resulting in overall rate constants (k) of 0.0119 and 0.0450 min^{-1} (Table 7.3). In principle, there are no significant variations in surface areas (Figure 7.2a) as zinc molar ratio (x) varies between 0 and 0.4 to justify the AO7 degradation peaking at x=0.2 and then reducing at x=0.4. There is a small reduction in pore volume (Figure 7.2b) though the resultant nanocomposites are mesoporous in nature, so there is no foreseeable hindrance for AO7 to access active sites in the catalysts. For these reasons, the structure of the nanocomposites does not explain the catalytic activity peaking at x=0.2, and then reducing. In fact, the catalytic activity is almost similar for x=0 and x=0.4. Hence, there are other factors affecting the catalytic degradation of AO7.

Another morphological change is the reduction of the crystallite size from x=0 to x=0.2 as listed in Table 7.1, though there are small values for x=0.1 and x=0.4. In principle, the reduction of the crystallite size should translate into improving the catalytic activity to a certain degree. It is not possible to say with a high degree of certainty that the crystallite sizes for x=0.1 (5.16 nm) and x=0.4 (4.43 nm), which are slightly lower as compared to x=0.2 (5.73 nm), confer a reduction in the kinetics of the catalytic activity.

So far the variations of the morphological features are not significant to justify the peaking of the AO7 degration at x=0.2. Therefore, another avenue for this justification should be sought based on the chemical functionalities conferred by the nanocomposites. Due to the photoluminescence properties of zinc, the nanocomposites were analysed by UV−vis. By comparing to the spectra of $Fe_{3-x}Zn_xO_4$ NPs (x=0 and 0.2) in Figure S1a (see Supplementary Information in Appendix D), all the GO–$Fe_{3-x}Zn_xO_4$ nanocomposites exhibited strong absorption in the visible-light region within 580–800 nm. These changes may be ascribed to the narrower band gap of the catalyst. It can be anticipated the formation of shallow defect states in the $Fe_{3-x}Zn_xO_4$ surface or inter-surface due to metal oxide particle immobilisation onto GO sheets via the strong interfacial interactions (Fe–O–C bonds). Defect states into the $Fe_{3-x}Zn_xO_4$ band gap create shallow trap states thus facilitating the photogeneration of electrons from lower-energy photons as reported elsewhere [40]. As can be seen from both Figure S1b and Table S2 (see Supplementary Information in Appendix D), the GO–$Fe_{3-x}Zn_xO_4$ at x=0.2 possessed the narrowest band gap energy (E_g= 1.90 eV) amongst others. Therefore, narrowing the E_g as well as in the presence of some shallow trap states enables the higher production efficiency of electrons and holes while preventing them from direct recombination during photocatalysis [37-39]. With respect to XPS, the Fe–O and Zn–O binding energies are overlapping at 530 eV. In fact, the binding energy of iron oxide and zinc oxide is at 711 and 1021.7 eV and any relationship between these elements cannot be drawn. However, the XPS measurements for all GO–$Fe_{3-x}Zn_xO_4$ nanocomposites show that the sp^2 carbon were within 59.7% (x=0) and 54.8% (x=0.4). This may be ascribed to the decreased reduction in GO with the incorporation of zinc during the synthesis.

Such results can be further corroborated with the deconvolution results of the C 1s spectra as shown in Table 7.2, which clearly shows that the C–C/ C–O ratio increased from 1.0 (pure GO) to 2.7 (x=0), peaking at 3.2 (x=0.2) and reducing to 3.1 (x=0.4). There are two important points for discussion here. First, the same ratio in Chapter 4 for GO–Fe_3O_4 was close to 4, which is higher than in this work. This means that the state of GO in GO–$Fe_{3-x}Zn_xO_4$ is not effectively being reduced when exposed to weak bases (NH_4OH) in this work as compared to NaOH in Chapter 4. These findings correlate well with reports from Fan et al. [41] and Chen et al. [42] on the reduction of GO in strong basic solutions (NaOH and KOH) in the absence of the typical reducing agents. The second point relates to the fact that the C–C/ C–O ratio peaking at 3.2 (x=0.2) is mainly associated with the contribution of sp^2 carbon domain (C=C) at binding energy of 284.6 eV (Figure 7.6) which intensifies at x=0.2, and then decreases at x=0.4. The change in C–C/ C–O ratio may affect the electron transfer between GO and NPs as per major findings in Chapter 4 and 6. Hence, it is plausible to argue that the improvement of the reaction kinetics of the partially substituted zinc nanocomposites at x=0.2 as determined in Table 7.3 is associated with a high concentration of sp^2 carbon domains. As such,

GO–$Fe_{3-x}Zn_xO_4$ nanocomposites containing a zinc molar ratio (x) of 0.2 conferred the efficient regeneration of the Fenton active species in producing more $HO^{\bullet}$ radicals under the UV-assisted reaction to oxidise AO7.

It is also possible to argue that the covalent interaction between Zn–O–Fe and GO could be enhanced for x=0.2, thus delivering the highest catalytic activity. It was shown in Chapter 4 that the covalent bond between GO and Fe–O (proved by XPS) improved the electron transfer in the Fenton-like reaction. As ZnO is a semiconductor which has the ability to partially reduce the GO [43] under UV radiation, it is plausible to consider that the ZnO modulate the electron transfer via the nanocomposite. This modulation is based on the assumption that zinc has fully incorporated into the Fe_3O_4, which is evident in the XRD patterns (Figure 7.3). This modulation improves the reaction kinetics up to x=0.2 and then decreases thereafter. Nevertheless, the chemical bonds and structures could not be clearly ascertained in this work by all the techniques used (XRD and XPS). Therefore, a higher level of characterisation is required such as using synchrotron light. For instance, XAS (x-ray absorption spectroscopy) analyses may determine quantitatively the oxidation state and coordination environment of the nanocomposites as Zn–O and/or Zn–O–Fe.

7.6 Conclusions

A series of GO–$Fe_{3-x}Zn_xO_4$ nanocomposites with different zinc concentration were prepared through a facile precipitation-oxidation method in the presence of GO. The partial substitution of zinc into the Fe_3O_4 was confirmed by the combined characterisation using XRD, TG-DTG, XPS, and STEM-EDS analysis. There was no visible formation of secondary phase or impurity peaks in the nanocomposites, indicating the partial substitution of zinc into the Fe_3O_4 crystal structure with a good dispersion within the Fe_3O_4 matrix. The reaction kinetics peaked at a zinc molar ratio (x) of 0.2 for GO–$Fe_{3-x}Zn_xO_4$ nanocomposites towards the AO7's oxidative degradation in both heterogeneous and UV-assisted Fenton-like reactions. Such improvement could not be attributed to the morphology as no significant structural changes were observed. However, it was found that C–C/ C–O ratio peaked at 3.2 (x=0.2), which is mainly associated with the sp^2 carbon domain contribution (C=C) at binding energy of 284.6 eV. The higher amount of the sp^2 carbon domain on the GO basal planes leads to an effective electron transfer between the GO and zinc partially substituted magnetite NPs. Nevertheless, the GO structure has been found to significantly increase the oxidative degradation of AO7 (by 30% or more) and also the reaction kinetics, thus conferring faster regeneration of the Fenton active species in producing more $HO^{\bullet}$ radicals for the degradation of AO7 under both heterogeneous and UV-assisted Fenton-like reactions. GO played a major role in modulating the overall catalytic activity of

nanocomposites, since the zinc only provides minor effect towards the catalytic performance for oxidative degradation of AO7.

References

[1] S. Guo, G. Zhang, Y. Guo, J.C. Yu, Graphene oxide–Fe_2O_3 hybrid material as highly efficient heterogeneous catalyst for degradation of organic contaminants, Carbon 60 (2013) 437-444.

[2] N.A. Zubir, C. Yacou, J. Motuzas, X. Zhang, J.C. Diniz Da Costa, Structural and functional investigation of graphene oxide–Fe_3O_4 nanocomposites for the heterogeneous Fenton-like reaction, Sci. Rep. 4 (2014) 4594 1-8.

[3] N.A. Zubir, C. Yacou, X. Zhang, J.C. Diniz da Costa, Optimisation of graphene oxide–iron oxide nanocomposite in heterogeneous Fenton-like oxidation of acid orange 7, J. Environ. Chem. Eng. 2 (2014) 1881-1888.

[4] Y. Dong, J. Li, L. Shi, J. Xu, X. Wang, Z. Guo, W. Liu, Graphene oxide-iron complex: synthesis, characterization and visible-light-driven photocatalysis, J. Mater. Chem. A 1 (2013) 644-650.

[5] Z.L. Hua, W.Q. Ma, X. Bai, R.R. Feng, L. Yu, X.Y. Zhang, Z.Y. Dai, Heterogeneous Fenton degradation of bisphenol A catalyzed by efficient adsorptive Fe_3O_4/GO nanocomposites, Environ. Sci. Pollut. Res. 21 (2014) 7737-7745.

[6] R. Matta, K. Hanna, S. Chiron, Fenton-like oxidation of 2,4,6-trinitrotoluene using different iron minerals, Sci. Total Environ. 385 (2007) 242-251.

[7] R.C.C. Costa, M.F.F. Lelis, L.C.A. Oliveira, J.D. Fabris, J.D. Ardisson, R.R.V.A. Rios, C.N. Silva, R.M. Lago, Novel active heterogeneous Fenton system based on $Fe_{3-x}M_xO_4$ (Fe, Co, Mn, Ni): The role of M^{2+} species on the reactivity towards H_2O_2 reactions, J. Hazard. Mater. 129 (2006) 171-178.

[8] X. Liang, Z. He, Y. Zhong, W. Tan, H. He, P. Yuan, J. Zhu, J. Zhang, The effect of transition metal substitution on the catalytic activity of magnetite in heterogeneous Fenton reaction: In interfacial view, Colloids Surf. A 435 (2013) 28-35.

[9] X. Liang, Z. He, G. Wei, P. Liu, Y. Zhong, W. Tan, P. Du, J. Zhu, H. He, J. Zhang, The distinct effects of Mn substitution on the reactivity of magnetite in heterogeneous Fenton reaction and Pb(II) adsorption, J.Colloid Interf. Sci. 426 (2014) 181-189.

[10] Y. Zhong, X. Liang, W. Tan, Y. Zhong, H. He, J. Zhu, P. Yuan, Z. Jiang, A comparative study about the effects of isomorphous substitution of transition metals (Ti, Cr, Mn, Co and Ni) on the UV/Fenton catalytic activity of magnetite, J. Mol. Catal. A 372 (2013) 29-34.

[11] L. Menini, M.C. Pereira, L.A. Parreira, J.D. Fabris, E.V. Gusevskaya, Cobalt- and manganese-substituted ferrites as efficient single-site heterogeneous catalysts for aerobic oxidation of monoterpenic alkenes under solvent-free conditions, J. Catal. 254 (2008) 355-364.

[12] R. Amrousse, A. Tsutsumi, A. Bachar, D. Lahcene, N_2O catalytic decomposition over nano-sized particles of Co-substituted Fe_3O_4 substrates, Appl. Catal. A 450 (2013) 253-260.

[13] R.C.C. Costa, M. De Fátima Fontes Lelis, L.C.A. Oliveira, J.D. Fabris, J.D. Ardisson, R.R.V.A. Rios, C.N. Silva, R.M. Lago, Remarkable effect of Co and Mn on the activity of $Fe_{3-x}M_xO_4$ promoted oxidation of organic contaminants in aqueous medium with H_2O_2, Catal. Commun. 4 (2003) 525-529.

[14] H.W.P. Carvalho, P. Hammer, S.H. Pulcinelli, C.V. Santilli, E.F. Molina, Improvement of the photocatalytic activity of magnetite by Mn-incorporation, Mater. Sci. Eng. B 181 (2014) 64-69.

[15] X. Liang, Y. Zhong, S. Zhu, L. Ma, P. Yuan, J. Zhu, H. He, Z. Jiang, The contribution of vanadium and titanium on improving methylene blue decolorization through heterogeneous UV-Fenton reaction catalyzed by their co-doped magnetite, J. Hazard. Mater. 199-200 (2012) 247-254.

[16] S. Yang, H. He, D. Wu, D. Chen, X. Liang, Z. Qin, M. Fan, J. Zhu, P. Yuan, Decolorization of methylene blue by heterogeneous Fenton reaction using $Fe_{3-x}Ti_xO_4$ ($0 \leq x \leq 0.78$) at neutral pH values, Appl. Catal. B 89 (2009) 527-535.

[17] X. Liang, Y. Zhong, H. He, P. Yuan, J. Zhu, S. Zhu, Z. Jiang, The application of chromium substituted magnetite as heterogeneous Fenton catalyst for the degradation of aqueous cationic and anionic dyes, Chem. Eng. J. 191 (2012) 177-184.

[18] X. Liang, S. Zhu, Y. Zhong, J. Zhu, P. Yuan, H. He, J. Zhang, The remarkable effect of vanadium doping on the adsorption and catalytic activity of magnetite in the decolorization of methylene blue, Appl. Catal. B 97 (2010) 151-159.

[19] Y. Zhong, X. Liang, Z. He, W. Tan, J. Zhu, P. Yuan, R. Zhu, H. He, The constraints of transition metal substitutions (Ti, Cr, Mn, Co and Ni) in magnetite on its catalytic activity in heterogeneous Fenton and UV/Fenton reaction: From the perspective of hydroxyl radical generation, Appl. Catal. B. 150-151 (2014) 612-618.

[20] W.S. Hummers, R.E. Offeman, Preparation of graphitic oxide, J. Am. Chem. Soc. 80 (1958) 1339-1339.

[21] Z. Xiong, L.L. Zhang, X.S. Zhao, Visible-light-induced dye degradation over copper-modified reduced graphene oxide, Chem. Eur. J. 17 (2011) 2428-2434.

[22] S.S. Pati, J. Philip, A facile approach to enhance the high temperature stability of magnetite nanoparticles with improved magnetic property, J. Appl. Phys. 113 (2013) 44314 1-9.

[23] X. Liang, Y. Zhong, S. Zhu, H. He, P. Yuan, J. Zhu, Z. Jiang, The valence and site occupancy of substituting metals in magnetite spinel structure $Fe_{3-x}M_xO_4$ (M = Cr, Mn, Co and Ni) and their influence on thermal stability: An XANES and TG-DSC investigation, Solid State Sci. 15 (2013) 115-122.

[24] X. Zhang, D.K. Wang, D.R.S. Lopez, J.C. Diniz da Costa, Fabrication of nanostructured TiO_2 hollow fiber photocatalytic membrane and application for wastewater treatment, Chem. Eng. J. 236 (2014) 314-322.

[25] J. Su, M. Cao, L. Ren, C. Hu, Fe_3O_4–graphene nanocomposites with improved lithium storage and magnetism properties, J. Phys. Chem. C 115 (2011) 14469-14477.

[26] J.M. Byrne, V.S. Coker, E. Cespedes, P.L. Wincott, D.J. Vaughan, R.A.D. Pattrick, G. Van Der Laan, E. Arenholz, F. Tuna, M. Bencsik, J.R. Lloyd, N.D. Telling, Biosynthesis of zinc substituted magnetite nanoparticles with enhanced magnetic properties, Adv. Funct. Mater. 24 (2014) 2518-2529.

[27] G. Lu, S. Qiu, J. Liu, X. Wang, C. He, Y.-J. Bai, Enhanced electrochemical performance of Zn-Doped Fe_3O_4 with carbon coating, Electrochim. Acta 117 (2014) 230-238.

[28] M. Chiesa, M.C. Paganini, E. Giamello, D.M. Murphy, C. Di Valentin, G. Pacchioni, Excess electrons stabilized on ionic oxide surfaces†, Accounts Chem. Res. 39 (2006) 861-867.

[29] M. Noorjahan, V. Durga Kumari, M. Subrahmanyam, L. Panda, Immobilized Fe(III)-HY: an efficient and stable photo-Fenton catalyst, Appl. Catal. B 57 (2005) 291-298.

[30] G. Jiang, Z. Lin, C. Chen, L. Zhu, Q. Chang, N. Wang, W. Wei, H. Tang, TiO_2 nanoparticles assembled on graphene oxide nanosheets with high photocatalytic activity for removal of pollutants, Carbon 49 (2011) 2693-2701.

[31] A. Prakash, S.K. Misra, D. Bahadur, The role of reduced graphene oxide capping on defect induced ferromagnetism of ZnO nanorods, Nanotechnol. 24 (2013) 95705-95714.

[32] R.R. Prabhakar, N. Mathews, K.B. Jinesh, K.R.G. Karthik, S.S. Pramana, B. Varghese, C.H. Sow, S. Mhaisalkar, Efficient multispectral photodetection using Mn doped ZnO nanowires, J. Mater. Chem. 22 (2012) 9678-9683.

[33] M. Ahmad, S. Yingying, H. Sun, W. Shen, J. Zhu, SnO_2/ZnO composite structure for the lithium-ion battery electrode, J. Solid State Chem. 196 (2012) 326-331.

[34] A. Prakash, S. Chandra, D. Bahadur, Structural, magnetic, and textural properties of iron oxide-reduced graphene oxide hybrids and their use for the electrochemical detection of chromium, Carbon 50 (2012) 4209-4219.

[35] H. He, C. Gao, Supraparamagnetic, conductive, and processable multifunctional graphene nanosheets coated with high-density Fe_3O_4 nanoparticles, ACS Appl. Mater. Interf. 2 (2010) 3201-3210.

[36] Ingler, J.P. Baltrus, S.U.M. Khan, Photoresponse of p-type zinc-doped iron(III) oxide thin films, J. Am. Chem. Soc. 126 (2004) 10238-10239.

[37] D. Beydoun, R. Amal, G.K.C. Low, S. McEvoy, Novel photocatalyst: Titania-coated magnetite. Activity and photodissolution, J. Phys. Chem. B 104 (2000) 4387-4396.

[38] G. Liao, S. Chen, X. Quan, H. Yu, H. Zhao, Graphene oxide modified g-C_3N_4 hybrid with enhanced photocatalytic capability under visible light irradiation, J. Mater. Chem. 22 (2012) 2721-2726.

[39] C. Chen, W. Cai, M. Long, B. Zhou, Y. Wu, D. Wu, Y. Feng, Synthesis of visible-light responsive graphene oxide/TiO_2 composites with p/n heterojunction, ACS Nano 4 (2010) 6425-6432.

[40] B. Qiu, Y. Zhou, Y. Ma, X. Yang, W. Sheng, M. Xing, J. Zhang, Facile synthesis of the Ti^{3+} self-doped TiO_2-graphene nanosheet composites with enhanced photocatalysis, Sci. Rep. 5 (2015) 8591 1-6.

[41] X. Fan, W. Peng, Y. Li, X. Li, Deoxygenation of exfoliated graphite oxide under alkaline conditions: A green route to graphene preparation, Adv. Mater. 20 (2008) 4490-4493.

[42] C. Chen, W. Kong, H.-M. Duan, J. Zhang, Theoretical simulation of reduction mechanism of graphene oxide in sodium hydroxide solution, Phys. Chem. Chem. Phys. 16 (2014) 12858-12864.

[43] G. Williams, P.V. Kamat, Graphene-semiconductor nanocomposites: excited-state interactions between ZnO nanoparticles and graphene oxide, Langmuir 25 (2009) 13869-13873.

Chapter 8

Conclusions and recommendations

8.1 Conclusions

This thesis focused on the development of GO–Fe_3O_4 nanocomposites as an alternative heterogeneous Fenton-like catalyst for the oxidative degradation of synthetic dye. In particular, this thesis endeavoured to investigate the synergistic structural and functional effects of GO–Fe_3O_4 nanocomposites. To this end, GO loading was systematically investigated to understand the novel structural formation and physicochemical properties of the resultant nanocomposites. In addition, the GO–Fe_3O_4 nanocomposites were comprehensively tested to determine their overall catalytic performance, and compared under the same reaction conditions against conventional Fe_3O_4 nanoparticles (NPs) and GO as the catalyst support.

The first key finding of this thesis was that GO proved to be a promising catalyst support for immobilisation of Fe_3O_4 NPs. For instance, GO–Fe_3O_4 nanocomposites resulted in superior catalytic performance for the degradation of a textile dye pollutant, acid orange 7 (AO7), in the heterogeneous Fenton-like reaction as compared to the control catalysts of Fe_3O_4 NPs and GO sheets. This was attributed to the good dispersion of Fe_3O_4 NPs onto GO sheets as well as the synergistic effect of GO on the pre-concentration of AO7 within the vicinity of active sites ($\equiv Fe^{2+}$/ $\equiv Fe^{3+}$) to be further oxidised by the generated $HO^{\bullet}$ radicals during catalysis.

The first contribution to knowledge of this thesis was that the synergistic interaction between GO and Fe_3O_4 NPs led to the formation of two distinct structures with different catalytic activities. The first structure corresponded to a low GO loading up to 10 wt%, which prevented the aggregation of the Fe_3O_4 NPs and the stacking of GO sheets, resulting in a desirable structure with higher surface area up to 409 $m^2\ g^{-1}$. The second structure was correlated with the deposition of Fe_3O_4 NPs mainly onto the exterior surface of GO which stacked at higher GO loading (>10 wt%). It was found that the low GO loading nanocomposites led to higher AO7 degradation (92–98%) owing to the high surface area and pore volume, which enhanced the mass transfer of reactants towards the active sites ($\equiv Fe^{2+}$/ $\equiv Fe^{3+}$). Contrary to these results, the removal efficiency of AO7 at higher GO loading gradually declined from 88 to 60%.

Further investigations based on the GO(5wt%)–Fe_3O_4 nanocomposites with best catalytic activity demonstrated that optimal operational conditions were found to be at the catalyst dosage of 0.2 g L^{-1}, initial pH of 3 and 22 mM of H_2O_2 concentration at 298 K. In fact, there were no significant differences (except for temperature) on the optimal conditions between the one-parameter-at-a-time and the global optimisation method by using response surface methodology. The high coefficient value (0.9742) of the derived quadratics model indicated the high correlation between the experimental and predicted values. The oxidative degradation of AO7 can be well described by a pseudo-first-order kinetic through the Langmuir–Hinshelwood mechanism which is dominated by the rate of intrinsic chemical reactions on the surface of active sites rather than the rate of mass transfer.

Another key finding is that the GO–Fe_3O_4 nanocomposites demonstrated superior catalytic activity and stability by sustaining nearly 98% of AO7 removal with insignificant iron leaching over seven consecutive cycles of heterogeneous Fenton-like reaction. This performance is far superior as compared to conventional Fe_3O_4 NPs which deactivated very quickly leading to barely discernible removal of AO7 (~0%) at the fifth cycle onwards. A key second contribution of this thesis is the postulation that this superior stability is attributed to the donor-acceptor synergistic interaction between the GO sheets and the immobilised Fe_3O_4 NPs. This was proven by the key finding that the Fe^{3+}/Fe^{2+} ratio of the GO–Fe_3O_4 was maintained during the reactions contrary to that of Fe_3O_4 NPs. This vital property of the donor-acceptor mechanism confers the spontaneous reduction of $\equiv Fe^{3+}$ to regenerate into $\equiv Fe^{2+}$ which is actively participating in the decomposition of H_2O_2 into HO• radicals. This postulation was further supported by another key finding related to electron transfer between GO and oxidised active sites ($\equiv Fe^{3+}$) via Fe–O–C bonds based on GO's slight oxidation.

The last contribution of this thesis was demonstrated by the fact that GO also contributed significantly UV-assisted Fenton-like reactions. Although samples were too dark in hue to undertake UV-vis analysis, GO loaded catalysts improved the oxidative degradation of AO7 by ~30% or more as compared to samples without GO. Interestingly, even samples containing photo-luminescent zinc as GO–$Fe_{3-x}Zn_xO_4$ ($0 \leq x \leq 0.4$) provided minor catalytic activity improvement only. The catalytic kinetic activity peaked for x=0.2 samples, which was attributed to the higher sp^2 carbon domain on the basal plane, responsible for the transference of electrons from the GO to the catalyst nanoparticles.

8.2 Recommendations for future work

This research has shown the potential of using GO–Fe_3O_4 nanocomposites as an alternative heterogeneous Fenton-like catalyst based on their superior catalytic activity and stability for the oxidative degradation of AO7. Therefore, recommendations for future work follows below.

There are a large number of pollutants in wastewaters which are recalcitrant and very difficult to be destroyed even by advanced oxidation technologies. These include caffeine, carbamazepine, diclofenac, codeine, sulfamethoxazole and bisphenol A. Hence, there is a window of opportunity to investigate the use of GO loaded catalyst to treat wastewaters containing these recalcitrant pollutants.

The key finding of the GO effect in the UV-assisted heterogeneous Fenton-like reaction was unexpected. Additionally, the catalytic activity for the GO–$Fe_{3-x}Zn_xO_4$ nanocomposites could be associated with Zn–O–Fe and GO chemical bonds and structures which could not be clearly ascertained in this work by all the techniques used (XRD and XPS). Therefore, a higher level of characterisation is required such as using synchrotron light such as XAS (X-ray absorption spectroscopy) analyses.

Appendix

Appendix A - Supplementary Information (Chapter 3)

Detailed correction for minor mistakes on published papers

Chapter 3

Section 1. Introduction, Page 37

The third sentence in the introduction section and its reference have been revised as follows:

More importantly, these wastewaters are considered to be carcinogenic, mutagenic and toxic once certain concentration levels are reached depending on the types of dye presence.[3]

Revised reference

[3] A. Gottlieb, C. Shaw, A. Smith, A. Wheatley, S. Forsythe, The toxicity of textile reactive azo dyes after hydrolysis and decolourisation, J. Biotechnol. 101 (2003) 49-56.

Appendix B - Supplementary Information (Chapter 5)

Supplementary Information

Optimisation of graphene oxide–iron oxide nanocomposite in heterogeneous Fenton-like oxidation of Acid Orange 7

Nor Aida Zubir[1,2], Christelle Yacou[1], Xiwang Zhang[3] and João C. Diniz da Costa[1*]

[1]*The University of Queensland, FIMLab—Films and Inorganic Membrane Laboratory, School of Chemical Engineering, Brisbane, Qld 4072, Australia*

[2]*Universiti Teknologi MARA (UiTM), Faculty of Chemical Engineering, 13500 Pulau Pinang, Malaysia*

[3]*Department of Chemical Engineering, Monash University, Clayton Vic 3800, Australia*

*Email Id of Corresponding Author: j.dacosta@uq.edu.au

Table S1. The k_{obs} and decolourisation rate of AO7 at different dye initial concentration in heterogeneous Fenton-like reaction.

C_{AO7o} (mg L^{-1})	k_{obs} (min^{-1})	Decolourisation of AO7 (%)	R^2
15	0.039	99.71	0.9415
25	0.029	99.07	0.9875
35	0.022	97.82	0.9890
45	0.015	92.28	0.9898
55	0.013	81.39	0.9803

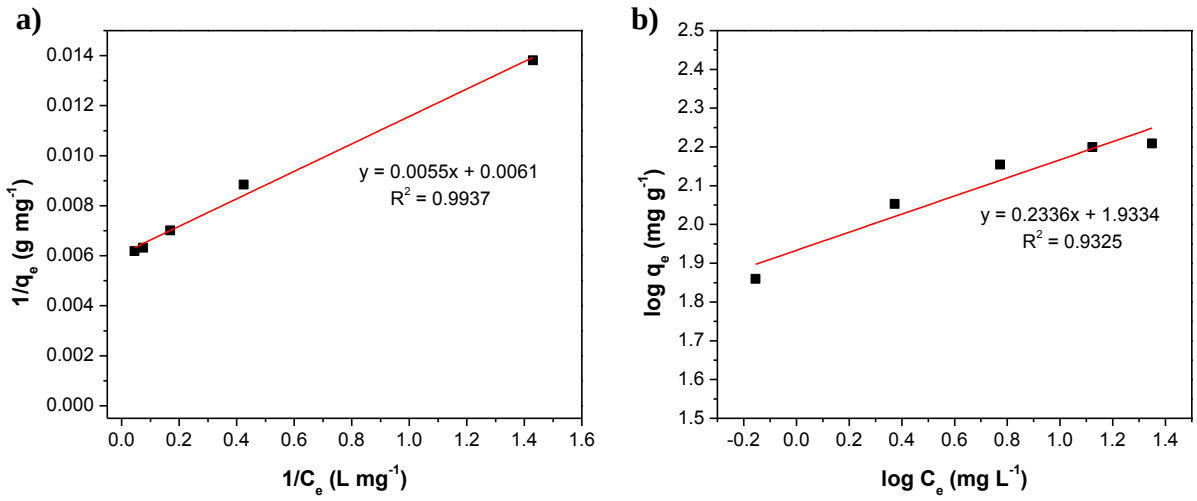

Fig. S1. Adsorption isotherms of GO–Fe_3O_4 nanocomposite using (a) Langmuir and (b) Freundlich models

Table S2. Adsorption isotherms parameters for AO7 removal by GO–Fe_3O_4 nanocomposite

Langmuir			**Freundlich**		
q_m (mg g^{-1})	**K_L (L mg^{-1})**	**R^2**	**k_F (mg g^{-1})**	**n**	**R^2**
163.934	1.109	0.9937	1.933	4.281	0.9325

Table S3. FCCD design matrix of the chosen parameters with corresponding responses.

Parameters (Factors)	Code	Unit	Level		
			Low (-1)	Centre (0)	High (+1)
Dosage	A	g L^{-1}	0.15	0.20	0.25
pH	B	-	2.5	3.0	3.5
Temperature	C	K	298	313	328

Run	Parameters			Degradation of AO7 (%)	
	A	B	C	Experiment	Predicted
1	-1	-1	-1	79.35	80.55
2	+1	-1	-1	79.64	80.86
3	-1	+1	-1	59.84	60.98
4	+1	+1	-1	62.01	62.83
5	-1	-1	+1	77.33	77.00
6	+1	-1	+1	87.11	86.46
7	-1	+1	+1	70.75	70.02
8	+1	+1	+1	81.72	81.01
9	-1	0	0	92.50	91.21
10	+1	0	0	97.54	96.86
11	0	-1	0	84.15	82.71
12	0	+1	0	70.73	70.20
13	0	0	-1	96.97	92.60
14	0	0	+1	97.51	99.92
15	0	0	0	92.22	95.89
16	0	0	0	97.74	95.89
17	0	0	0	93.08	95.89
18	0	0	0	93.14	95.89
19	0	0	0	97.74	95.89
20	0	0	0	97.51	95.89

Table S4. ANOVA for the derived response surface quadratic model.

Source	Sum of squares	Degree of freedom	Mean square	*F*-Value	Prob. > *F*	Comment
Model	2803.80	9	311.53	41.95	< 0.0001	Significant
A-Dosage	*79.81*	*1*	*79.81*	*10.75*	*0.0083*	
B-pH	*391.00*	*1*	*391.00*	*52.65*	*< 0.0001*	
C-Temperature	*134.03*	*1*	*134.03*	*18.05*	*0.0017*	
AB	*1.18*	*1*	*1.18*	*0.16*	*0.6988*	
AC	*41.82*	*1*	*41.82*	*5.63*	*0.0391*	
BC	*79.19*	*1*	*79.19*	*10.66*	*0.0085*	
A^2	*9.48*	*1*	*9.48*	*1.28*	*0.2850*	
B^2	*1038.87*	*1*	*1038.87*	*139.89*	*< 0.0001*	
C^2	*0.36*	*1*	*0.36*	*0.049*	*0.8293*	
Residual	74.26	10	7.43			
Lack of Fit	*38.42*	*5*	*7.68*	*1.07*	*0.4707*	*Not significant*
Pure Error	*35.85*	*5*	*7.17*			

Note: $R^2 = 0.9742$; Adjusted $R^2 = 0.9510$

Appendix C - Supplementary Information (Chapter 6)

Table S1. Atomic concentration (%) of sp^2 carbon domain in GO–Fe_3O_4 nanocomposites before and after long-term stability test.

Cycles	Atomic concentration (%) of sp^2 carbon	Reduction percentage of sp^2 carbon domain (%)
0	61.40	0.00
1	60.95	0.73
3	53.31	13.18
5	51.62	15.93
7	49.91	18.71

Table S2. AO7 removal efficiency for the long-term stability test using GO–Fe_3O_4 nanocomposites and Fe_3O_4 NPs in the heterogeneous Fenton-like reaction.

Cycle	AO7 removal efficiency (%)	
	GO–Fe_3O_4	Fe_3O_4
1	96.13 ± 0.81	69.96 ± 2.92
2	98.07 ± 1.62	54. 74 ± 5.09
3	98.73 ± 0.65	51.78 ± 7.72
4	98.67 ± 1.13	10.05 ± 2.19
5	98.64 ± 0.73	0.71 ± 8.51
6	98.63 ± 1.77	No removal
7	98.93 ± 0.98	No Removal

Table S3. Leaching of iron (Fe) during long-term stability testing.

Cycles	Fe leached into solution (ppm)	Percentage of Fe leached from $GO–Fe_3O_4$ * (%)
1	0.165	0.09
3	0.340	0.18
5	0.553	0.29
7	0.723	0.38

*based on the total Fe initially present in the $GO–Fe_3O_4$ nanocomposites

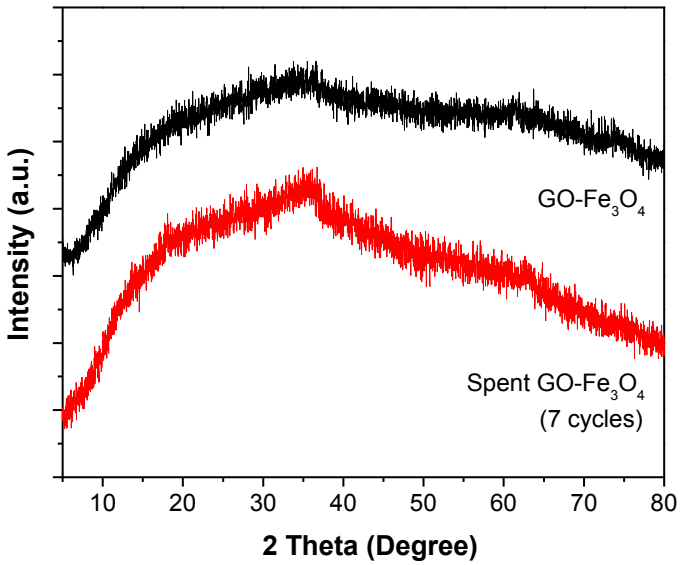

Fig. S1. XRD patterns of pristine and spent $GO–Fe_3O_4$ nanocomposites after long-term stability test.

Appendix D - Supplementary Information (Chapter 7)

Table S1. The AO7 removal efficiency (%) of GO–$Fe_{3-x}Zn_xO_4$ nanocomposites in the UV-assisted Fenton-like reactions.

Sample	AO7 removal efficiency (%)	
	60 min	90 min
GO–$Fe_{3-x}Zn_xO_4$, x=0	65.22	95.69
GO–$Fe_{3-x}Zn_xO_4$, x=0.1	72.40	95.57
GO–$Fe_{3-x}Zn_xO_4$, x=0.2	80.07	97.30
GO–$Fe_{3-x}Zn_xO_4$, x=0.4	68.12	93.87
$Fe_{3-x}Zn_xO_4$, x=0	32.12	47.21
$Fe_{3-x}Zn_xO_4$, x=0.2	34.27	52.05
Blank (without catalyst)	0.68	1.31

Remarks:
Experimental conditions: AO7 0.1 mM, H_2O_2 22 mM, catalyst 0.2 g L^{-1}, pH 3, 4 x 8W UV-A

Table S2. The bandgap energies of $Fe_{3-x}Zn_xO_4$ NPs and GO–$Fe_{3-x}Zn_xO_4$ nanocomposites.

Samples	Bandgap energy, E_g (eV)
GO-$Fe_{3-x}Zn_xO_4$, x=0	1.92
GO-$Fe_{3-x}Zn_xO_4$, x=0.1	1.91
GO-$Fe_{3-x}Zn_xO_4$, x=0.2	1.90
GO-$Fe_{3-x}Zn_xO_4$, x=0.4	1.93
$Fe_{3-x}Zn_xO_4$, x=0	1.95
$Fe_{3-x}Zn_xO_4$, x=0.2	1.94

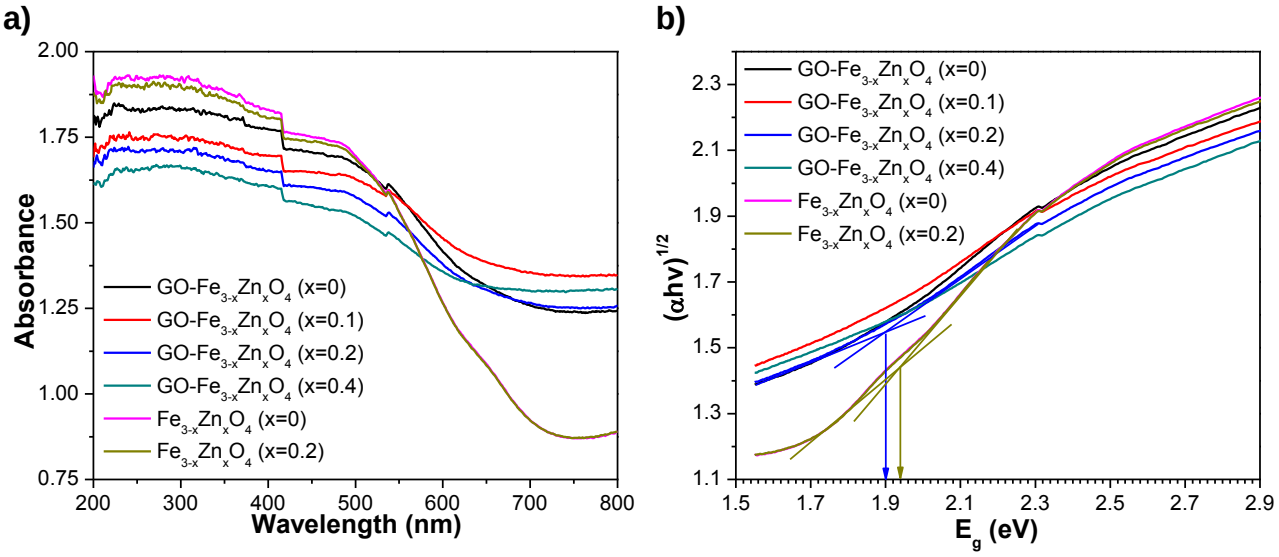

Figure S1. (a) UV–vis diffuse reflectance spectra of $Fe_{3-x}Zn_xO_4$ NPs and GO–$Fe_{3-x}Zn_xO_4$ nanocomposites and (b) the plot of Kubelka-Munk function against the photon energy.